# MODELING WINTER STORMS OVER ARIZONA

Final Report
Volume I

Prepared for
Arizona Department of Water Resources
Under IGA-0-AG-30-08290

September 1995

**U.S. DEPARTMENT OF THE INTERIOR**
Bureau of Reclamation
Technical Service Center
Water Resources Services
River Systems and Meteorology Group

# REPORT DOCUMENTATION PAGE

Public reporting burden for this collection of information is estimated to average 1 hour per response, including the time for reviewing instrucitons, searching exisitng data sources, gathering and maintaining the data needed, and completing and reviewing the collection of information. Send comments regarding this burden estimate or any other aspect of this collection of information, including suggestions for reducing this burden to Washington Headquarters Services, Directorate for Information Operations and Reports, 1215 Jefferson Davis Highway, Suit 1204, Arlington VA 22202-4302, and to the Office of Management and Budget, Paperwork Reduction Report (0704-0188), Washington DC 20503.

| 1. AGENCY USE ONLY *(Leave Blank)* | 2. REPORT DATE<br>September 1995 | 3. REPORT TYPE AND DATES COVERED<br>Final |
|---|---|---|

**4. TITLE AND SUBTITLE**
Modeling Winter Storms Over Arizona
Final Report—Volume I

**5. FUNDING NUMBERS**
PR

**6. AUTHOR(S)**
D.A. Matthews and J.G. Medina

**7. PERFORMING ORGANIZATION NAME(S) AND ADDRESS(ES)**
Bureau of Reclamation
Technical Service Center
Denver CO 80225

**8. PERFORMING ORGANIZATION REPORT NUMBER**
R-95-11

**9. SPONSORING/MONITORING AGENCY NAME(S) AND ADDRESS(ES)**
Bureau of Reclamation
Technical Service Center
PO Box 25007
Denver CO 80225-0007

**10. SPONSORING/MONITORING AGENCY REPORT NUMBER**
DIBR

**11. SUPPLEMENTARY NOTES**
Microfiche and hard copy available at the Technical Service Center, Denver, Colorado

**12a. DISTRIBUTION/AVAILABILITY STATEMENT**

Available from the National Technical Information Service, Operations
Division, 5285 Port Royal Road, Springfield, Virginia 22161

**12b. DISTRIBUTION CODE**

**13. ABSTRACT *(Maximum 200 words)***

The Bureau of Reclamation has adapted two numerical models for precipitation augmentation research at the Mogollon Rim of Arizona. The AAIM (Arizona Airflow and Microphysics) model simulates local airflow and transport of cloud seeding materials released from seeding generators. The orographic precipitation model simulates daily precipitation at grid points.

The AAIM diagnoses airflow and ice crystal trajectories. Comparisons of simulated results with field measurements indicated modeled plume top heights within 200 to 500 m of those observed; plume widths were within 3 km of observed values. If applied at 3- or 6-h intervals on newly collected sounding data taken upwind from the Mogollon Rim, the model should be useful in field programs requiring cloud seeding agent targeting.

The orographic precipitation model simulates winter precipitation over the Colorado Rocky Mountains. Comparisons of simulated precipitation with Mogollon Rim measurements yielded a correlation of 0.75 with daily estimates and 0.92 with monthly totals. Correlation of simulated winter-spring precipitation with Salt and Verde River seasonal streamflow yielded respective values of 0.97 and 0.84. The model offers useful skill and should be beneficial in the planning, conduct, and evaluation of future cloud seeding experiments.

**14. SUBJECT TERMS**--atmospheric research/ meteorology/ weather modification/ orographic clouds/ cloud seeding/ meteorological instruments/ Arizona Snowpack Augmentation Program/ Arizona Department of Water Resources/ Sierra Cooperative Pilot Project/ Arizona Airflow and Microphysics Model/ National Center for Atmospheric Research/

**15. NUMBER OF PAGES**
85

**16. PRICE CODE**

| 17. SECURITY CLASSIFICATION OF REPORT | 18. SECURITY CLASSIFICATION OF THIS PAGE | 19. SECURITY CLASSIFICATION OF ABSTRACT | 20. LIMITATION OF ABSTRACT |
|---|---|---|---|
| UL | UL | UL | UL |

R-95-11

# MODELING WINTER STORMS
# OVER ARIZONA

Final Report
Volume I

Prepared for

Arizona Department of Water Resources
Under IGA-0-AG-30-08290

by

D.A. Matthews and J.G. Medina

River Systems and Meteorology Group
Water Resources Services
Technical Service Center
Denver, Colorado

September 1995

UNITED STATES DEPARTMENT OF THE INTERIOR    ★    BUREAU OF RECLAMATION

## ACKNOWLEDGEMENTS

## U.S. Department of the Interior
## Mission Statement

As the Nation's principal conservation agency, the Department of the Interior has responsibility for most of our nationally-owned public lands and natural resources. This includes fostering sound use of our land and water resources; protecting our fish, wildlife, and biological diversity; preserving the environmental and cultural values of our national parks and historical places; and providing for the enjoyment of life through outdoor recreation. The Department assesses our energy and mineral resources and works to ensure that their development is in the best interests of all our people by encouraging stewardship and citizen participation in their care. The Department also has a major responsibility for American Indian reservation communities and for people who live in island territories under U.S. administration.

# CONTENTS

# CONTENTS – CONTINUED

## TABLES

## FIGURES

# CONTENTS – Continued
## FIGURES – Continued

# EXECUTIVE SUMMARY

The Mogollon Rim, a mountain range located north through east of Phoenix, produces most of the runoff originating in Arizona. The mountains act as a barrier, forcing moving air to rise and descend in conformance with the terrain. The ascending air cools and, if moisture is present, clouds form, some eventually producing precipitation. This process, known as the orographic precipitation process, is generally well understood and occurs to some degree in all winter storms crossing the Mogollon Rim. Reclamation (Bureau of Reclamation) and the ADWR (Arizona Department of Water Resources) have collaborated on field and modeling studies of seeding material targeting and orographic precipitation processes. This report describes the results of the modeling studies.

In the past several decades, many research studies have been performed on the augmentation of precipitation from orographic clouds (e.g., Grant and Mielke, 1967; Mielke et al., 1971; Elliott et al., 1978; Super and Heimbach, 1983; Reynolds and Dennis, 1986) similar to those that occur in Arizona. Recognition that Mogollon Rim winter clouds may be seedable to produce additional precipitation led to the initiation of the ASAP (Arizona Snowpack Augmentation Program) involving cooperative research studies between the ADWR and Reclamation. The research is aimed at assessing winter cloud seeding potential on the Mogollon Rim and developing a cloud seeding technology that can lead to additional precipitation and runoff.

The initial effort under ASAP was a preliminary cloud seeding feasibility study (Bureau of Reclamation, 1987) using existing data. Recommendations in that study led to the conduct of field experiments on Mogollon Rim clouds during early 1987 and 1988 (Super et al., 1989). The results of the field experiments were encouraging, suggesting that cloud seeding on Mogollon Rim may be feasible. A 5-year plan was subsequently developed (Super et al., 1991) that called for the conduct of additional field experiments to test and refine conceptual models of cloud physical processes and determine the feasibility of a follow up randomized seeding program. The latter would estimate seeding effects on watershed precipitation and runoff expected over long periods, such as several winters.

The Arizona field experiments produced valuable insight into future experimentation needs. Analyses of field data suggested that numerical models could be useful in the planning, conduct, and evaluation of future Arizona cloud seeding experiments. Successful modeling studies have been conducted recently for other geographical locations with Reclamation assistance. Two such programs include the SCPP (Sierra Cooperative Pilot Project) (Reynolds and Dennis, 1986; Rauber et al., 1988) conducted in the Sierra Nevada, and a Moroccan cloud seeding project (Matthews et al., 1989) performed in the Atlas Mountains of Morocco. Consequently, a cooperative modeling effort was pursued as part of the ASAP.

A targeting model would be useful to future seeding experiments if it could yield, for given cloud conditions, proper ground seeding dispersal points and aircraft seeding tracks that would target additional precipitation for desired watershed areas. An orographic precipitation model that could accurately estimate daily precipitation at grid points of a fine mesh grid also could improve future seeding programs. Consequently, a targeting model and an orographic precipitation model were selected for adaptation to the Mogollon Rim. Preference was given to models that required minimal inputs and were fast running on microcomputers. Such operational models can be employed on a real-time basis in the field.

**Airflow and Microphysics Targeting Model Study**

The model selected for adaptation to Arizona was the SCPP model (Rauber et al., 1988). The adapted model is called the AAIM (Arizona Airflow and Microphysics) model. It has been adapted to the Mogollon Rim and performs well for operational applications of targeting seeding material to produce precipitation in the desired "target area." AAIM model adaptation and validation were based on data collected in the 1987 ASAP. The model is a fast objective diagnostic tool that is useful for daily decision making in field programs. The AAIM model was adapted to simulate the effect of lifting over a simplified barrier with a ridge orientation of 315 to 135°, which is perpendicular to the 225° winds that are typical of many significant precipitation events. It diagnosed the airflow and thermodynamic conditions based on data observed in soundings from rawinsondes or aircraft systems during 1987 field operations.

Model diagnoses of airflow and ice crystal trajectories appear to match observed airflow patterns and range of likely crystal trajectories. The model plume top was generally within 200-500 m of that observed and model plume width was within 3 km of the observed width. Plume positions downwind of $SF_6$ (sulfur hexafluoride) tracer release points generally matched the aircraft observed plume patterns and were within 2-5 km of the observed position at HJK (Happy Jack). However, results show that the model is sensitive to sounding variations that often occur within 3- to 6-h periods and within distances of 100 to 200 km. These variations produced significant changes in model predictions of plume and ice crystal trajectories. This variability suggests that rawinsondes observed at 3- to 6-h intervals during field operations and observed at a two sites, one upwind of the barrier and the other along the Rim, will improve model performance.

Case study results suggest that ground-based seeding may be effective in about a quarter of the precipitation events. Two types of storms appear to have potential for ground-based seeding: cold mid-winter storms with surface freezing temperatures over the Mogollon Rim, and late winter unstable convective systems with deeper vertical transport of seeding nuclei. Temperatures over the Rim at this low latitude are often too warm for ground-based seeding; therefore, airborne seeding will likely be required for most conditions. Model tests of airborne seeding suggest that the AAIM model will be a useful tool for positioning the seeding and cloud physics aircraft. The limited sample of cases studied in 1987 precluded broad generalizations regarding suitable seeding generator sites and flight tracks; still, they provided a useful model adaptation test.

Comparisons with coarse resolution simulations from the more sophisticated, three-dimensional Clark (1977) model show that the AAIM model did not capture three-dimensional, time-dependent features of flow over the Mogollon Rim; but it did capture the essence of the targeting information. More accurate and detailed results from the Clark model provide better theoretical information and guidance; but this model has not been proven as an economical operational real-time tool for weather modification field projects. Current studies by Gall and Bruintjes will evaluate the operational application of the Clark model and help determine the role of the AAIM model in future field projects. At this time, we recommend the AAIM model as an operational tool for real-time decision making.

Additional studies and field tests of the model are recommended to evaluate model performance and to improve our understanding of the physical processes controlling transport and diffusion of seeding materials. Cloud physics experiments are recommended to better understand the precipitation processes and improve the modeled simulations of these complex processes. These projects should involve comparisons with the high resolution Clark model simulations and its coarser resolution operational version. During the initial field tests of the operational version of the Clark model, parallel runs with the AAIM model are recommended as a backup to provide timely information.

**Orographic Precipitation Model Study**

The orographic precipitation model selected for adaptation was a model developed by Rhea (1978). This grid point model attempts to simulate only the most important physical processes involved in orographic precipitation. The two-dimensional, steady-state, multilayer model accounts for moisture flow from any direction by employing 36 grid arrays of topography, one for each 10° of the compass, at a grid point spacing selected as 10 km for Arizona. The model computes effects of terrain rate-of-rise, "shadowing" by upstream barriers, and vertical displacement of the individual air layers resulting from interaction with the underlying topography. Enhanced rise of air layers over the highest terrain is employed to simulate effects of convection, the only model feature aimed at this process. A simple formulation based on the temperature of a high-altitude moist layer is used to calculate the precipitation efficiency.

The model requires only a limited number of inputs. It needs only twice daily rawinsonde data at the upwind border of the model domain, consisting of estimates of the pressure height, temperature, relative humidity, and the wind direction and speed. For each geographical region, the model must be given the positions of precipitation gauges or other locations of interest and descriptions of watersheds for which computations are desired. Outputs produced in each model run are precipitation estimates at each grid point and other positions denoted in inputs, and volume precipitation (precipitation integrated over all area contained in each watershed) for each designated watershed. Point and volume precipitation can be integrated in successive runs over selected time periods such as months or seasons.

The adaptation process for the orographic precipitation model employed rawinsonde data for the 10 winters of 1978-88, from Desert Rock in southern Nevada and Winslow and Tucson in Arizona. Ground truth was obtained from daily precipitation data from 11 gauges distributed along higher elevations of the Mogollon Rim. The model computed daily estimates of the precipitation for each gauge location and also the mean value for the 11 gauges. The model generated means were then compared with the corresponding 11-gauge mean values. Precipitation differences of model and gauge estimates and correlation values from data pairs assisted in adjusting model parameters.

Using preferred model parameters, the correlation obtained of model estimated precipitation versus respective gauge means, for 1683 days of the 10 winters, was 0.75. When monthly sums rather than daily totals were employed, the correlation improved to 0.92, indicative of reduced noise by integration in time. The 10-winter sum of daily 11-gauge means was 3326.2 mm (130.95 in) versus 3369.3 mm (132.65 in) estimated by the model, a 1.3 percent overestimate.

Application of correlation analysis to monthly volume precipitation for the Verde River watershed and stream gauge measurements from the Verde River below Tangle Creek, above

Horseshoe Dam, yielded a correlation of 0.66. The similar analysis for the monthly sums of the two gauges, Salt River near Roosevelt and Tonto Creek above Gun Creek, and corresponding model estimates, produced a correlation of 0.56. The analyses were also performed with stream gauge totals from the seasonal runoff period of November through June, and corresponding model volume precipitation obtained by integration over November through April. The correlation obtained for the Verde watershed was 0.84, and for the Salt-Tonto watersheds the value was 0.97. The sample size was 10 seasons in the seasonal analysis and 60 months in the monthly analysis.

Model runs and precipitation data were employed to study features of winter storms of importance to cloud seeding feasibility and application. On the average, precipitation was recorded by at least 1 of the 11 Mogollon Rim precipitation gauges about 85 days per winter (here November through April). Modeling showed that about 88 percent of Mogollon Rim winter precipitation occurred with moist southwest steering-level winds (taken here as the 700-mb level, near 3000 m or 10,000 ft).

Additional results indicated that nearly all precipitation occurred with 500-mb (near 5500 m or 18,000 ft) temperatures within the cloud seeding window of less than or equal to -10 °C and equal to or greater than -27 °C, suggested in some studies (e.g., Grant and Elliott, 1974) to lead to positive seeding results. However, temperatures at the 750-mb level (near 2500 m or 8200 ft) during storms were rather warm, frequently exceeding -6 °C and sometimes above freezing. Warm temperatures at this level can present a formidable problem to cloud seeding by ground-based generators because temperatures above -6 °C substantially decrease the formation of ice crystals from seeding with commonly available agents. If clouds contain supercooled liquid water, a necessity for successful cloud seeding, it is often concentrated in the first kilometer above the barrier crest (in the vicinity of the 750- to 700-mb zone over the Mogollon Rim, where diffusion can deliver the ground-based generator produced seeding agent). Comparison of 750-mb temperatures from regional soundings employed in the model, with local soundings collected by Super et al. (1989) near Camp Verde located just west of the Mogollon Rim crest, show the regional sounding temperatures exceeded the corresponding local sounding values by a couple degrees, considered insufficient to materially allay concern for difficulties with ground-based seeding in some, and perhaps many, Arizona storms.

Wind speeds at 700 mb, important for targeting the seeding agent in winter storms, were also analyzed. Though this level is sometimes above the layer of most interest for transport of the seeding agent, it serves as an index of wind speeds for the transporting layers. Many productive precipitation episodes occurred with higher wind speeds. About as many precipitation days (days with at least one gauge recording some precipitation) occurred with winds exceeding 15 m s$^{-1}$ as with winds of less than 5 m s$^{-1}$. However, weak wind cases accounted for only about 12 percent of strong-wind precipitation amounts. These analyses suggested the need for further study on whether weak wind cases can be modified by cloud seeding to obtain a higher precipitation efficiency.

In summary, the adapted orographic precipitation model will produce useful estimates of daily precipitation at grid points spaced at 5 or 10 km over the Mogollon Rim and develop volume precipitation for the Salt-Verde watersheds. The model should be useful in planning future cloud seeding experiments, developing seeding suspension criteria, constructing daily weather forecasts necessary for seeding operations, and designing and performing the evaluation of cloud seeding effects on precipitation and streamflow. Additionally, model generated grid point

precipitation can be employed as input to a physical hydrologic model that estimates daily runoff.

# 1. INTRODUCTION

## 1.1 Clouds and Cloud Seeding in Arizona

Although Arizona depends heavily on ground water and water from upstream States that are pumped from the Colorado River, runoff originating within the State is still an important component of its total water supply. Most of the runoff that originates within Arizona comes from the mountainous northern half, in particular, from the Mogollon Rim.

The Mogollon Rim is a range of mountains located to the north through east of Phoenix. A computer-generated view of Arizona's terrain from a vantage point above the southwestern area of the State clearly shows the Rim (fig. 1.1). Summit elevations generally run 2000 to 2500 m (6560 to 8200 ft), although a few peaks exceed 3000 m (9840 ft). San Francisco Mountain north of Flagstaff, and the White Mountains east-northeast of Phoenix, are the two most prominent high elevation areas of the Rim.
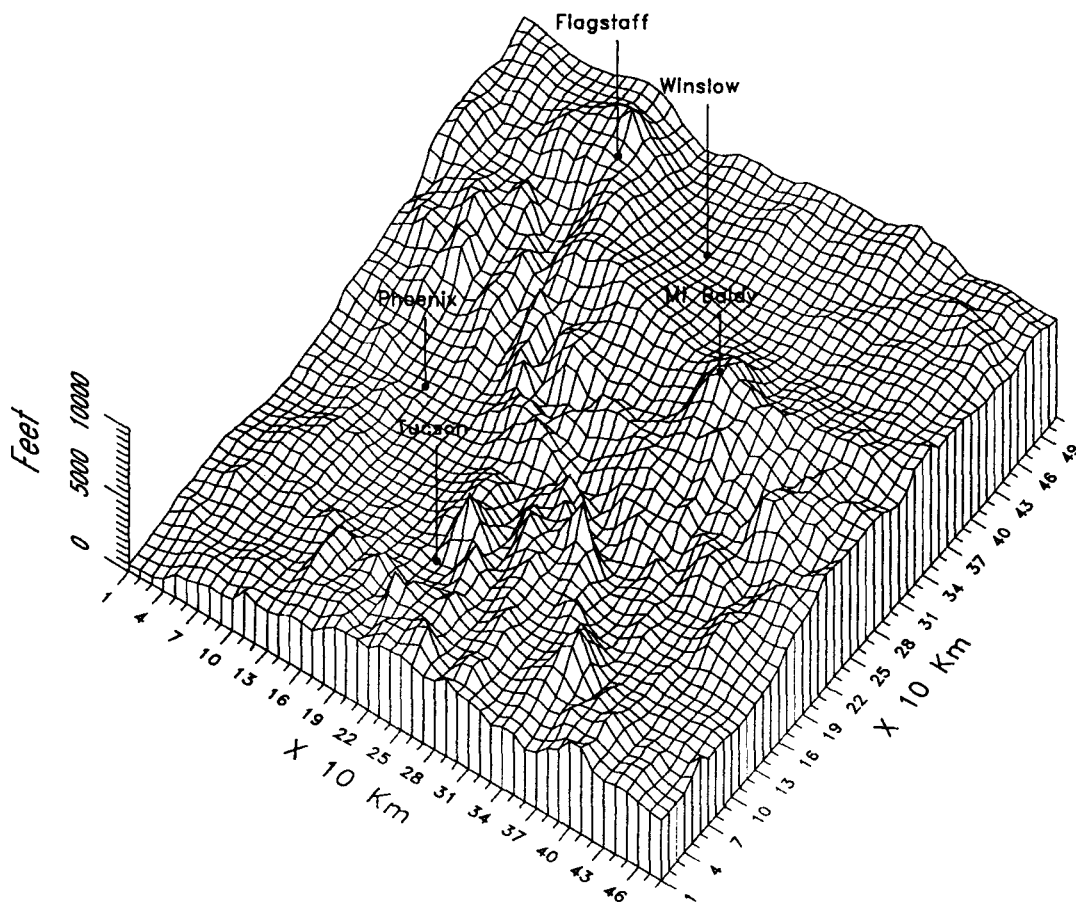


Figure 1.1. – A computer-generated view of Arizona's terrain from a vantage point above the southeastern area of the State shows the Mogollon Rim.

1

Winter storms force air currents up and over the Mogollon Rim. Some moisture condenses from the ascending air to form clouds and, sometimes, snow or rain. This rain or snow is called orographic precipitation because of the role orography plays in producing it. The orographic precipitation process is fairly well understood, as shown schematically on figure 1.2.
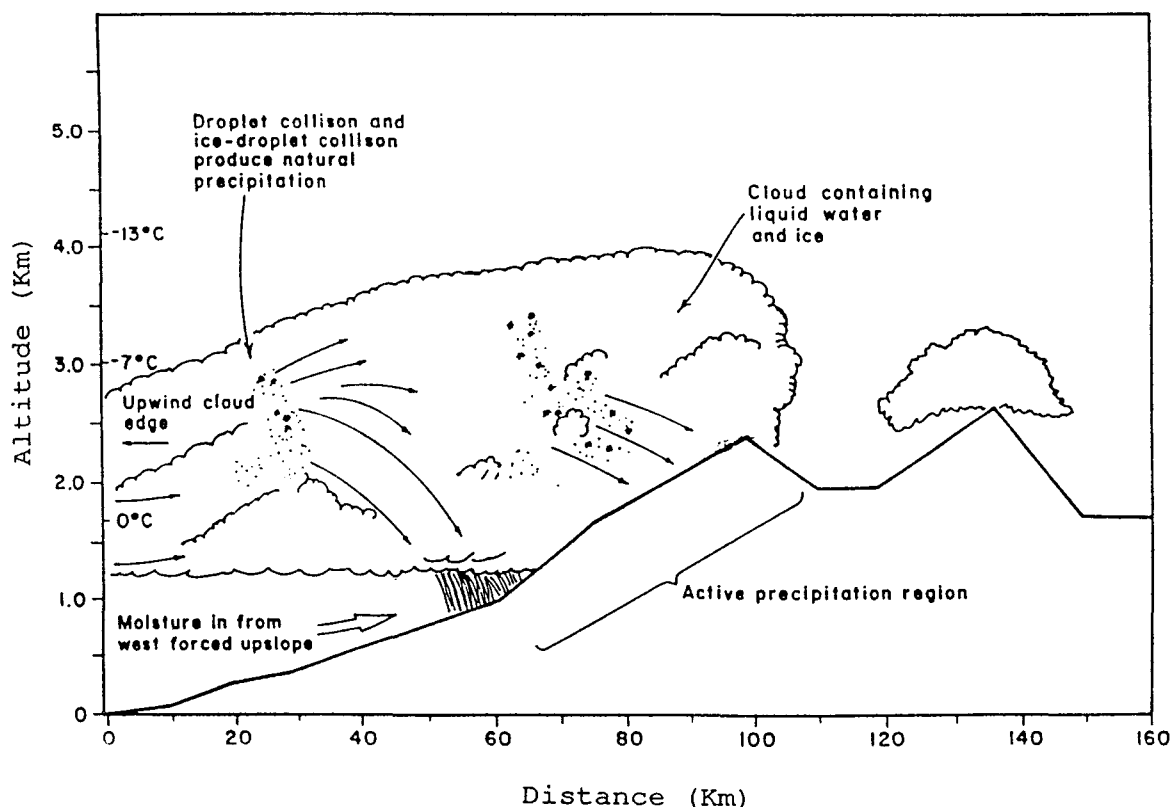


Figure 1.2. – Schematic of the orographic precipitation process.

The character of winter storms impacting the Mogollon Rim suggests some potential for precipitation augmentation by the application of weather modification technology. Recognition of this possibility has led to inquiry of the status of the technology and the feasibility for application in Arizona.

The ADWR (Arizona Department of Water Resources) and Reclamation (Bureau of Reclamation) began cooperative studies in 1985 in a research program known as the ASAP (Arizona Snowpack Augmentation Program). The main purposes of the research were to assess the potential for winter precipitation augmentation on the higher elevations of the Mogollon Rim and develop a precipitation management technology capable of enhancing the winter precipitation that in turn could be expected to increase streamflow and ground water recharge.

The initial effort under ASAP was the performance of a feasibility study (Reclamation, 1987) that determined cloud data collection was warranted. Consequently, Reclamation's WAG (Water Augmentation Group) conducted field programs on the Rim in 1987 and 1988 (Super et al., 1989). The 1987 program was based at HJK (Happy Jack). Data were collected using a meteorological C-band radar, microwave radiometer, acoustic sounder, aspirated 2D-C probe, and conventional surface instrumentation. An instrumented aircraft collected cloud physics data and tracked plumes of a gas tracer released to simulate seeding. The 1988 program was

based at Hannigan Meadow in the White Mountains, not far from the New Mexico border. It used a smaller set of instrumentation, of which the most important components were the acoustic sounder, the microwave radiometer, and the aspirated 2D-C probe.

Field data analyses were aimed at determining winter cloud characteristics, including supercooled liquid water distribution and precipitation production. Specific analyses, including transport and diffusion studies, dealt with assessing the feasibility of cloud seeding with ground-based AgI (silver iodide) generators.

Under a follow-on agreement, Reclamation prepared a detailed plan for a possible, additional 5-year research program. The suggested program would include physical experiments to test and refine hypothesized physical processes that follow cloud seeding, and determine the feasibility of a follow up randomized program (Super et al., 1991) that would quantify effects from seeding for long periods, such as several winters.

Results of the 1987 and 1988 Arizona experiments and modeling studies in the SCPP (Rauber et al., 1988) and a cloud seeding project in Morocco (Matthews et al., 1989) suggested that future Arizona experiments could be improved by using numerical models. This report covers the adaptation, testing, and some applications to the Mogollon Rim, of a seeding agent targeting model and an orographic precipitation model. Both are operational grid point models that are easily run on microcomputers.

## 1.2 Use of Numerical Models in Weather Modification Projects

The models that guided the first weather modification projects were purely conceptual. For example, cloud seeders hypothesized that the precipitation efficiency of supercooled clouds would be enhanced by the addition of artificial freezing nuclei to promote formation of ice crystals. Targeting of the seeding agent was hampered by lack of knowledge. Projects were evaluated principally by the comparison of precipitation observations from seeded areas with observations at nearby unseeded control areas and by randomized experiments.

Numerical models were introduced into weather modification experiments in the 1960s. They have been used to assess seeding opportunities, provide estimates, and predict potential seeding effects in real time during seeding experiments. Originally, because of limitations of the computers used, most of the modeling had to be done well before field experimentation, to aid in project design and selection of days for seeding trials, or after the experimentation, to aid in evaluation of results. The availability of powerful, portable computers and communications systems in recent years has made it possible to introduce numerical models into the decision making process during the actual conduct of cloud seeding. To obtain maximum benefit for money spent, any future experiments in Arizona should have such tools available.

Future field experiments may be designed to study precipitation in specific watersheds. Cloud seeding for each watershed may be done by aircraft and/or ground-based seeding generators. Proper selection of the seeding generator locations and/or the flight paths for the seeding aircraft is of primary concern to the success of operations.

A targeting model can assist in the design of field programs by determining seeding generator sites and potential flight tracks that conform to principal storm patterns and conditions. During operations, a targeting model can provide real-time information for decision making, including

selecting aircraft seeding tracks and ground-based generators that are appropriate for operation under existing wind and stability conditions.

Cloud seeding projects also need models that predict the natural precipitation. Predictions for the complex terrain of the Mogollon Rim would be useful for planning the conduct of daily operations and determining the cloud treatment effects on precipitation. A properly adapted orographic precipitation model can develop a fully objective estimate of the natural precipitation that can then be used as a covariate in the evaluation process. Additionally, the model can be used to help in the development of cloud seeding suspension criteria.

Chapter two explains the results of the adaptation, testing, and application of the targeting model to the Mogollon Rim. Similarly, for the orographic precipitation model, these processes are discussed in chapter three. User's Guides for each model are provided in two appendixes. Appendix A is a user's guide for the targeting model. Appendix B is a user's guide for the precipitation model.

## 2. ARIZONA AIRFLOW AND MICROPHYSICS MODEL

### 2.1 Model Development

**2.1.1 *History and Adaptation to Arizona*.** – The targeting model selected for the ADWR has been used extensively in other research programs in California and Morocco. It grew out of an "area-of-effect" model developed by Elliott (1971) to guide operational cloud seeding projects. The area-of-effect model evolved into the "Guide Model," that was used to predict the area-of-effect in orographic seeding experiments in the late 1970s.

The Guide Model was a two-dimensional, steady-state model representing a vertical plane cutting across a mountain range or ridge, which was assumed to be uniform along its length. An important feature of the Guide Model was the assumption that airflow across the barrier followed fixed flow channels, which were designed to mimic observed cross-barrier flows. The computer program used different flow channels for unstable-neutral or stable conditions as appropriate. Seeding nuclei from ground generators were dispersed as a plume drifting with the low-level flow until entrained into clouds. Growth of ice particles by diffusion and accretion was simulated as the plume rose through saturated layers.

The SCPP, which was operated over and near the American River Basin of northern California, developed the Guide Model into a quasi-three-dimensional diagnostic targeting model that provided aircraft seeding tracks required to direct seeding effects to a specified point on the ground (Rauber et al., 1988). Huggins et al. (1985) provided more detailed descriptions of the design of flow channels used in the SCPP model. The SCPP model determined the best seeding flight track upwind of a predetermined ground target. The process involved:

(1) manual analysis of soundings to find the appropriate flight level for the release of the seeding material used in each case;
(2) an estimation of the liquid water content of the cloud system from radiometer, soundings, or other aircraft data; and
(3) execution of the targeting model.

The model computed the SLCP (seeding line centerpoint), which the operations director relayed to pilots for their initial flight plan. During the flight to the SLCP, a sounding was taken and relayed to the ground to reinitialize the model with current information. Results were then used to determine the first pass flight track along the revised seedline. If conditions were appropriate, seeding was conducted, if not, a revised SLCP for another flight level was computed. The aircraft checked this site and, if criteria were met, seeding began. The Atlas version of the SCPP model was used in a similar manner in the Morocco Winter Snowpack Augmentation Project. Matthews et al. (1989) describe its application to the High Atlas Mountains of Morocco.

The AAIM (Arizona Airflow and Microphysics) model was adapted from a generic version of the SCPP (Sierra Cooperative Pilot Project) targeting model modified by Dr. Terry Deshler and described by Rauber et al. (1988). The AAIM model was adapted to simulate conditions along the Mogollon Rim in central Arizona. The adaptation of the SCPP model to produce the AAIM model required four basic modifications to the program. First, the local terrain cross section for the Mogollon Rim was added to the model. This addition required selection of the upwind boundary and terrain elevations typical of the transect through the ALT (Allen Lake Tank) and HJK central Mogollon Rim region. Figure 2.1 shows the region from Phoenix to Flagstaff with the AAIM model 225° grid overlay. ALT is located 7.4 km north of HJK falling within the same grid box in the coarse 10 km resolution of the model. The ALT location is plotted in cross sections for purposes of model presentations and future model applications during operations from the ALT area. The 225° grid orientation is nearly perpendicular to the NW-SE axis of the mean barrier crestline. Interestingly, Super et al. (1989) found that the prevailing flow during most heavy precipitation events was from the southwest. This grid orientation provides maximum lifting effects under these conditions. The local terrain is somewhat homogeneous, permitting the assumption of a uniform terrain slope along the length of the crest (y-axis). Line AB shows the location of the transect used for the model terrain.

The second adaptation step was the vertical adjustment of the midflow channel height to the Arizona terrain for stable conditions. The midflow channel was nearly parallel to the terrain at a level ~350mb above the ground shown by line 7 on figure 2.2. At the left boundary of the domain, the midflow channel was located at ~550-mb pressure level. Midpoints of each flow channel are plotted with flow channels numbered from the bottom (1) to top channel (12) to the right of each channel. This figure shows the vertical structure of the model domain with surface terrain for Arizona; flow channels and top of the domain are indicated in pressure and height coordinates for stable cases. The maximum lifting along this channel was assumed to be 60 km upwind of the Rim over the first major ridge southwest of HJK at the wave crest. Theoretical studies show that the primary mountain wave propagates upstream of the crest (Smith, 1979). Aircraft measurements in SCPP showed the airflow crest at 40 km upstream of the Sierra crest. Results from the Clark model (1977) simulations for Arizona show that this wave crest occurs between the crest of the Mogollon Rim and 80 km upstream of the crest and varies with the stability and intensity of flow conditions.
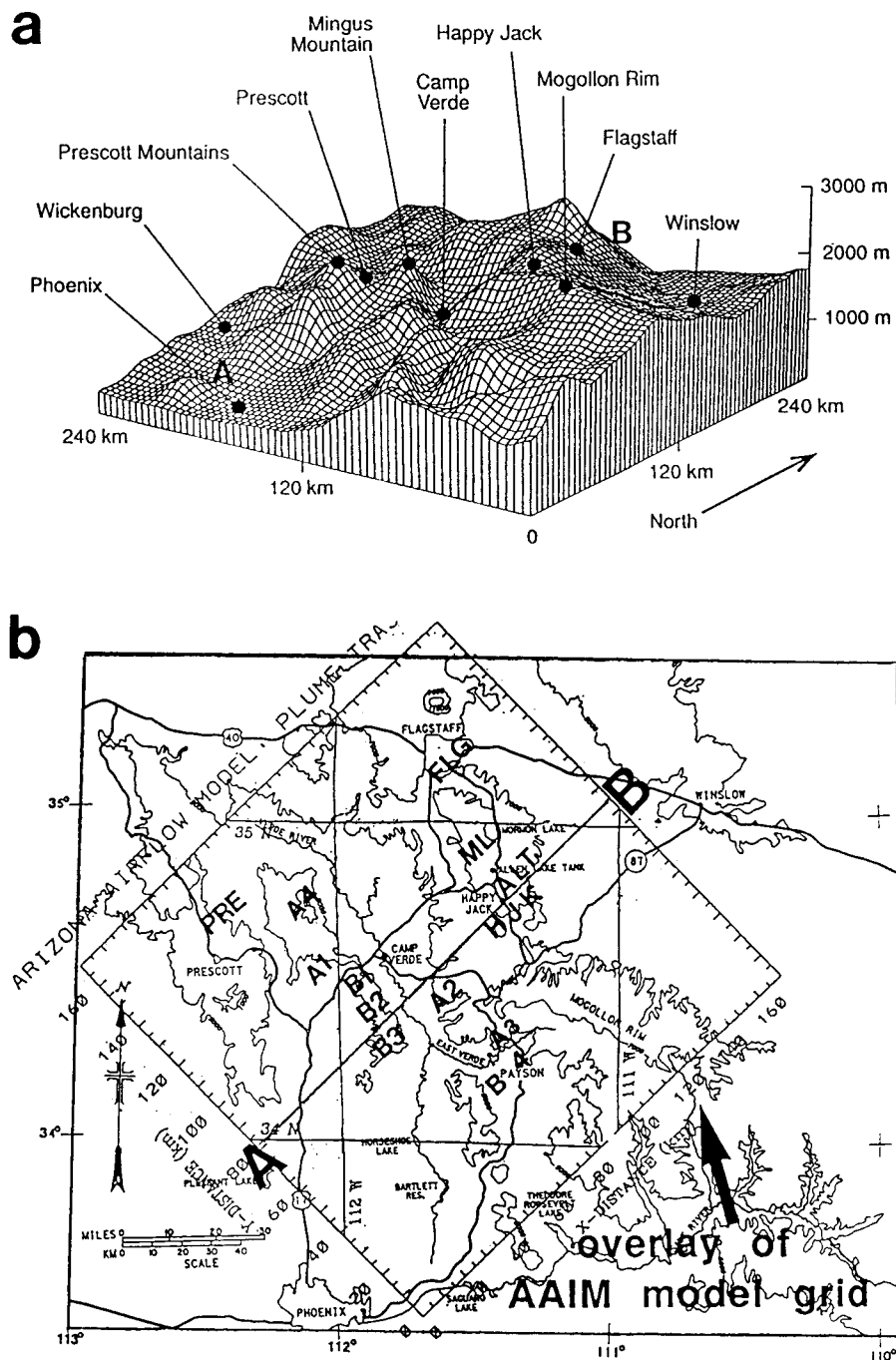
Figure 2.1. – The Mogollon Rim region showing the three-dimensional topography used in the Clark model (a) and a contour map of the area from Phoenix (PHX) to Flagstaff (FLG) showing the AAIM model's 225° grid overlay (b). Key points used in the model simulations are identified by bold letters on the map; numbers indicate locations of simulated seeding generators. Line AB shows the AAIM model cross section through Happy Jack (HJK). Three-dimensional topography from the Clark model illustrates the limitations of simplifying assumptions used in the two-dimensional AAIM model, which performs remarkably well in this complex terrain.

ARIZONA AIRFLOW MODEL: FLOW CHANNEL
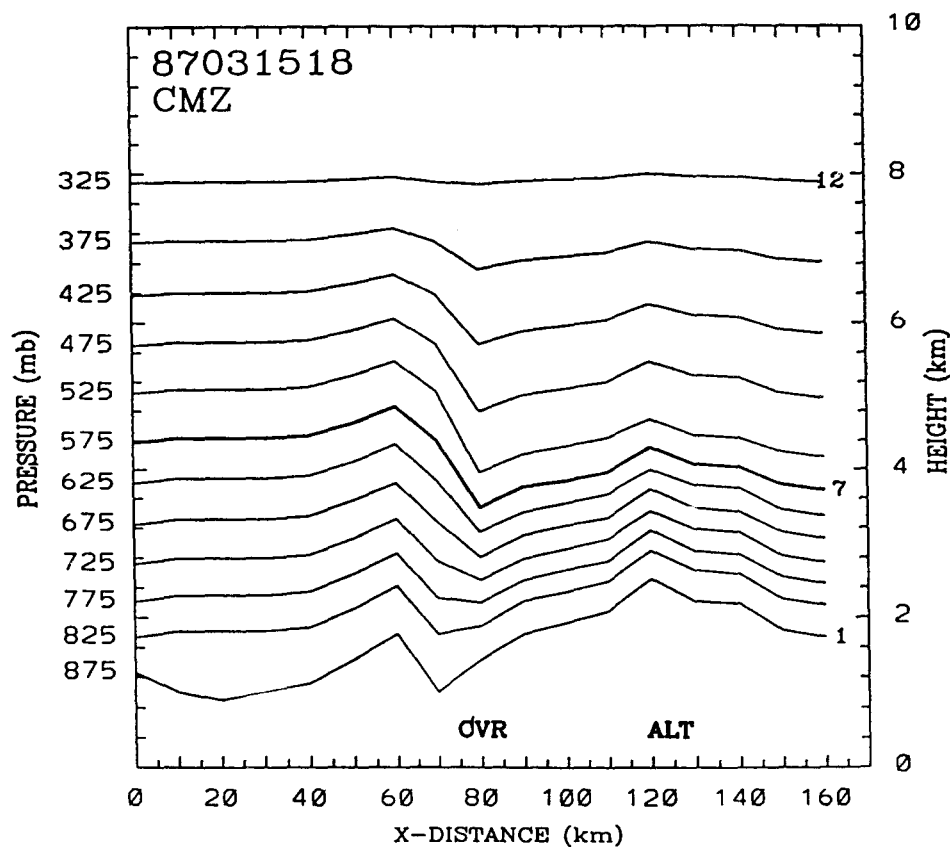
Figure 2.2. – Schematic of the AAIM model vertical cross section along line AB shown in figure 2.1. Heights of the midpoint of channels for stable conditions are labeled from 1 to 12 for the surface to top channels, respectively. Arrows show the airflow through the channels.

The third adaptation step was the adjustment of the midflow channel for neutral-unstable conditions. Figures 2.3 and 2.4 show the difference in the stable and unstable flow channels. Stable flow channels represent the simple stratiform cloud conditions, whereas neutral-unstable channels attempt to represent more complex convective vertical motion fields that produce deeper cloud development. The scientist who runs the model must determine the type of stability for each case from local soundings, and then select the appropriate stability option.

The fourth step required locating specific field sites within the AAIM model grid using model coordinates. The seeding generator sites, sounding locations, VOR/DME aircraft navigation aid site, and landmarks for the Arizona Program were located in the model coordinates. These observations used a different archival format than previous data sets, hence the model initialization procedure was revised for Arizona.

**2.1.2 Graphics Processor Program.** – A special graphics processor was developed to visualize the AAIM model results in a manner readily useful to the project scientists during operations. These graphics show horizontal locations of plumes from ground seeding generators; vertical cross sections of plumes and ice crystal fallout points; aircraft seedline locations and ice crystal fallout points from aircraft seeding; vertical cross sections of flow channel height, temperatures, winds, and mixing ratios; and vertical cross sections of modeled airflow, mixing ratio, potential temperature, equivalent potential temperature, and wind

**a** ARIZONA AIRFLOW MODEL, FLOW CHANNEL
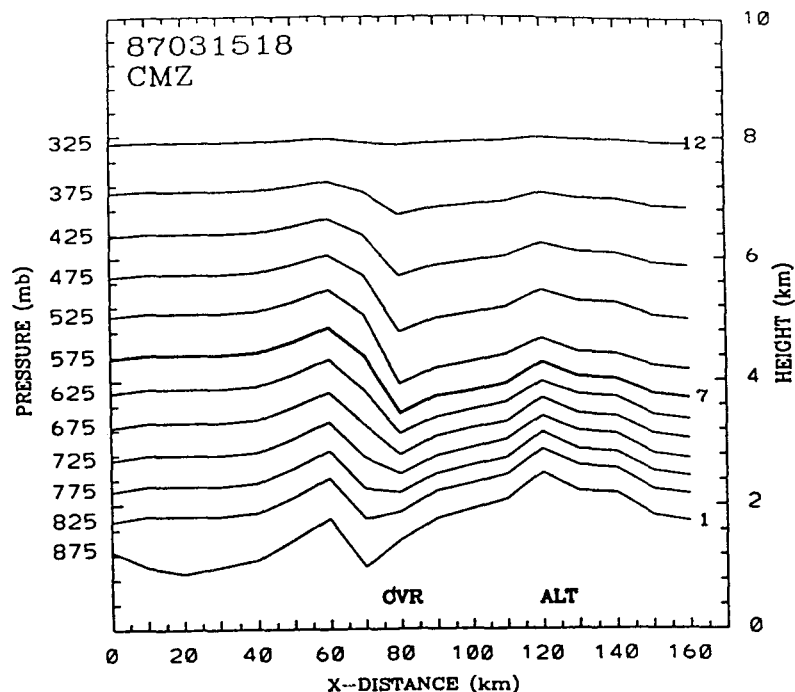


**b** ARIZONA MODEL, Cross-section
VERTICAL VEL. (M/S)
CMZ 87031518
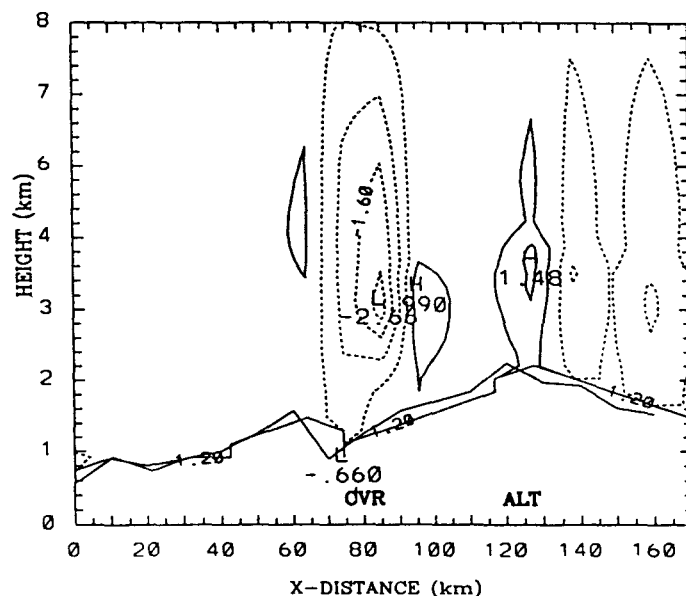


Figure 2.3. – Vertical cross section through the Mogollon Rim at Allen Lake Tank (ALT) along the 225° southwest flow axis on March 15, 1987, showing the stable flow channel structure (a) and vertical motion field (b) contours intervals are 0.7 m s⁻¹. Arrows show airflow through the flow channels. Numbers show the flow channel from 1 in the lowest 50 mb agl to 12 at the top of the flow channel domain. The midflow channel is shown by level **7**.

ARIZONA AIRFLOW MODEL. FLOW CHANNEL
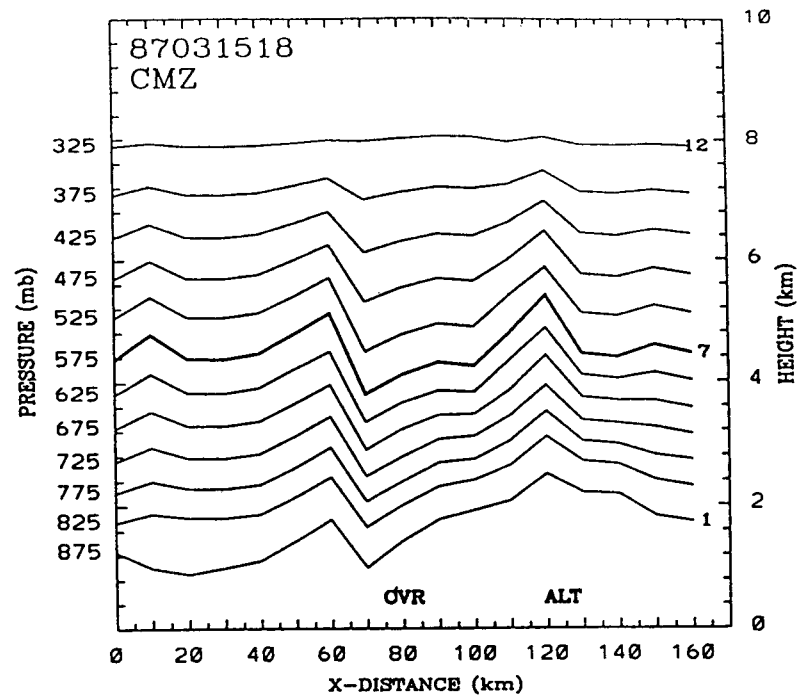
87031518
CMZ



b ARIZONA MODEL. Cross-section
VERTICAL VEL. (M/S)
CMZ 87031518



Figure 2.4. – Same as 2.4 showing sensitivity to unstable conditions with the unstable-neutral flow channels providing more lifting than stable channels.

components perpendicular and parallel to the barrier. Plots from this processor are used throughout this chapter to illustrate model features and describe various model simulations. Further information regarding the program is described in Appendix A.

**2.1.3 Model Physics.** – The AAIM model provides a coarse resolution analysis of kinematic structure based on observed winds and theoretical plume transport and diffusion, using the Pasquill-Gifford model's (Turner, 1969) neutral stability curves. The domain is extended from the vertical slice perpendicular to the mountain barrier of interest into a quasi-three-dimensional domain. The $x$-axis is transverse to the barrier and the $y$-axis is parallel to the barrier. The terrain profile along the $x$-axis is assumed to be invariant along the $y$-axis. The domain is divided into 17 10-km grid spaces along the $x$- and $y$-axes, for a total of 289 grid points. Modeled wind and temperature structure are also assumed to be homogeneous along the $y$-axis. In regions with a simple barrier these assumptions may be applied. Vertical integration is performed at 12 levels above the surface along flow channels described in section 2.1.4. Results are then interpolated to a fixed 200-m vertical grid. Microphysical computations are based on parameterizations for different types of ice crystals and growth processes described in section 2.1.5. The simulation of ground and airborne seeding is described in section 2.1.6.

Computations of airflow and ice crystal nucleation and growth are performed in a series of subroutines within the model (fig. 2.5). The model is initialized with an observed sounding of temperature, dewpoint, and wind direction and speed as functions of height from the surface to the 300-mb level (about 9200 m m.s.l.). The model may use one or two soundings to represent conditions over the barrier. Results are generally better when two soundings are used to adjust the flow as described in section 2.1.4. Sounding data are interpolated to uniform pressure intervals and used to define flow-channel characteristics of temperature, relative humidity, and winds over the barrier. The scientist selects the type of seeding method used in the simulation: airborne or ground-based. Then the model computes the appropriate dispersion rate of seeding material, the point where nucleation begins, and the growth and fallout trajectory of an ice crystal. Finally, a summary tabulation is provided with data files for graphical plots to help interpret the results. The following sections describe the kinematic and microphysical structure of the model. A more detailed flowchart of the model is provided in the User's Guide (app. A).

**2.1.4 Kinematic Structure.** – The surface pressure in the AAIM model is near 900 mb at the southwestern inflow boundary near Phoenix. The model calculates the component of the wind perpendicular to the axis of the barrier in a domain extending from the surface to 600 mb above the ground, i.e., to 300 mb. The airflow at the upper boundary of the model domain (300 mb) is assumed to be horizontal. The barrier-perpendicular $u$-component is determined by assuming conservation of mass flux throughout the domain. The midpoint of the domain is defined at 350 mb above the ground, that is, at the 550-mb level at the upwind boundary. The area below the midpoint is divided into seven channels with 50-mb depth at the inflow location. The $u$-component of each channel is determined by assuming mass flux conservation, such that

$$u_{i,j} = u_{i,1}(dp_{i,1}) \, (dp_{i,j})^{-1}$$

where, $u_{i,1}$ = $u$-component inflow channel $i$ at inflow boundary, $u_{i,j}$ = $u$-component inflow channel $i$ at downwind point $j$, $dp_{i,1}$ = depth of flow channel $i$ at inflow boundary (50 mb), and $dp_{i,j}$= depth of flow channel $i$ at downwind point $j$. Channels with low-level winds, i.e. less than 2.5 m s⁻¹, are considered to be within the "dead layer" of blocked flow; no flow normal to the

10

**Arizona Airflow and Microphysics Model (AAIM)**
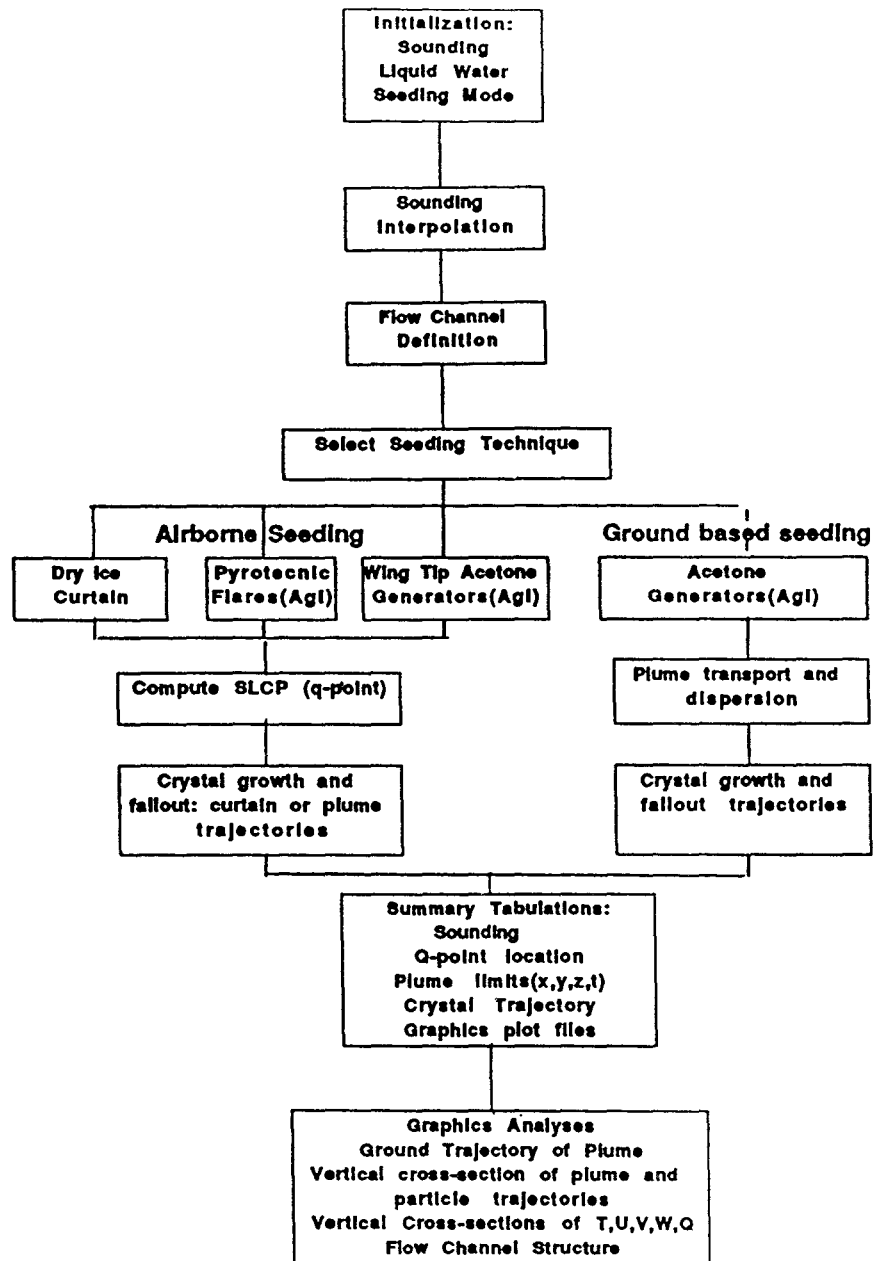


Figure 2.5. – Schematic chart showing the flow of computations in the AAIM model.

barrier is computed for these channels. When this condition occurs, the vertical integration of the mass flux begins at the top of the blocked layer instead of the surface. The profile of the terrain elevation is then adjusted to account for the dead layer. If no downwind observation exists, the region downwind of the crest is simulated by assuming a midchannel profile parallel to the terrain. Winds are then computed by the methods described above. Figure 2.4 shows the vertical cross section of flow channel heights through the Mogollon Rim at HJK along the prevailing 225° southwest flow axis. Note the gravity wave effect of the ridge southwest of the Verde River Valley shown by the wave 10 km southwest of CVR.

11

Above the midflow channel (from 550 to 300 mb), winds are estimated by assuming mass conservation between the midflow channel and the 300-mb pressure surface, which is assumed to be horizontal. This assumption artificially accelerates the winds in the upper channels over the crest; however, these calculations have little effect on the trajectory calculations at 800- to 550-mb levels. Wind components above the midflow channel are estimated by dividing this region into five channels of equal 50-mb pressure depth, and then computing the wind components in a manner similar to that below the midflow channel. The $v$-component of the wind is taken from the upwind sounding, or from two soundings if available, and is assumed not to vary with $y$.

Vertical motion is computed based on the slope of the terrain and flow channels and the $u$-component of the wind. Vertical motion, $w$, is defined as

$$w = u(dh/dx)$$

where d$h/dx$ = slope of the flow channel between grid points

The slope of the terrain to the lee of the crest produces downward flow that parallels the terrain. To the lee of the primary gravity wave upwind of the barrier, similar downward motion generally occurs at the midflow channel level. Lifting associated with the barrier is generally 0.2 to 1.5 m s$^{-1}$ within 20 km of the ridgeline.

Figure 2.3a shows an example of the flow channels under stable conditions and the resulting vertical motion field (fig. 2.4b) for a representative CMZ (composite sounding) on March 15, 1987, at 1800 UTC. Here the channels parallel the surface terrain, forming a standing wave pattern. The mid-point of the first channel, marked by "1" on figure 2.3a, represents the flow in the lowest 50-mb layer. In this case the bottom of the first channel is located at 900 mb and the channel mid-point is at 875 mb. The mid-point of the top channel (12) is located at 325 mb and the model top is at 300 mb. The channels below midflow channel (7) are compressed, resulting in an acceleration of flow over the barrier.

Unstable and neutral conditions produce amplified waves with deeper regions of lifting and increased intensity of vertical motion fields. A sensitivity analysis of the model using the March 15, 1987, composite sounding shows the flow channels for the unstable conditions and the resulting vertical motion field on figure 2.4. Vertical motion is amplified by -0.7 m s$^{-1}$ in the lee of ridges and +0.2 to 0.5 m s$^{-1}$ over the ridges, producing a more distinct wave pattern (fig. 2.4b) than in the stable case. The resulting effects on plume trajectories are discussed in section 2.2.1. In this design, the unstable midflow channel (labeled 7) was 0.2 to 1.1 km higher than the stable midflow channel, which effectively increased the upward momentum transfer and reduced the acceleration created by the restricted flow over the crest. Here the maximum value of the $u$-component over the crest was 9 m s$^{-1}$ less than in the stable case. These changes in the structure of flow over the barrier are generally consistent with more complex Clark model simulations. However, they neither evolve with time, nor show the complex, three-dimensional phase structure predicted by the Clark model for this case as shown in section 2.2.2 and discussed in other theoretical work by Smith (1979).

2.1.5 *Microphysical Structure.* – Seeding is conducted under a variety of cloud temperatures and supersaturations; therefore, a critical feature of targeting is proper determination of crystal fall velocity as a function of particle habit and size. The model uses parameterized

microphysical processes to compute particle growth (Rauber et al., 1988). These computations provide a realistic empirical framework that describes the particle shape, mass, and degree of riming, which determine fall velocities as functions of time. Fall velocities of particles are computed using empirical relationships for various types of ice particles, densities, and mass. Ice crystal growth rates are determined from empirical relationships that are dependent on temperature and supersaturation as described by Hallett and Mason (1958), Kobayashi (1961), Magono and Lee (1966), and Ryan et al. (1976). The AAIM model uses a parameterized routine developed for SCPP, which computes the linear growth rates for basal ($c$) and planar ($a$) crystal axes as specified by measurements of Ryan et al. (1976). CLW (cloud liquid water) production and riming processes are important factors in crystal mass growth and subsequent fallout. Observational relationships are used to estimate the onset time of riming under various liquid water content conditions. These relationships account for the onset of riming on different types of crystals as a function of liquid water content and determine the time required for a particle to become heavily rimed. Several studies have examined the riming process in the Sierra Nevada (Reinking 1974, 1979; Rodi et al. 1985; Prasad 1986). Results from their studies and those of Heymsfield (1982) and Heymsfield and Pflaum (1985) were used to estimate the onset time of riming under various liquid water content conditions. Rodi et al. (1985) developed a relationship that is used in the SCPP and AAIM models today. Their method accounts for the onset of riming on different types of crystals as a function of liquid water content and determines the time required for a particle to become heavily rimed. Rauber et al. (1988) used direct measurements of Brown (1970), Davis (1974), and Locatelli and Hobbs (1974) to develop a set of parameterizations for the particle fall velocity used in the SCPP model targeting calculations. Elliott et al. (1978) described this plume model in greater detail as applied to the SCPP. Two limitations of the model's microphysical design are its failure to describe ice crystal concentrations and explicitly compute the CLW. CLW is specified by the user when the model is executed. These limitations are discussed in section 2.2.5, model limitations.

Fall velocity of ice crystals can then be determined as a function of the crystal habit, axis size, and degree of riming. Table 2.1 shows the fall velocity equations used in the model and the references for each relationship. Table 2.2 shows the temperature and particle axis dimension criteria used to select the appropriate fall velocity equation for the four different ice crystal types simulated in the model.

13

Table 2.1. – Fall velocity ($V_t$  m s$^{-1}$) equations as a function of crystal major axis (centimeters).

| Type | Equation | Reference |
|---|---|---|
| 1. Dendrite, unrimed | $V_t = 0.6197a^{0.217}$ | Brown (1970) |
| Dendrite, rimed | $V_t = 1.32a^{0.330}$ | Locatelli and Hobbs (1974) |
| 2. Plate, unrimed | $V_t = 2.96a^{0.824}$ | Davis (1974) |
| Graupel | $V_t = 3.34a^{0.460}$ | Locatelli and Hobbs (1974) |
| 3. Column unrimed (c<0.09 cm) | $V_t = 24.3c^{1.309}$ | Davis (1974) |
| Column unrimed (c>0.090.09 cm) | $V_t = 3.99c^{0.56}$ | Locatelli and Hobbs (1974) |
| Column rimed | $V_t = 3.99c^{0.56}$ | Locatelli and Hobbs (1974) |
| Column rimed (c>0.2 cm) | $V_t = 1.62$ | Locatelli and Hobbs (1974) |
| 4. Needles unrimed (0<c<0.1 cm) | $V_t = 5c$ | Brown (1970), Nakaya (1954) |
| Needles unrimed (0.1<c<0.2 cm) | $V_t = 2.1c + 0.29$ | Brown (1970), Nakaya (1954) |
| Needles unrimed (0.2<c<0.35 cm) | $V_t = 1.2c + 0.47$ | Brown (1970), Nakaya (1954) |
| Needles unrimed (c>0.35 cm) | $V_t = 0.89$ | Brown (1970), Nakaya (1954) |
| Needles (rimed or aggregated) | $V_t = 1.5V_t$ (unrimed) | Brown (1970), Nakaya (1954) |

Table 2.2. – Temperature and size criteria
used to determine crystal type.

| Temperature (°C) | Axis | Crystal type |
|---|---|---|
| ≤-13 | $a$-axis ≥ $c$-axis | dendrite |
| >-13 | $a$-axis ≥ $c$-axis | plate |
| <-6 | $c$-axis > $a$-axis | column |
| ≥-6 | $c$-axis > $a$-axis | needle |

Four particle growth stages from nucleation to crystal fallout are parameterized to simulate the evolution of a precipitation particle. Diffusional growth along the $c$- or $a$-axes is simulated from nucleation to 300 s using a 60-s time-step. No riming is permitted. A 60-s time step is sufficient to resolve the fall velocity and effect of horizontal wind changes along the fallout trajectory. The fall velocity after 300 s is either that for a plate ($a$-axis ≥ $c$-axis) or a needle ($c$-axis > $a$-axis). At this time the crystal habit is established and this habit is retained for the remainder of the trajectory. Diffusional growth continues until the onset of riming, which is a function of liquid water content specified in the initial conditions. The third stage of growth extends from the onset of riming to heavy rime coverage. Diffusional growth continues; but, in addition, a smooth transition from fall velocity for unrimed to that of rimed particles is calculated as

$$V_t = AV_{tr} + (1 - A) V_{tu}$$

where

$$A = (t - t_0) / (t_r - t_0)$$

where:   $t$ = current time

$t_0$ = time of onset of riming

$t_r$ = time when heavy rime coverage developed

$V_{tr}$ = fall velocity of the rimed particle

$V_{tu}$ = fall velocity of the unrimed particle

The final growth stage extends from the heavy rime coverage to impact with the ground. Diffusional growth along the major axis continues as the particle falls as a rimed crystal. Figure 2.6 shows a composite of terminal velocity functions for the four crystal types used in the model.
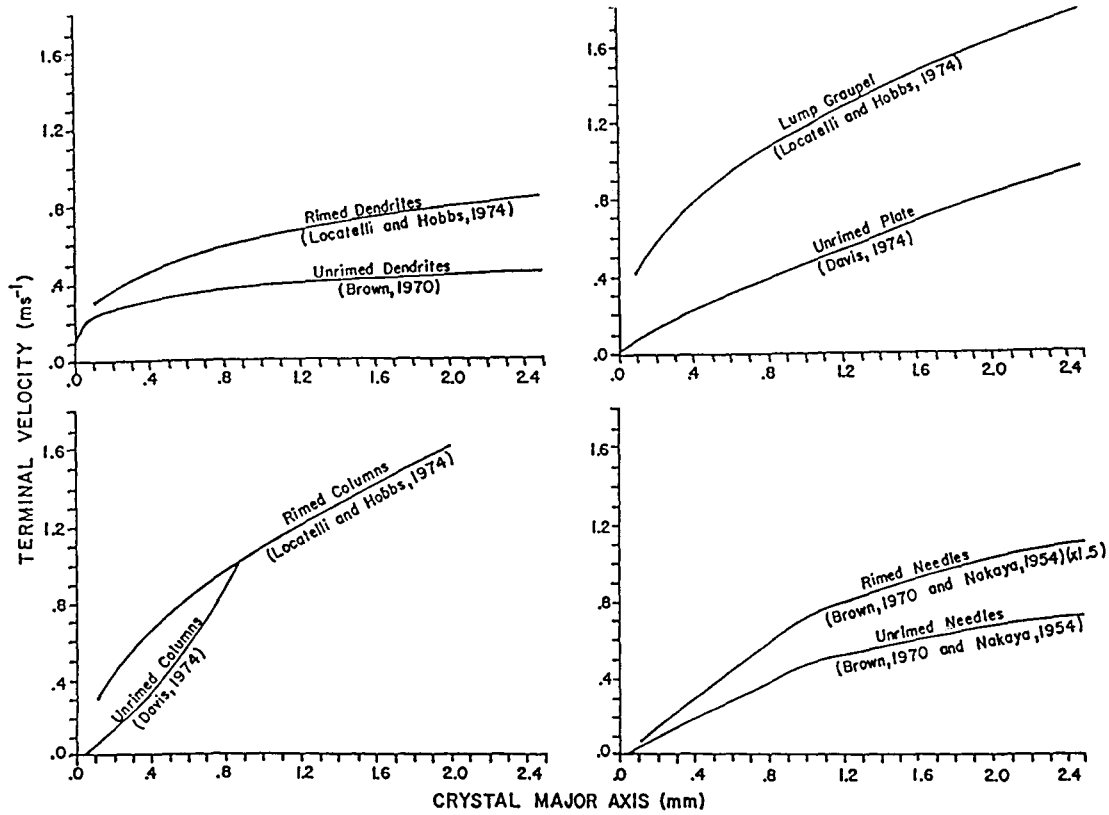


Figure 2.6. – Composite of terminal velocity functions for the four crystal types used in the model. These significant changes in terminal velocity for different types of the crystals control ice crystal trajectories (from Rauber et al., 1988).

**2.1.6 Simulation of Seeding Techniques.** – Conditions at the time of seeding, i.e., airflow, stability, temperature, cloud-base height, and the local terrain orientation to the wind, determine the methodology used for seeding. Proper selection of the optimum seeding technique, location, and time are critical to the success of the seeding experiments. Controlling

factors vary during a given day because of rapidly changing conditions within a precipitation event. Thus, the need for interactive decision making using automated assimilation of observations and model results.

Both ground and aircraft seeding are simulated. Three types of seeding are modeled to simulate the effect of dry ice ($CO_2$), droppable pyrotechnics (AgI), or airborne or ground acetone generators (AgI). Ground-based seeding is simulated using point source plumes from assumed generator sites. Generators are assumed at the 1987 $SF_6$ sites and three additional test sites along the Mingus Mountain ridge west of the Verde Valley. Plume transport and diffusion are simulated using the Pasquill-Gifford model for neutral stability (Turner, 1969). This model assumes a gaussian distribution of nuclei across a three-dimensional plume. This distribution is empirically described as a function of turbulence and mean horizontal wind speed. The horizontal width of the plume is calculated at the altitude of the two-standard deviations (sigma) concentration line. The actual plume would likely be narrower at the seeding level. The top height of the plume is assumed to be the surface at which the concentration is two standard deviations (2-sigma) lower than that on the centerline, accounting for horizontal displacement caused by wind shear. Dennis (1980) describes the engineering considerations for ground-based seeding generators and application of the gaussian plume models to ground seeding simulations.

Computations of $CO_2$ and pyrotechnic seeding effects on crystal fallout include the effects of vertical dispersion of seeding material, vertical wind shear within that depth, variations in saturation vapor pressure, and changes in liquid water content as crystals fall along their trajectories. Variations in the AgI activation rates are not considered. Variations in the particle fall velocities caused by different growth rates are accounted for by a series of five particles with different fall velocities determined by the following parameterization

$$V_{tn} = 0.1(n + 6)V_t, \quad n = 1, 2, 3, 4, 5$$

where: $V_{tn}$ = fall velocity of particle $n$

$V_t$ = standard terminal velocity calculated from the equations in table 2.1

To estimate the nucleation effects through the depth of a seeding curtain of $CO_2$ or AgI, calculations for six depths are simulated from top to bottom of the curtain that would range from 200 to 1200 m deep. Rauber et al. (1988) found that 20-gm AgI flares fell consistently about 1000 m, while $CO_2$ pellets generally fell from 600 to 1000 m below the aircraft before subliming completely. These depths are labeled 1 from the top to 6 at the bottom of the curtain as shown on figure 2.7. Trajectories are typically computed from the center and end points of the seeding line. The end points are based on a 20 percent error in wind direction. As the trajectories of particles become longer with increased wind speed, the length of the seedline is proportionally increased according to table 2.3. Maximum seedline length is 37 km (20 n mi), equivalent to about 10 min of flight time while flying at 120 knots. The seedline length must be determined to maximize the effects of seeding over a target of specific size, and is a function of target surface area and aircraft performance.
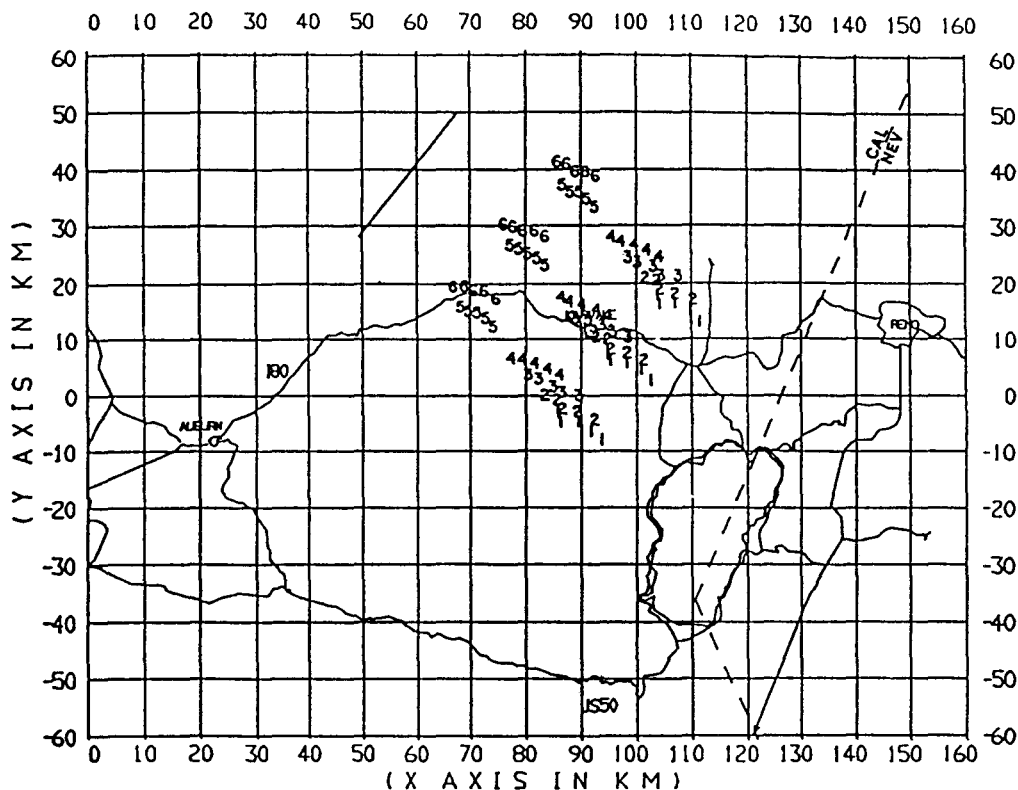
Figure 2.7. – Example of crystal trajectories from an aircraft seedline. Crystals were labeled 1 from the top to 6 at the bottom of the curtain at the center and endpoints of the seedline. The seedline is along the line marked by Q. Five different release times are shown for each set of crystals to block the area in which seeding is likely to have an effect (from Rauber et al. 1988).

Table 2.3. – Seedline length versus trajectory length (T) used in SCPP fixed target experiments.

| Trajectory length (T) (km) | Seeding line length [km (n mi)] |
| --- | --- |
| T < 10 | 10 (5) |
| 30 > T ≥ 10 | 19 (10) |
| 45 > T ≥ 30 | 28 (15) |
| T ≥ 45 | 37 (20) |

Acetone seeding generators may be used when aircraft fly in or near the supercooled region of the cloud and vertical mixing within the cloud is expected to disperse the seeding material throughout the supercooled region of liquid water. Targeting computations of the narrow continuous plume of AgI from the acetone generator differed from the curtain calculations for particle fall velocity. The crystal growth was initiated at the flight altitude 5 min after release of nuclei to account for laboratory measurements of nucleation rates by Demott et al. (1983). Five groups of crystals were simulated to describe the range of fallout points downwind of the seedline. These groups represented parcels at 0, 5, 10, 15, and 20 min downwind of the line.

17

Deshler and Reynolds (1987) found that this procedure appeared adequate for the Sierra Nevada.

## 2.2 Evaluation of Model Performance

The following sections present an evaluation of the AAIM model predictions of airflow and ice crystal trajectories. Model sensitivity to stability parameterizations and representative soundings is presented in section 2.2.1. Section 2.2.2 examines the validity of diagnosed airflow, based on modeled plume trajectories and aircraft observations of tracer gas released at five sites on 6 days in 1987. Further verification was documented in comparisons with the coarse resolution ($dx = dy = 4$ km, and $dz = 0.5$ km) Clark model analyses of 3 intensive case study days. Section 2.2.3 gives case study analyses of the microphysical properties of 5 days where clouds developed and aircraft data were available for verification of model predictions. One well documented heavy snowstorm which grounded the aircraft is also analyzed. Results are then summarized in section 2.2.4, which provides a composite evaluation of model performance for all model runs using the existing aircraft observations for verification.

Data used in the model evaluation were obtained from the ASAP 1987 field project. The project headquarters and base of aircraft operations were located at the Prescott airport. The highly instrumented Beechcraft King Air 200T turboprop, owned and operated by the University of Wyoming, flew microphysics and transport and diffusion missions as described by Super et al. (1989). Soundings were routinely observed during the ascent from Prescott to the target area and on descent upon return. Special aircraft soundings were made as conditions warranted at six locations over the Rim. Table 2.4 shows the locations and map symbols used for field facilities, soundings, $SF_6$ release points used in the 1987 experiment, and potential seeding generator sites and ground facilities at ALT and Mormon Lake planned for future field experiments. Sites A1-A4 and B4 were used to evaluate the model predictions of plume location and depth.

Table 2.4. – Locations of field facilities, soundings, SF$_6$ sites, and seeding generator test sites.

| Facility type | Site name | Symbol | Location Latitude (°) | Latitude (') | Longitude (°) | Longitude (') | Elevation (m m.s.l.) |
|---|---|---|---|---|---|---|---|
| Intense ground observations | Happy Jack | HJK | 34 | 44.78 | 111 | 24.50 | 2286 |
| Future field observations | Allen Lake Tank | ALT | 34 | 49.45 | 111 | 26.40 | 2270 |
| Future radar site | Mormon Lake | ML | 34 | 54.05 | 111 | 26.43 | 2213 |
| Prescott Airport VOR | Prescott | PRE | 34 | 42. | 112 | 28.5 | 1534 |
| SF$_6$ release site | Cherry Road | A1 | 34 | 34.25 | 112 | 4.27 | 1524 |
| SF$_6$ release site | Yavapi Road | A2 | 34 | 29.10 | 111 | 36.98 | 1844 |
| SF$_6$ release site | Forest Road | A3 | 34 | 21.87 | 112 | 23.02 | 1650 |
| SF$_6$ release site | Mingus Mountain | A4 | 34 | 42.52 | 112 | 8.85 | 2142 |
| Western line of generators | Squaw Peak | B1 | 34 | 28. | 111 | 54.5 | 1524 |
| Western (future option) | Tule Mesa | B2 | 34 | 22. | 111 | 50. | 1989 |
| Western (future option) | S. Tule Mesa | B3 | 34 | 20.5 | 111 | 47.5 | 1951 |
| Western (future option) | Payson Airport | B4 | 34 | 15.40 | 111 | 20.33 | 1572 |
| Aircraft sounding | Prescott Ascent | PRA | (exact locations vary with aircraft flight tracks) | | | | |
| | | PRZ | (Prescott composite aircraft soundings) | | | | |
| Aircraft sounding | Prescott Descent | PRD | | | | | |
| Aircraft sounding | Happy Jack West | HJW | | | | | |
| Aircraft sounding | Happy Jack | HJK | | | | | |
| Aircraft sounding | Happy Jack East | HJE | | | | | |
| Aircraft sounding | Payson | PAY | | | | | |
| Aircraft sounding | Payson West | PAW | | | | | |
| Aircraft sounding | Camp Verde | CVA | | | | | |
| Rawinsonde site | Camp Verde | CVR | 34 | 0.5 | 111 | 46. | 1027 |
| Rawinsonde site | Winslow | INV | 35 | 2. | 110 | 43.5 | 1505 |
| Rawinsonde site | Tucson | TUS | 32 | 10. | 110 | 54. | 862 |
| Composite soundings | Clark model[1] | CMZ | 34 | 0.5 | 111 | 46. | 1027 |

[1] Soundings composited from all available information on case study days by Bruintjes et al. (1991).

**2.2.1 *Model Sensitivity Analyses*.** – This section presents examples of model sensitivity to different stability criteria and initial synoptic scale soundings. The following section 2.2.2 provides additional examples. Figure 2.8 shows the different trajectories for plumes under stable and unstable-neutral conditions simulated using the composite sounding for March 15, 1987. Note the unstable plume cross sections for generators A2 and A4 and the resulting crystal trajectories that fell out 5 and 10 km earlier than in the stable simulation. This example shows the effect of stable and unstable-neutral conditions on model calculations of crystal trajectories. Stability affects the flow channel heights over a barrier and their separation, thereby controlling the height of nucleation and the wind speed and direction that carries the crystals. In addition, the relatively compressed stable flow channels accelerate the low-level flow over the crest more than the less compressed unstable channels as shown on figures 2.9a,b. Flow channels for this case were shown on figures 2.4a and 2.5a.

**a** Plume and Crystal Trajectory
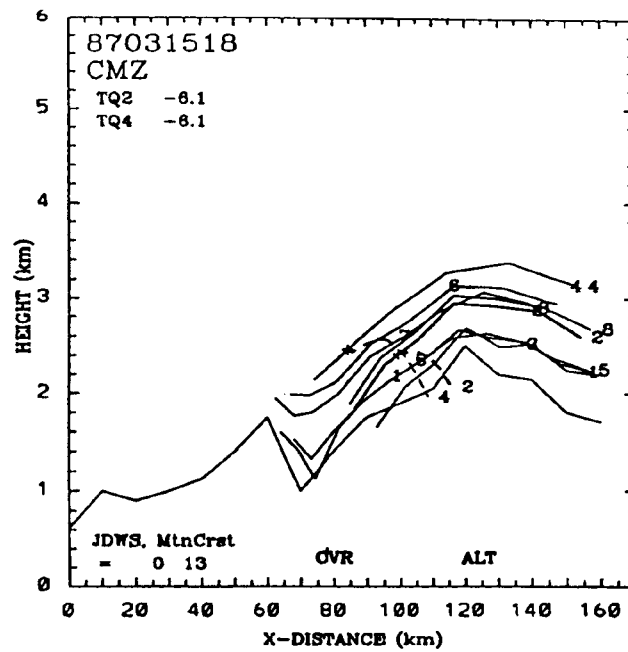
**Stable**



**b** Plume and Crystal Trajectory
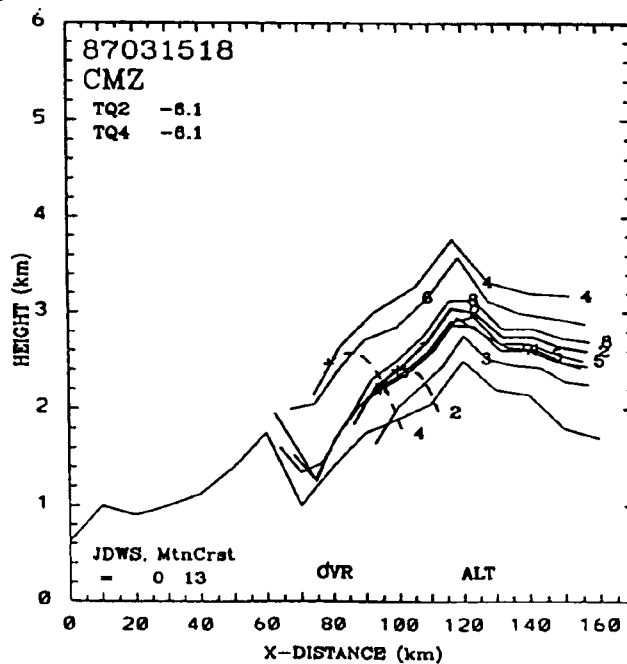
**Unstable**



Figure 2.8. – Vertical cross section of plume trajectories for stable (a) and unstable (b) conditions simulated using the composite sounding for March 15, 1987. Crystal trajectories from generators at **A2** and **A4** are shown by dashed lines. Numbers along trajectories show seeding generator sites shown in figure 2.1 and 1-h positions of particles in plume. The stable case produced crystals that fell out closer to the crest than the unstable case.

**a** ARIZONA MODEL: Cross-section
U—WINDS (M/S)
CMZ 87031518

Stable



**b** ARIZONA MODEL: Cross-section
U—WINDS (M/S)
CMZ 87031518
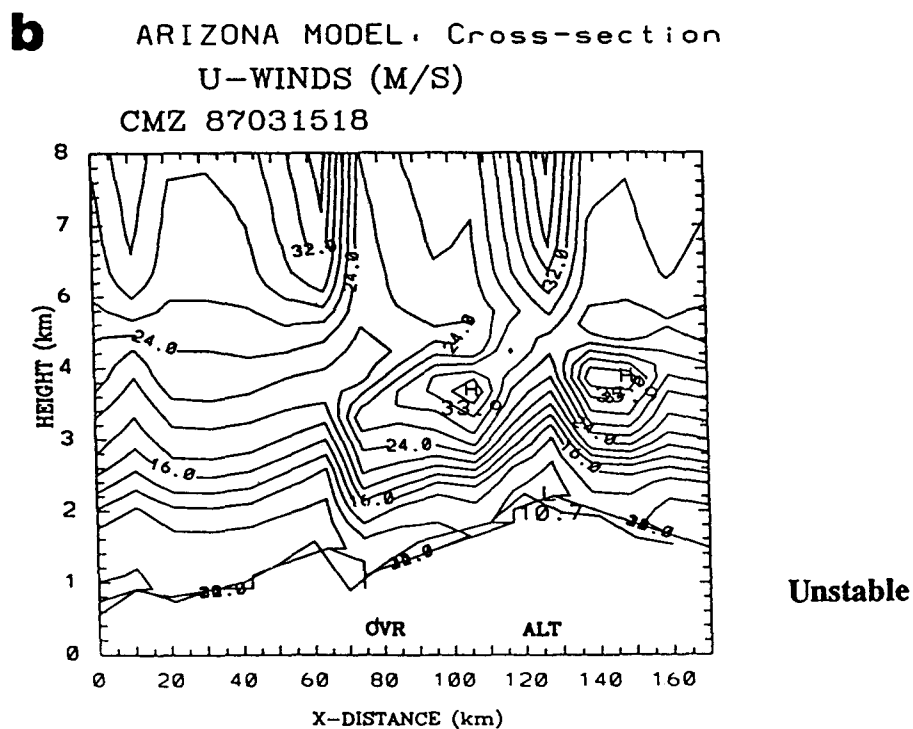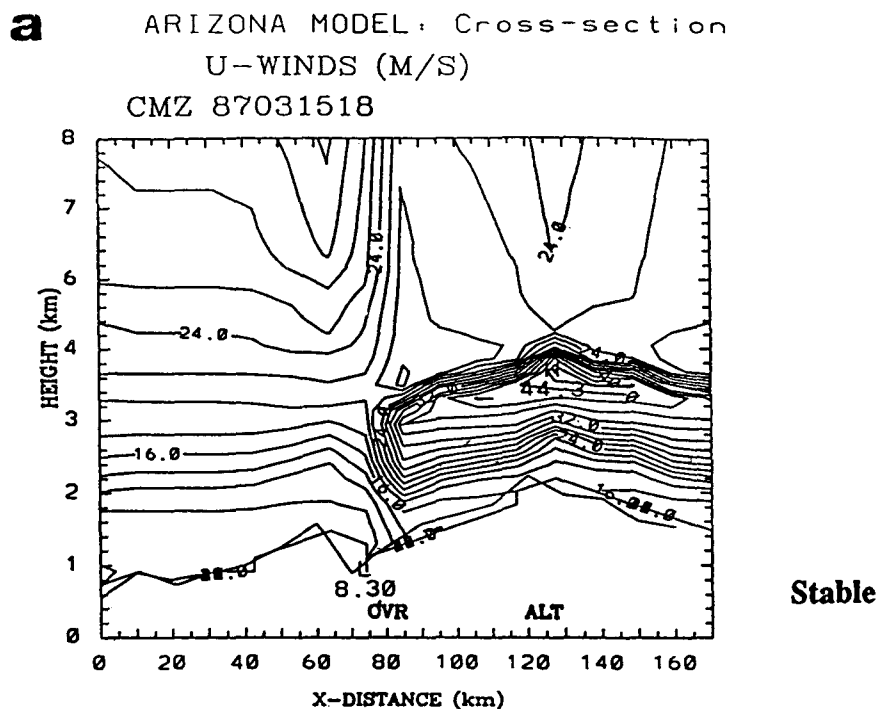
Unstable

Figure 2.9. — Wind component normal to the barrier (*u*-component) showing
acceleration of flow over the crest on March 15, 1987. Larger acceleration
occurs in the more compressed stable channels (**a**) than in the less
compressed unstable flow simulations (**b**). Isolines have contour intervals at
2 m s$^{-1}$.

21

An analysis of model sensitivity to soundings on March 15, 1987, showed subtle differences in the modeled airflow and important temperature effects on the modeled ice crystal evolution. Simultaneous synoptic-scale National Weather Service soundings at TUS (Tucson) and INW (Winslow), Arizona, were used to initialize the model using stable flow channels. When TUS was used alone, the results were slightly different from those with INW used as a downwind sounding at 1200 UTC in the case with a broad uniform southwesterly flow. Figure 2.10 shows the subtle differences in plume track. Numbers along the plume edge indicate the plume location at 1-h intervals. The bold plume boundaries indicate the plume from a test $SF_6$ release site. The warmer temperatures at TUS prevented simulation of nucleation and crystal growth and resulted in a slightly deeper midflow channel height with a model top flow channel that was 0.7 km higher than the channel predicted from the CMZ sounding (see figs. 2.8 and 2.17). The warm TUS and INW soundings did not represent the cooler Mogollon Rim conditions observed by aircraft and CVR soundings. Plume trajectories were deeper than the stable CMZ simulation and closely resembled the stable CMZ analysis. The maximum $u$-component here also matched the stable maximum over the crest; however, the TUS case veered more with height, producing a 20° eastward shift in the plume track. These examples show the importance of using the most representative sounding for the region simulated. Natural variations in winds, temperatures, and stability produced important differences in model results. Model sensitivity to these variables using local soundings is clearly demonstrated by the case studies in section 2.2.2.

**2.2.2 Verification of Airflow Simulations.** – Special atmospheric dispersion and airflow studies were conducted on six days in Arizona during the 1987 field experiment. These studies were designed to estimate the potential for seeding with ground-released ice nucleation agents through tracer transport and diffusion studies (Super et al. 1989). An instrumented aircraft made downwind measurements of $SF_6$ tracer gas. All observational comments in this section are based on the final report by Super et al. (1989). Table 2.5 shows the location and times of $SF_6$ releases from the ground. Observational data sets were not complete because of the limitations of soundings, aircraft observations, and surface networks, which did not continuously monitor all areas of the Rim during periods of interest.
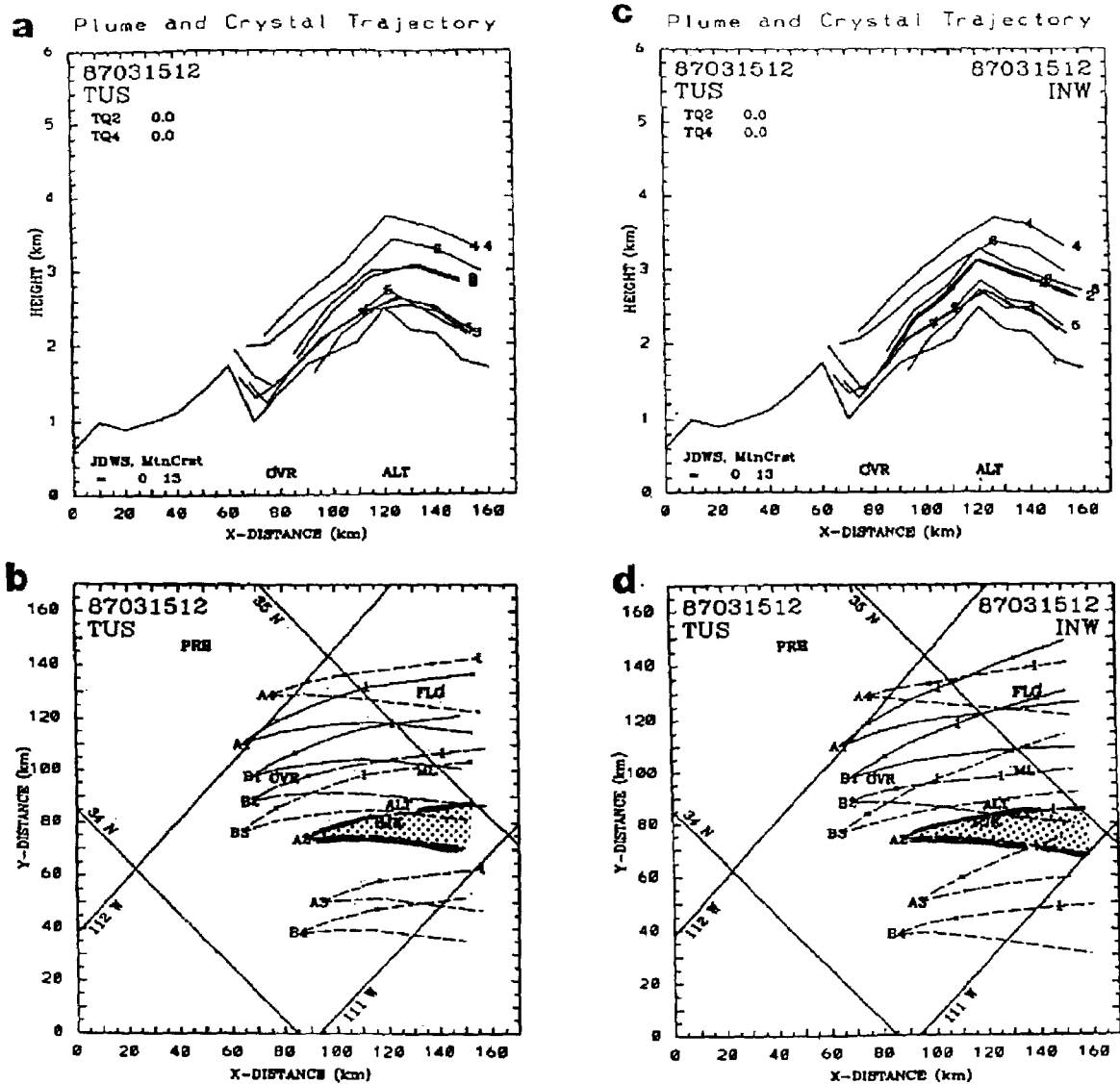
Figure 2.10. – Plume trajectory sensitivity for the stable simulations using synoptic soundings at Tucson (TUS) and Winslow (INW) observed on March 15, 1987, at 1200 UTC. Horizontal positions of the plumes from eight generator sites are marked by numbers at 1-h intervals. Note the decreased speed with the downwind INW sounding in figure 2.10 d. The stippled area shows the plume from A2 passing over HJK.

Table 2.5. – 1987 SF$_6$ observation times, release locations, and mean surface winds.

| Date | Time | Site | Direction (°) | Speed (m s$^{-1}$) |
|------|------|------|-----------|-------|
| February 3 | 1840-2250 | A2 | 190 | 10 |
| February 15, 16 | 2238-0115 | A2 | 180 | 5 |
| March 2 | 1754-1918 | A3 | 190 | 2 |
| March 5 | 2100-2322 | B4 | 180 | 2 |
| March 9 | 2245-0110 | A4 | 190 | 5 |
| March 15, 16 | 2145-2340 | A2 | 210 | 5 |

Table 2.6 shows a summary of the observed plume top height and plume width as it passed over HJK and model predictions at HJK. The distance from the edge of the plume (defined by the model for the two sigma concentration line) to HJK is indicated in the $dx$ and $dy$ columns. A negative $dx$ indicates that the plume was west of HJK while a negative $dy$ shows that the model prediction was to the south. The model performed well when compared with the analyses from the aircraft data performed by Super et al. (1989).

Table 2.6. – Comparison between the AAIM model and observed plume properties.

| Date | Station | Time (UTC) | Observed top height (km m.s.l.) | Plume maximum width (km) | Model top height (km) | Plume width (km) | Location of plume edge from HJK | |
|------|---------|------------|----------------------------------|---------------------------|------------------------|-------------------|--------------------------------------|---|
| | | | | | | | Distance $dx$ (km) | Distance $dy$ (km) |
| **Primary ICS used in Clark Model Comparisons** | | | | | | | | |
| February 3 | CVR | 1200 | 3.2 | 9.5 | 2.98 | 7 | 0 | 0 |
| | CVR | 2000 | | | 3.10 | 10 | 0 | 0 |
| | CMZ | 1800 | | | 2.93 | 7 | 0 | 0 |
| February 15 | CVR | 18 | 2.95 | 12 | 3.3 | 9 | -12 | -13 |
| | CMZ | 18 | | | 3.02 | 7 | -6 | -15 |
| | CVR | 21 | | | 2.91 | 10 | -2 | -7 |
| February 16 | CVR | 00 | | | 2.5 | 10 | -2 | -10 |
| | CVR HJW | 00 | | | 3.32 | 8 | 2 | 0 |
| March 15 | CVR | 12 | 3.4 | 11 | 2.9 | 10 | 0 | 0 |
| | CVR HJK | 15 | | | 3.2 | 7 | 18 | 0 |
| | CMZ | 18 | | | 2.94 | 8 | 0 | 0 |
| | CMZ | 21 | | | 3.01 | 8 | 0 | 0 |
| | CVR HJK | 22 | | | 3.2 | 8 | 0 | -2 |
| March 16 | CVR | 00s[1] | | | 2.92 | 8 | 0 | -2 |
| | CVR | 00n[2] | | | 3.03 | 8 | 0 | -1 |
| **Other SF$_6$ Cases** | | | | | | | | |
| March 2 | CVR | 18 | 3.1 | 12 | 2.44 | 5 | 0 | -38 |
| | PRZ | 18 | | | 2.63 | 6 | 0 | -18 |
| March 5 | CVR | 12 | 2.8 | 12 | 2.8 | 12 | 0 | 0 |
| | CVR | 18 | | | 2.34 | 13 | 0 | 0 |
| March 6 | CVR | 00 | | | 2.83 | 13 | 0 | 0 |
| | CVR | 06 | | | 2.88 | 13 | 0 | 0 |
| March 9 | CVR | 12 | 4.2 | 11 | 2.82 | 13 | -35 | 0 |
| | CVR | 18 | | | 2.72 | 6 | -35 | 8 |
| March 10 | CVR | 00 | | | 3.37 | 7 | -2 | 35 |

[1] s – stable simulation
[2] n – unstable-neutral simulation

Comparisons of observed and model predicted plume height and location shown in table 2.6 indicate the large sensitivity of the model to initial soundings. All soundings used in the comparisons were observed within 12 h of the plume release and within 60 km of the release point. Large temporal and spatial mesoscale (local) variations in wind direction, speed, and stability produced significant differences in many model predictions within this small time and space domain. The plume top height predicted by the model was within 200 m of that observed in four of the six cases. It was underpredicted by 500 to 600 m in the other two cases. Given the resolution of the aircraft data and limitations of the model, these results were considered good.

The targeting of the plume over HJK was more difficult to evaluate. In four of the six cases the modeled plume passed over or within 2 km of HJK as observed; but in the other two it passed ~18 to 38 km to the south and 35 km to the west respectively; in these cases the aircraft terminated observations before reaching HJK. The model performed satisfactorily with most soundings. The following detailed case studies compare model results with field observations.

Results from Clark model simulations by Bruintjes et al. (1993) were used to assess the AAIM model performance for three case studies. The Clark model provides a theoretical basis for comparison with the observed data and the AAIM model simulations. Its three-dimensional, time-dependent simulation of airflow and cloud and precipitation evolution permits an independent check of expected flow and cloud properties over the entire area with a resolution of about 2 km horizontally and 200 m vertically. Three days with the most complete sets of field data were selected for intensive case study comparisons with the Clark model. Analyses were designed to make comparisons between the AAIM and Clark model results and verification data observed by aircraft. Bruintjes et al. (1993) ran the Clark model on a composite sounding, designated as CMZ, which was believed to represent conditions over the analysis domain at the time of the tracer release and subsequent observations. Identical soundings were used to initialize the AAIM model. In addition, CVR rawinsonde and aircraft soundings (CVA, PRA, PRD, PAY, HJK, HJW, HJE) were used to simulate actual conditions from the operational data-stream. These unadjusted data tested the AAIM model's ability to perform under conditions of field operations.

**2.2.2.1** *February 3, 1987: Yavapai Road.* – Steady light southwesterly winds carried the plume from the release site on Yavapai Road (A2) toward HJK under neutral stability conditions. Aircraft observations from 1944 to 2346 UTC detected a well defined plume that passed just northwest of HJK. Analyses of the ascending and descending aircraft passes show the plume structure northwest and over HJK on figure 2.11 from Super et al. (1989). Their analysis was the primary model verification data set for predictions of plume trajectories and depth. Figure 2.11 shows the edge of the plume as defined by detailed analysis of $SF_6$ concentrations observed along the flight tracks within the dashed areas. Figure 2.11a shows the horizontal structure of the plume with $SF_6$ concentrations given in p/t (parts per trillion). The vertical extent of the plume and aircraft sampling points are shown on figure 2.11b. Note that Super adjusted the plume analysis to account for the eastward drift of the plume with time during the flight. Similar analyses were performed for all tracer cases discussed in this report. The reader is referred to Super et al. (1989) for detailed discussions of this case and others.

Figure 2.12 shows the plume trajectories analyzed by the model for February 3, 1987, using the sounding from CVR observed at 2000 UTC. The figure shows the locations of $SF_6$ release points used in the tracer studies in model coordinates. Five sites were used for different tracer case studies in 1987. Three additional sites B1-B3 were tested to examine model sensitivity for future seeding generator locations along the Mingus Mountain ridge. In the plume trajectory figures, plume top heights are marked by numbers 1 to 8 with the numbers plotted at 30-min intervals of plume transport. The numbers 1 to 8 correspond to the seeding generator locations from A1(1) to B4(8), respectively. Horizontal plume positions are marked by numbers from 1 to 3 on the left edge of the plume every 30 min. Plumes from eight generator sites were examined in each case to determine the area covered and differences in plume trajectories diagnosed by the model. Table 2.4 lists the geographic locations and elevations of the eight sites, which are plotted on a map on figure 2.1.

Model predictions from three local soundings all indicated that the plume from A2 passed over HJK and its top was within 250 m of that observed by aircraft. The predicted plume width at HJK was 7 to 10 km for the three soundings in comparison with the observed width of 5 to 7 km for the 3 p/t concentration. The model analysis of the CVR sounding at 2000 UTC produced a plume that passed directly over HJK with its top at 3.2 km as seen on figure 2.12b.
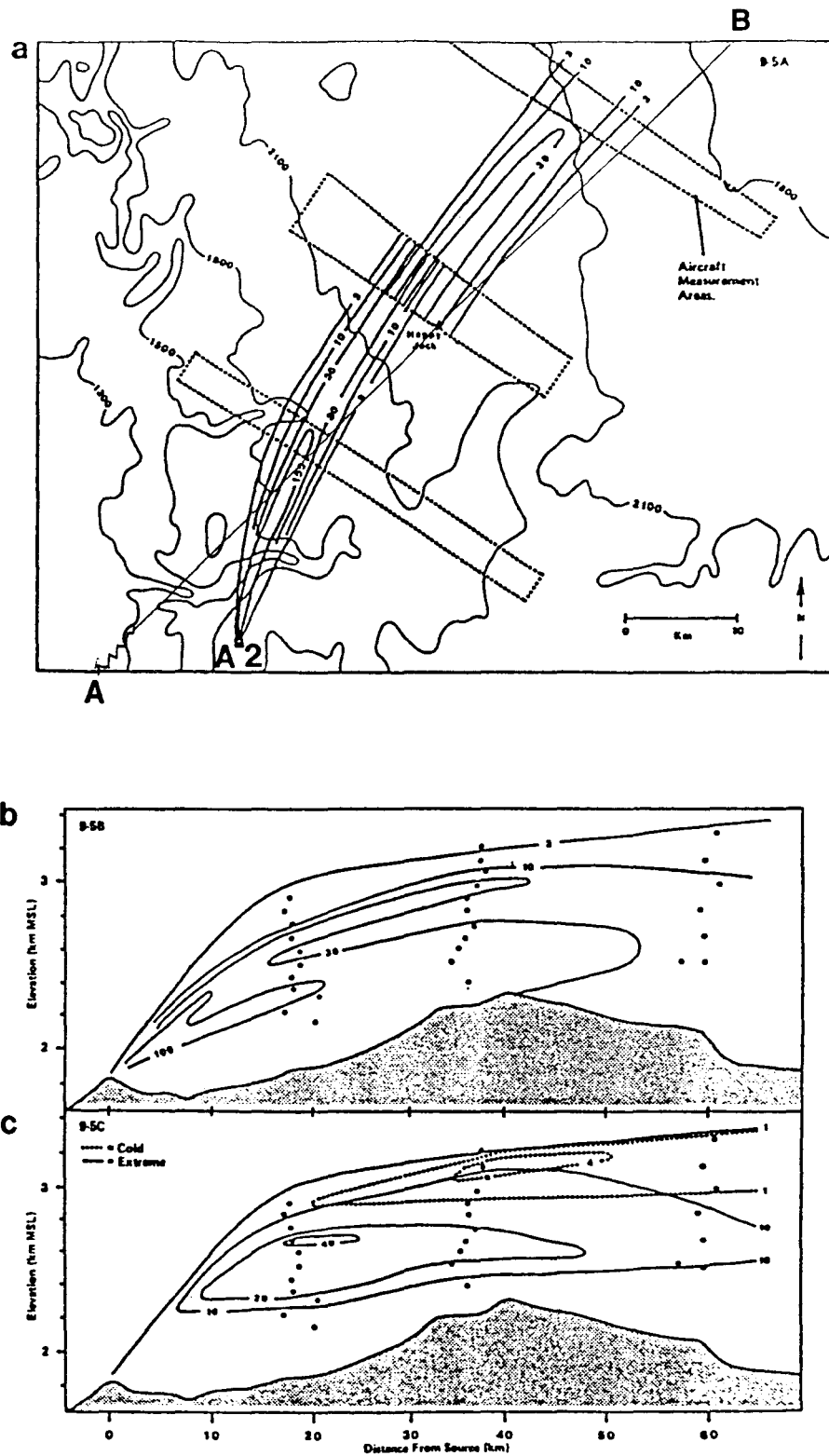
Figure 2.11. – Observed SF$_6$ plume as defined by detailed analysis of SF$_6$ concentrations observed along the flight tracks for the transport and diffusion study on February 3, 1987, (from fig. 9.5 of Super et al., 1989). Line AB shows the location of AAIM grid axis through Happy Jack (HJK). The SF$_6$ release point was Yavapi Point (A2).

**a** Plume and Crystal Trajectory
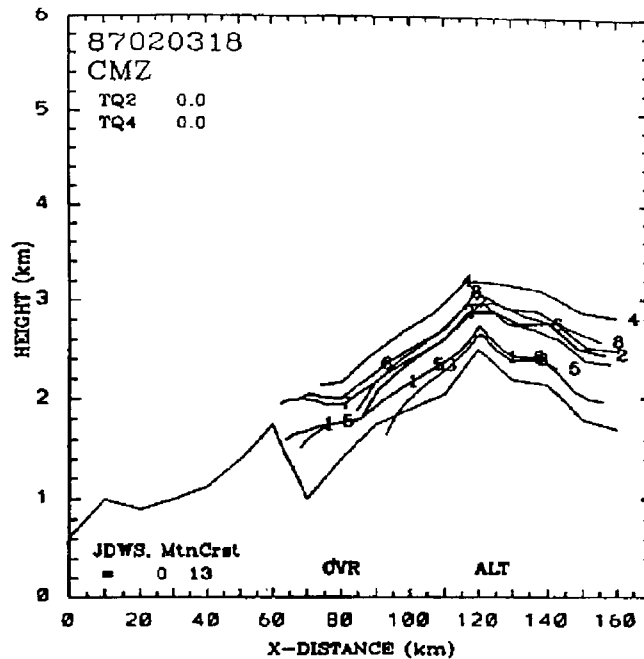


**b** ARIZONA AIRFLOW MODEL - PLUME TRAJECTORY
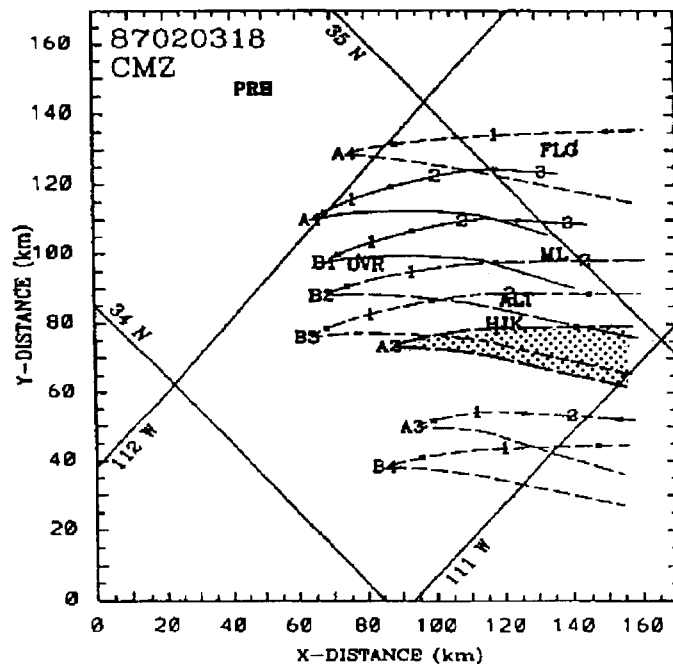


Figure 2.12. – Vertical cross sections (a) and horizontal (b) positions of plume trajectories analyzed by the AAIM model for February 3, 1987, using the sounding from CVR observed at 2000 UTC. The SF$_6$ release point at Yavapi Road is marked by **A2**. The bold lines and stippled area indicate the plume coverage from A2.

The AAIM model analysis using the Clark model composite sounding, CMZ for 1800 UTC February 3, 1987, produced results similar to those from the local soundings (fig. 2.13). The Clark model plume top reached 2.7 km m.s.l. depth and a width of 20 km over HJK after 50 to 60 min of simulated transport and diffusion. In contrast, the AAIM model plume reached HJK after only 40 to 50 min of transport time, and was only 7 km wide. This transport time is consistent with that required for a plume to move with the mean winds from the surface to 2700 m m.s.l., which were from 195 to 210° at 7 to 11 m s$^{-1}$ at 1800 UTC. In this simulation the AAIM model plume passed just to the south of HJK, whereas the Clark model plume passed directly over HJK (marked by the X) as shown on figure 2.14. The broad Clark model plume plotted on figure 2.14 shows the effect of grid point dispersal. This dispersal effectively changes the point source to a grid box of 2 by 2 km dimensions. Winds at the surface and 4 km m.s.l. show a uniform flow field that accelerates over the Rim. Vertical motion on figure 2.14d shows internal gravity waves and local orographic lift on the slope upwind of HJK.

**2.2.2.2  February 15, 1987: Yavapai Road.** – On February 15, 1987, the release of SF$_6$ from this site starting at 2238 UTC was measured during a stratified storm with low cloud water concentrations and no precipitation. This plume passed just to the north of HJK, reached a height of 2.95 km m.s.l., and was 9 km wide at HJK as observed near 2300 UTC. The model indicated a range of conditions and plume tracks based on soundings observed from 1200 UTC February 15 to 0000 UTC February 16, 1987. These variations were consistent with rawinsonde and aircraft wind data. The best plume track was predicted by the CVR and HJW soundings observed at 0000 UTC February 16, 1987. This plume passed just north of HJK and reached 3.3 km m.s.l. and a width of 8 km at HJK. Here the aircraft sounding west of HJK contributed information that significantly improved the model simulation. Without the HJW sounding, predictions from the CVR 0000 UTC sounding produced a strong veering of the flow with height that resulted in a plume position 10 km southwest of HJK.

In the simulation of the CMZ sounding for 1800 UTC, the model also predicted a plume 15 km south of HJK with a top height of 3 km. However, using this same sounding, the Clark model simulated a plume track that drifted over HJK with a core at the 2 km m.s.l. level located southwest of HJK.

**2.2.2.3  March 15, 1987: Yavapai Road.** – On March 15, 1987, from 2145 to 2340 UTC, SF$_6$ was released into a storm that produced snow. This complex case occurred during a frontal passage with instability showers and convective bands whose radar echoes reached 5 to 8 km m.s.l. This case demonstrates the model's ability to simulate crystal fallout trajectories and seeding plume locations during evolving storm conditions. Two flights examined the cloud structure and airflow on March 15, 1987. The first flight studied two prefrontal convective bands from 1417 to 1745 UTC. Liquid water measured by the radiometer reached 0.2 to 0.4 mm during the first flight. This flight observed a variety of ice crystals ranging from a few columns to aggregates of dendrites and graupel particles. Aircraft observations at 4.4 km m.s.l. (-14 °C) showed dendritic crystals and irregulars with most exceeding 1000 μm; the mean IPC (ice particle concentration) was 8 L$^{-1}$ at 1600 UTC. Snowfall of 3 to 5 mm occurred in 3 h. Snowfall rates estimated by aircraft observations varied from 1 to 4 mm h$^{-1}$ in these convective bands.

The second flight examined cloud characteristics and tracked the SF$_6$ plume during a lull in the storm. Southwesterly flow continued from 1200 to 0000 UTC and transported the plume from

**a** Plume and Crystal Trajectory
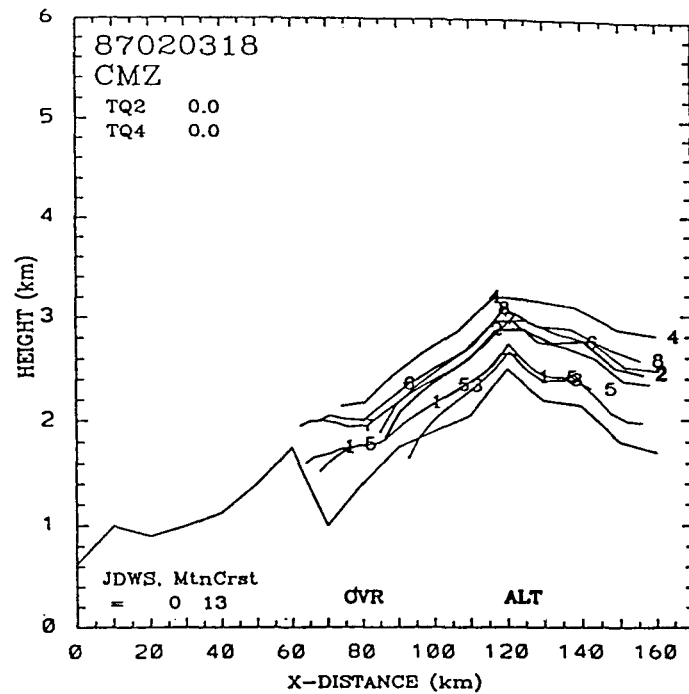


**b** ARIZONA AIRFLOW MODEL · PLUME TRAJECTORY
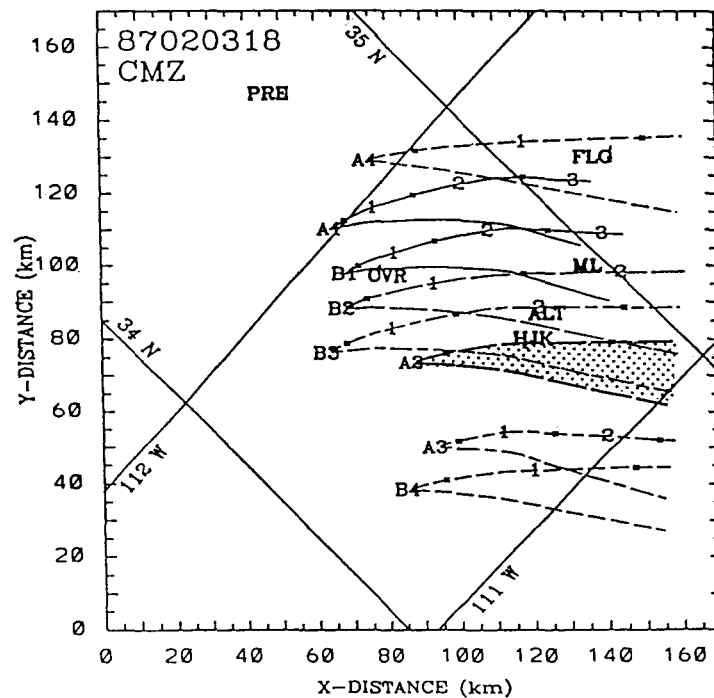
Figure 2.13. – Plume trajectories analyzed by the AAIM model for the Clark model composite CMZ 1800 UTC sounding, for February 3, 1987. Description is the same as figure 2.12.
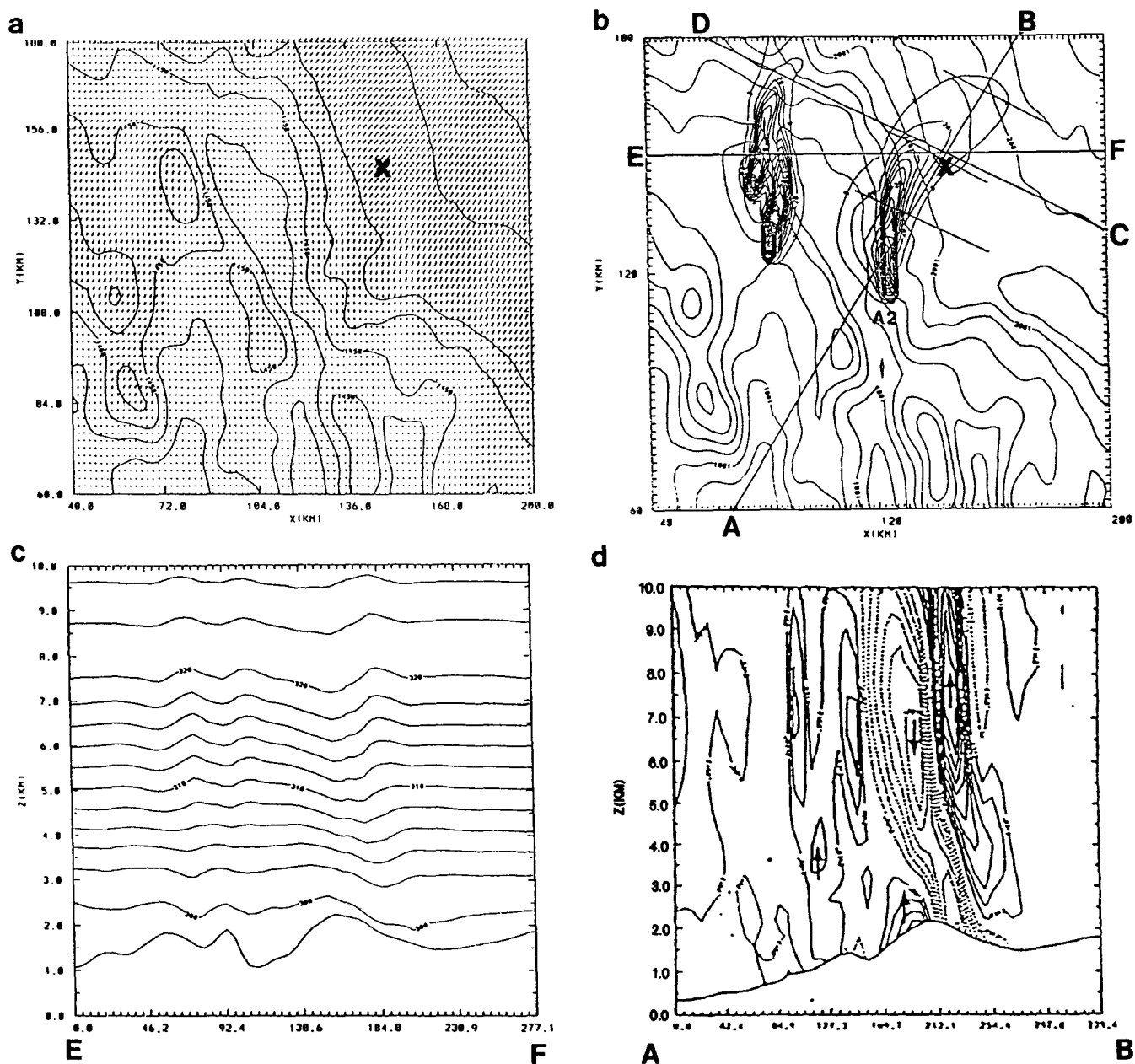
Figure 2.14. – Clark model analyses for February 3, 1987, showing the surface (a) wind field vectors, surface plume concentration field (b), vertical cross sections of potential temperature (°K) (c), and vertical cross-section (d) of the vertical motion field (m s⁻¹). Cross sections are taken along lines AB amd EF (from Bruintjes et al. 1991).

A2 to HJK by 2310 UTC. The maximum plume width of 10 km occurred at a point 20 km downwind of A2; yet, over HJK the width was only 4 km at aircraft flight levels. Aircraft observations showed the plume top height increasing from 3 to 3.4 km m.s.l. over the Rim. The $SF_6$ was detected around 2200 UTC in regions of snow at temperatures below 0 °C. Deep convective clouds were observed with echo tops of 8 km m.s.l. (-45 °C). Rapid changes in

mesoscale convective bands occurred during this period after a frontal passage at 2000 UTC. Supercooled liquid water was observed with radiometer values peaking at 0.25 mm and aircraft JW (Johnson-Williams) measurements at 0.1 to 0.2 g m$^{-3}$. IPC reached 20 to 40 L$^{-1}$ suggesting complex microphysical conditions with deep sources of natural ice crystals in convective bands; however, a large hole in the deep cloud deck was associated with shallow clouds with little or no ice or SLW. Simulation of these rapidly changing convective conditions is well beyond the capabilities of the simple AAIM model, yet it performed reasonably well in this case.

Seven model analyses were made using different soundings observed for this case. Model analysis of the 1200 UTC sounding produced a plume that passed directly over HJK and reached 2.9 km. The crystal fallout point from site A2 was on the lee side of the barrier. Winds were somewhat strong with a $u$-component over the barrier of 20 m s$^{-1}$ at 3.5 km. Results were remarkably consistent for all model runs from the 1200 to 0000 UTC soundings as seen in table 2.6. Figure 2.15 shows the plume trajectory from the upwind CVR sounding at 2200 UTC using the aircraft HJK 2200 UTC downwind sounding. The ice crystal trajectory shown by the dashed line marked 2 resulted in a nearly perfect fallout on the HJK/ALT crest 2 km south of HJK shown on figure 2.15a. In this simulation the model developed a column ice crystal with a $c$-axis that reached 914 μm and an $a$-axis of 153 μm. The fallout altitude was 2364 m, yet the fall velocity reached 1.0 m s$^{-1}$. Aircraft observations at 2200 UTC indicated winds from 210° at ~20 m s$^{-1}$ from 2-3.4 km; these winds increased to 30 m s$^{-1}$ at 5 km m.s.l., where the maximum $u$-component reached 28 m s$^{-1}$ over the crest. The wavelike flow was shown in the $u$-component of the wind and the vertical motion fields. Vertical motion reached a maximum of 1.1 m s$^{-1}$ at 4.5 km m.s.l. over the crest with sharp sinking motion of -2.4 m s$^{-1}$ upwind over the Verde River Valley.

Figure 2.16 shows the plume predicted from the CVR 0000 sounding on March 16, 1987. Numbers along the plume edge show the position of the plume every hour indicating a transport time from A2 to HJK of about 1.5 h. Results from this sounding were comparable to the CVR-HJK analysis, but the northern edge of this plume passed over HJK. Rapid crystal growth produced a needle with $c$-axis dimensions of 1210 μm and $a$-axis of 224 μm, having a fall velocity of 0.5 m s$^{-1}$. This crystal fell short of the crest by 10 km in comparison to the nearly exact targeting from the CVR-HJK sounding run shown on figure 2.15. In the latter case the nucleation occurred at a higher altitude, placing the particle in a faster flow that carried the crystal to the crest. The winds in this example were similar to those for the 2200 UTC case but were weaker over the crest. This case shows the sensitivity of the model to different soundings and the important roles that the dynamics and thermodynamics play.

Two soundings used in the Clark model analyses of this case, one from the 1800 UTC soundings, the other from 2100 UTC data (see fig. 2.17), were examined in the AAIM model. Both soundings produced stronger AAIM model winds than those observed. The plume from the 1800 UTC simulation passed directly over HJK after 30 min, whereas the latter case passed 2 km to the south after 20 min in close agreement with aircraft observations. The CMZ 1800 UTC sounding had slightly stronger winds that were 10 to 15° more southwesterly than the 2100 UTC soundings from CVR and HJK. Thus, a larger $u$-component of the wind at 1800 UTC produced stronger lifting and a 7-m s$^{-1}$ increase in maximum flow over the crest. Interestingly, the crystal fallout trajectories for the CVR 0000 UTC and CMZ 2100 UTC simulations showed a 20-km shift downwind for crystals from A4, but only a 5-km shift for A2 crystals, again illustrating the model sensitivity to subtle changes in airflow. Figures 2.16a and 2.17a show a small downwind shift in the fallout point for A2 crystals. The crystals from A2 were nearly

**a** Plume and Crystal Trajectory
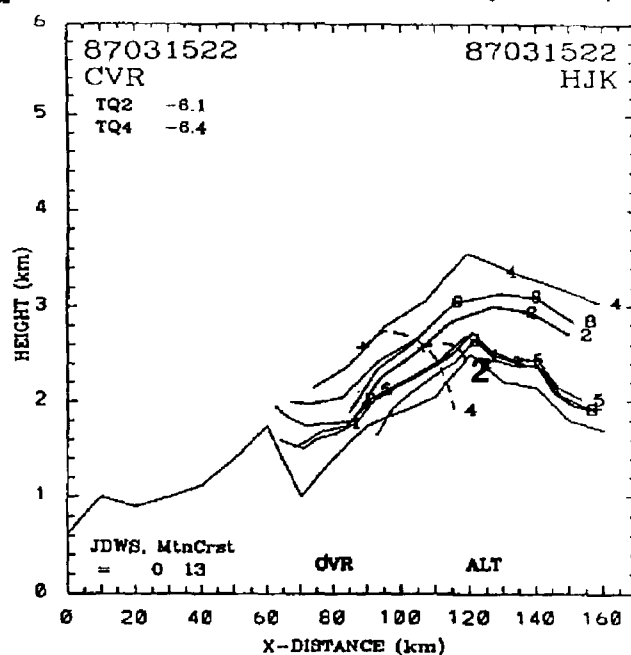


**b** ARIZONA AIRFLOW MODEL. PLUME TRAJECTORY
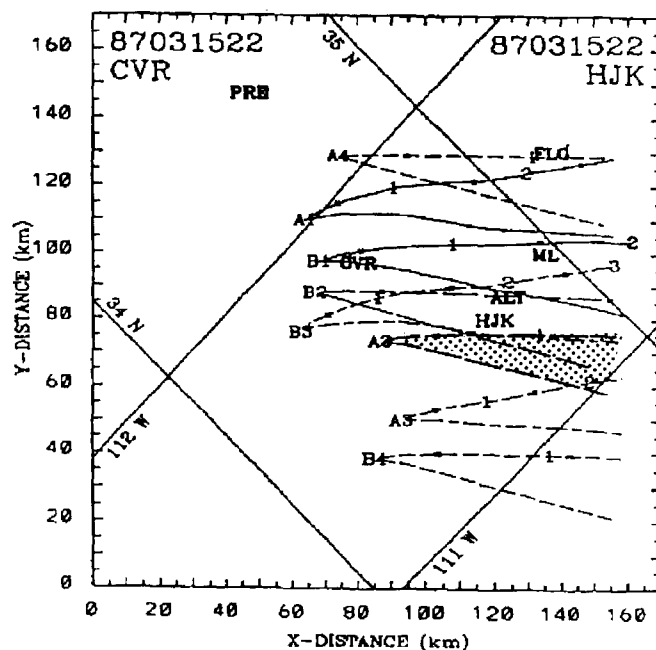


Figure 2.15. – Vertical (a) and horizontal (b) plume trajectories from the upwind CVR sounding at 2200 UTC March 15, 1987, using the aircraft HJK 2200 UTC as the downwind sounding. The ice crystal trajectory in figure 2.15a shown by the dashed line marked 2 resulted in a nearly perfect fallout on the Happy Jack (HJK)/Allen Lake Tank (ALT) crestline, 2 km south of HJK.
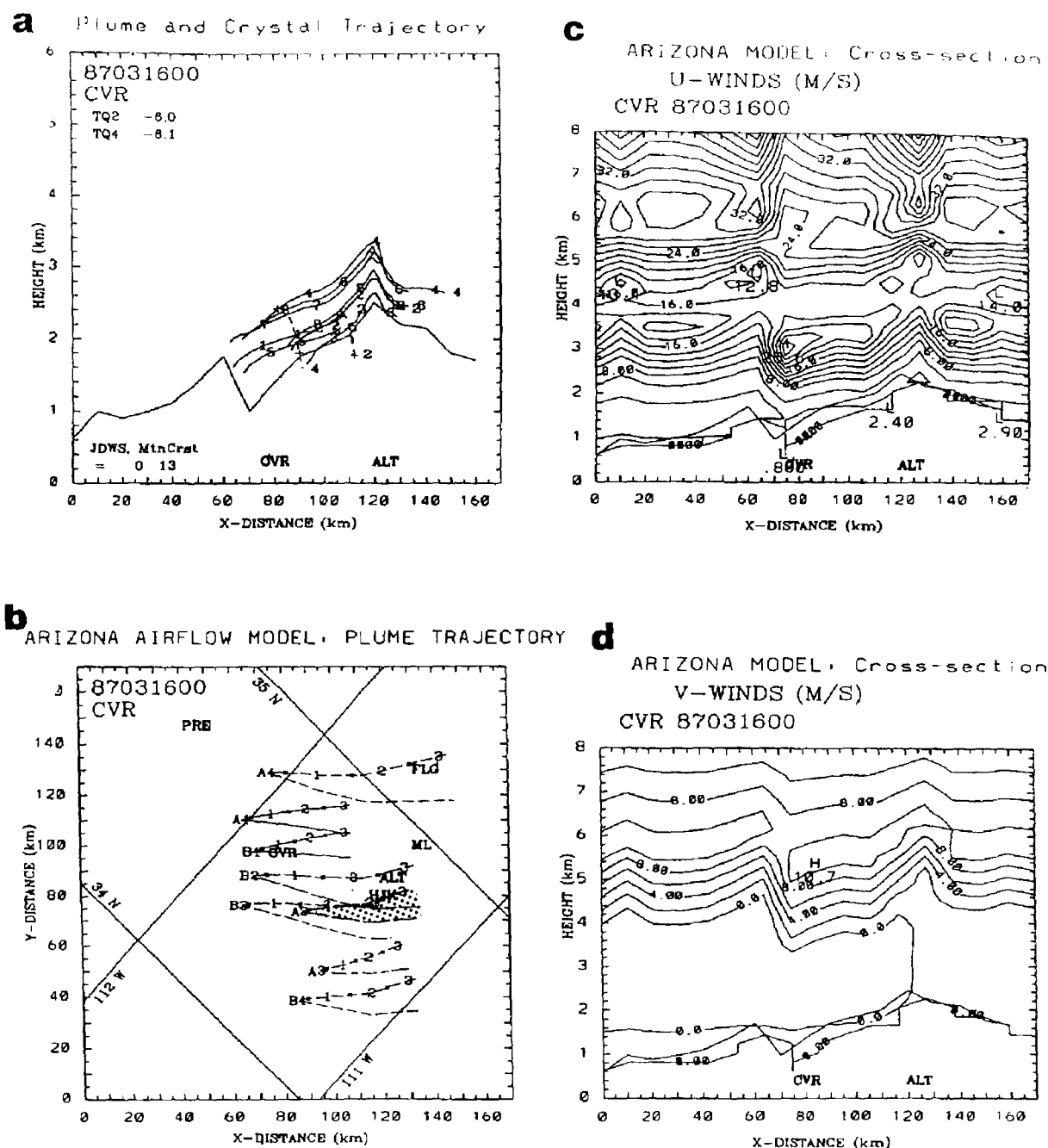
Figure 2.16. – Plume predicted from the CVR sounding at 0000 UTC, March 16, 1987. Numbers along the plume edge show the position of the plume every 30 minutes. Vertical cross sections show the $u$- (c) and $v$-components (d) of the wind (m s$^{-1}$).

identical columns, which upon impact with the ground, had $c$-axis dimensions of 980 and 979 μm and $a$-axes of 173 and 153 μm, respectively. Both crystals had terminal velocities of 1.09 m s$^{-1}$. Thus the increased $u$-component of the flow for the CMZ simulation carried the crystal farther than the CVR sounding. Slightly larger, nearly identical 1200-μm columns with terminal velocities of 1.21 m s$^{-1}$ developed in the A4 plume for the two soundings, but these crystals grew for 25 min in comparison to the 17 min available for the A2 crystals in both

34
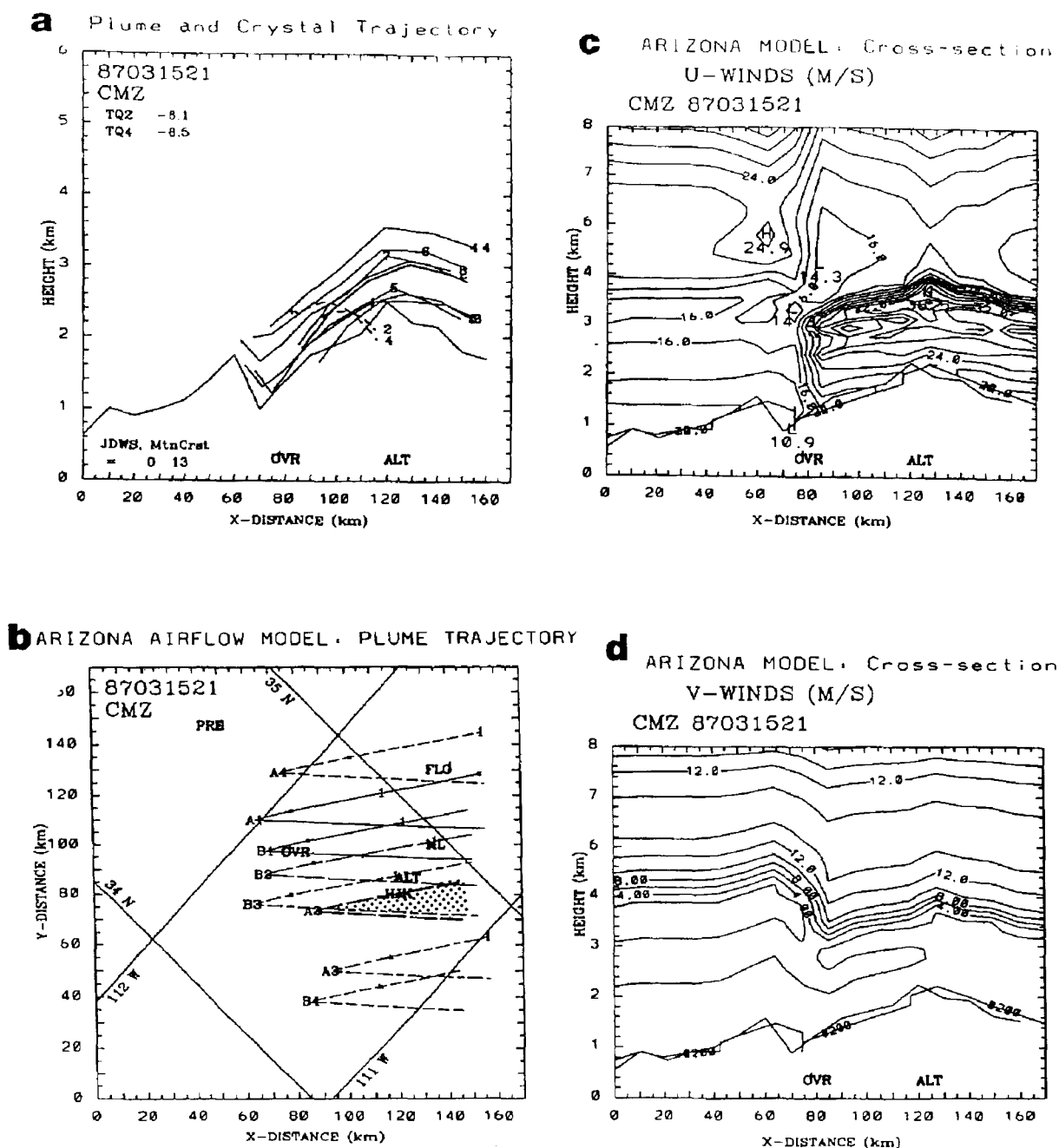
Figure 2.17. – Same as Figure 2.16 except the composite Clark model sounding at 2100 UTC, March 15, 1987, in post frontal conditions using stable flow channels.

simulations. In spite of the same 25-min growth times, the two A4 crystals fell out 20 km apart. The A4 generator site was more sensitive to flow accelerations than the A2 site because its higher elevation placed the nuclei in a different flow channel with higher winds. These examples show the AAIM model sensitivity to initial soundings and their effect on ice crystal targeting.
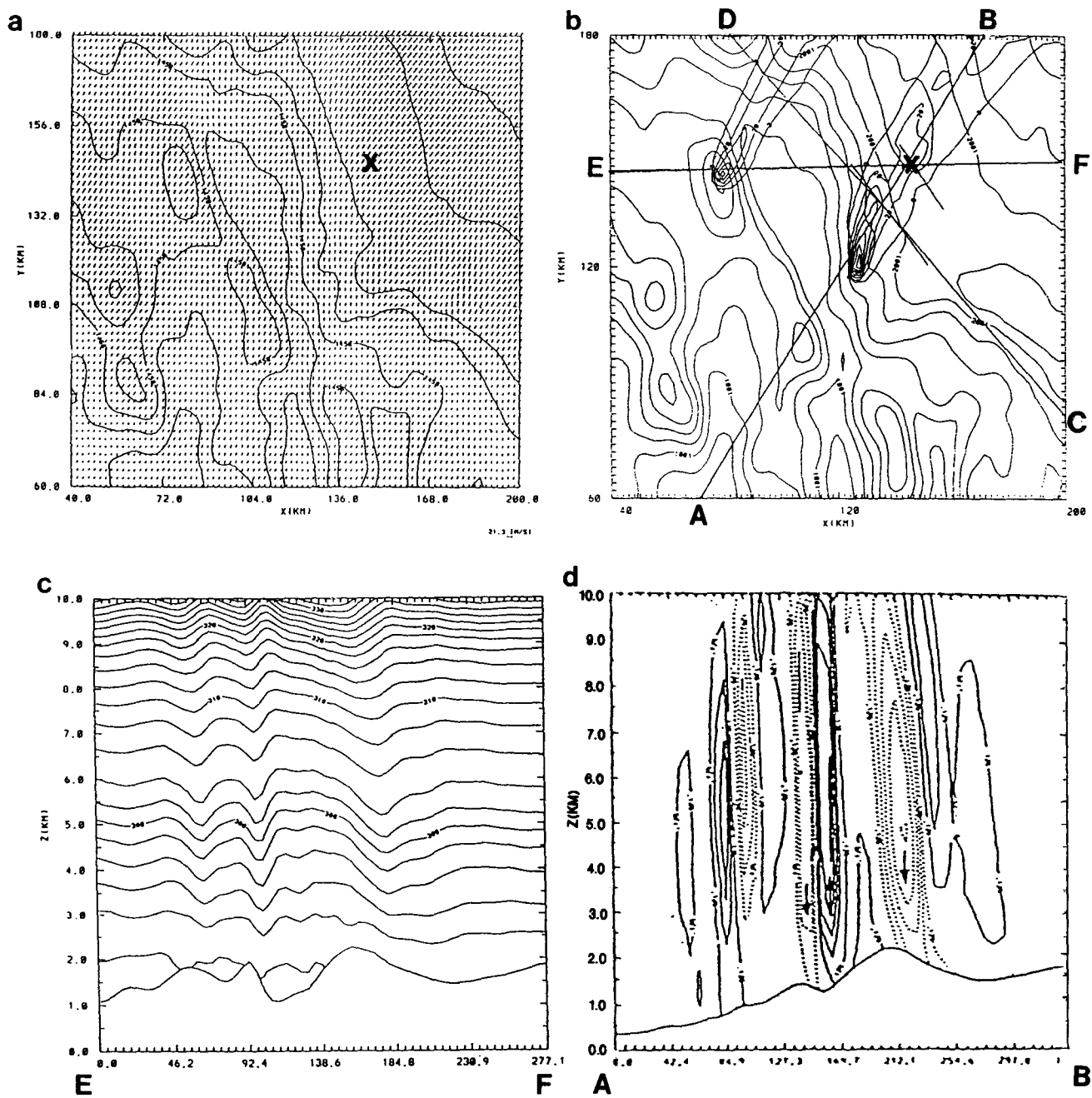
Figure 2.18. – Clark model results for the CMZ composite sounding at 2100 UTC March 15, 1987. Details are the same as described in Figure 2.14. Happy Jack is at the X (from Bruintjes et al. 1991).

Clark model simulations predicted a plume that passed over HJK and reached a top of 3 km m.s.l. (fig. 2.18). Airflow vectors in the surface layer are shown on figure 2.18a with corresponding plume concentrations at the surface (fig. 2.18b) shows the 20-km-wide plume over HJK. The vertical motion field here had a distinct standing wave pattern with a region of maximum lifting 30 km upwind of the crest at 5-7 km m.s.l. shown on figure 2.18d. This pattern corresponded to a distinctly different flow channel structure from the February 3 and 15, 1987, cases. The flow field produced a potential temperature field that reflects the wave pattern as shown on figure 2.18c. This pattern resembles the AAIM model flow channel structure. In this case both models predicted similar plume characteristics; however, the Clark model's time dependent solution provided more detailed information regarding the evolution and development of clouds and precipitation than the AAIM model. Such information is useful for research and development purposes, but may not be necessary for field operations.

**2.2.2.4 *March 2, 1987: Forest Road.*** – Very light winds prevailed on March 2, 1987. The model indicated a dead layer from the surface to 3.5 km with west-northwesterly flow of 2-10 m s$^{-1}$ above 3.5 km at CVR. Significant spatial variations were observed in the aircraft soundings. The plume moved slowly northwestward from the Forest Road SF$_6$ release point marked by A3 in model plots. The aircraft tracked it to the edge of the Rim about 12 km downwind, about one-third of the way to HJK. The aircraft sounding (PRZ) on climb out from Prescott at 1800 UTC indicated light 2 m s$^{-1}$ winds from 190° that were more representative than the CVR 1800 UTC sounding. The model simulation using the PRZ sounding produced short plumes from A2 and from Forest Road (A3) that did not reach HJK (fig. 2.19b-d). Observations indicated a rapid vertical rise of the plume characteristic of mesoscale orographic convective conditions. The AAIM model is not designed to simulate convective plumes. Its plume top heights reached only 2.4 to 2.6 km in contrast to the observed 3.1-km plume top height. Pilots observed local solar heating effects along the Rim. This heating likely accentuated the vertical fluxes beyond those typical of stable conditions that the model simulates well.

Model predictions from another Prescott-CVR composite sounding at 1800 also showed the plume passing slowly south of HJK and turning to the east 25 km downwind of A3 after 150 min of transport. Aircraft observations were not available to verify this plume location. However, this case demonstrates the model's limitations in convective conditions with light and variable winds.

**2.2.2.5 *March 5, 1987: Payson.*** – This case produced the best model simulation of observed conditions. Light southerly winds prevailed below 2100 m. Above this level, wind speed increased to 10-20 m s$^{-1}$, which carried the plume directly over HJK from 2149 to 2322 UTC as shown on figure 2.20. Observed plume top heights of 2.8 km matched the model's analysis. Modeled plume width reached 12 km at HJK, which matched that observed by aircraft. Note that Payson (B4, generator number 8) was 50 km directly upwind of the target in this southerly flow. The plume rose from the surface through the dead layer at 2200 m and then was carried with the wind to HJK. Observed aircraft winds upwind of the barrier were within 3 m s$^{-1}$ of model predicted winds at 2400- and 3000-m heights. At 4200 m the model tended to underpredict the upwind speed by 6 m s$^{-1}$. Simulations of stable conditions for the 1200, 1800, and 0000 UTC soundings indicated little change in wind speed and direction below 700 mb; but aloft wind speed increased. The plume top remained about the same for all soundings. The model predicted similar results for the CVR soundings at 1800, 0000, and 0600 UTC indicating a uniform structure of the plumes and vertical trajectories, that suggested a steady-state flow

**a** Plume and Crystal Trajectory
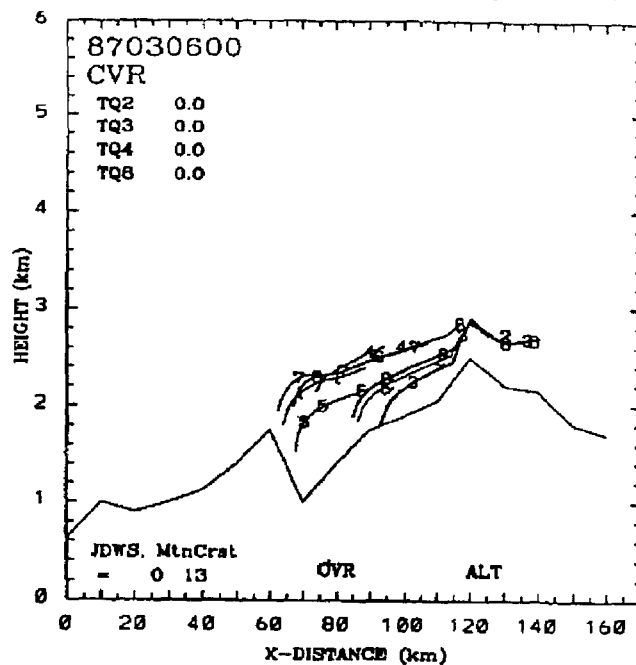


**b** ARIZONA AIRFLOW MODEL, PLUME TRAJECTORY
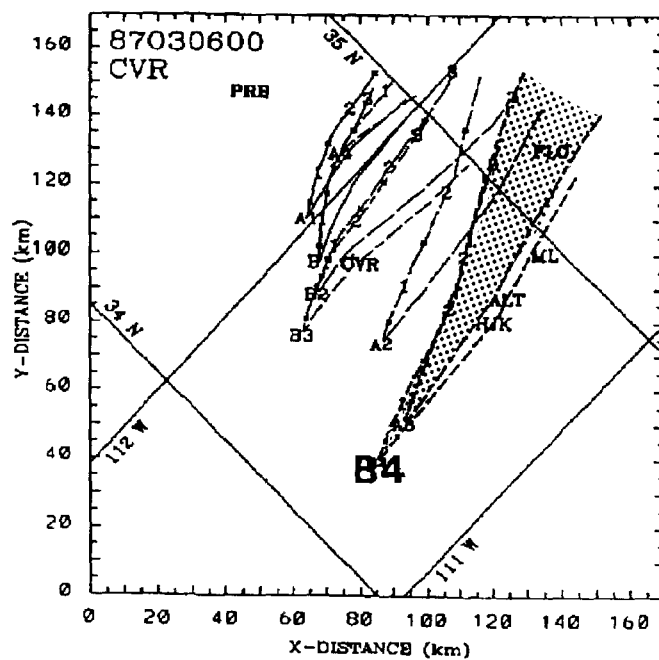


Figure 2.20. – Plume trajectories from the CVR soundings at 0000 (a,b) on March 6, 1987. SF₆ was released from Payson (B4).

created a dead layer of 3000 to 4600 m. Observed and modeled plume trajectories from Mingus Mountain (A4) passed 35 km west of HJK, missing it completely. HJK is 65 km southeast of A4, the aircraft followed the plume 40 km southeast of Mingus Mountain, but the plume did not reach HJK. At 0000 UTC on March 10, winds became more westerly resulting in a modeled plume that moved toward HJK, but ended 30 km northwest of HJK. This point was in close agreement with the aircraft observations of the plume 25 km northwest of HJK around 0000 UTC. Predicted plume top heights from the 1200 and 1900 UTC soundings reached only 2.7 to 2.8 km, well below the observed top of 3.5 km. Yet, the modeled plume reached 3.4 km under unstable-neutral conditions using the 0000 UTC sounding. Note that this sounding was the most representative of conditions during the flight from 2307 to 0236 UTC, further demonstrating model sensitivity to soundings and the need for frequent observations to capture the most representative initial conditions.

**2.2.3 Evaluation of Microphysical Characteristics.** – This section provides an assessment of the model predictions of microphysical characteristics and the resulting trajectories of ice crystals nucleated by seeding with ground and aircraft systems. The reader should recall that this model follows only one type of crystal and predicts trajectories from an initial set of levels or times depending on the seeding method. It simply describes the path of one crystal with no interaction with other particles. Therefore, the model cannot predict a series of different crystals that originate from different levels in a given simulation. The scientist operating the model has the flexibility to make different simulations that he feels best represent a variety of observed conditions. The observations described in this section were abstracted from the detailed descriptions by Super et al. (1989). Aircraft safety restrictions to flights in clouds near mountainous terrain precluded transport and diffusion studies in cases with microphysical observations. Therefore, the Clark model simulations of airflow will be helpful in evaluating the AAIM model.

**2.2.3.1 January 28, 1987.** – This case provided an example of a simple orographic cloud, which developed under strong southwesterly winds of 20-30 m s$^{-1}$ above 500 mb, which backed with height. This instance was the first cloud physics case of the 1987 field season, and was used to develop the original Clark model adaptations to the Arizona terrain reported by Hall et al. (1990). No precipitation was reported at the ground; still, supercooled liquid water persisted for several periods of 1 to 3 h and radar echo top heights were 6 to 9.5 km m.s.l. until 1700 UTC. Aircraft observations indicated regions of SLW in excess of 0.1 g m$^{-3}$ near cloud top at 5.1 km (-13 °C) with ice observed near cloud base in snow showers. Ice crystals were generally small (0.1 to 0.2 mm diameter), but occasionally 1-mm graupel and heavily rimed dendrites were observed. In this case Super et al. (1989) suggested that "seeding at higher levels would have produced larger particles, perhaps graupel-like pellets with high fall velocities."

AAIM model analyses of soundings confirmed the need for aircraft seeding. Only one seeding generator (A4) produced a plume that reached the -6 °C level and initiated crystal growth. This crystal grew to 1 mm and had a fall velocity of 1.1 m s$^{-1}$, which carried it to the ground 20 km on the lee of the crest after rising to 4.1 km m.s.l. (-6.3 °C). Wind data from the 1200 UTC CVR sounding were missing; therefore, the CVR 0000 UTC sounding was combined with the HJW 1600 UTC data in these simulations. Figure 2.21 shows the plume and crystal trajectory for the model simulation using the CVR January 29 0000 UTC and the HJW 1600 UTC soundings. This simulation resulted in deep vertical transport of the plumes as shown on figure 2.21a. The crystal growth in this simulation required 20 min from nucleation to reach 1-mm size at 3.6 km m.s.l. (-3.8 °C) and then 15 min to fall to ~2.2 km m.s.l. In all vertical cross sections, the crystals
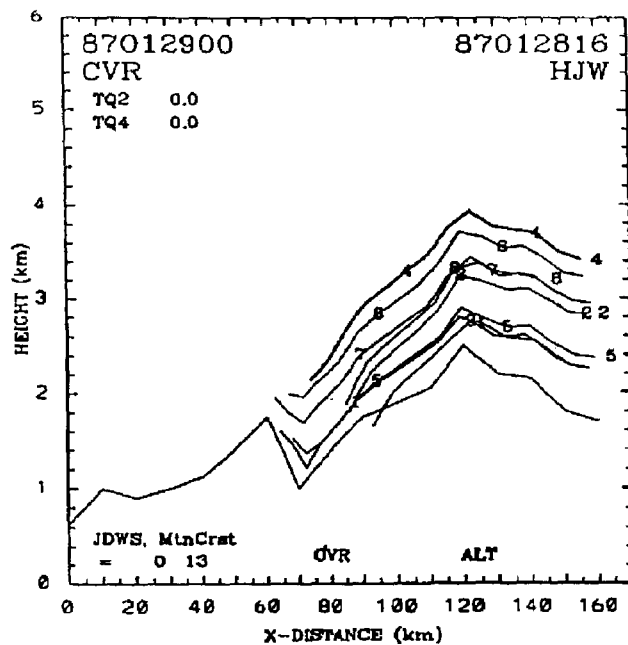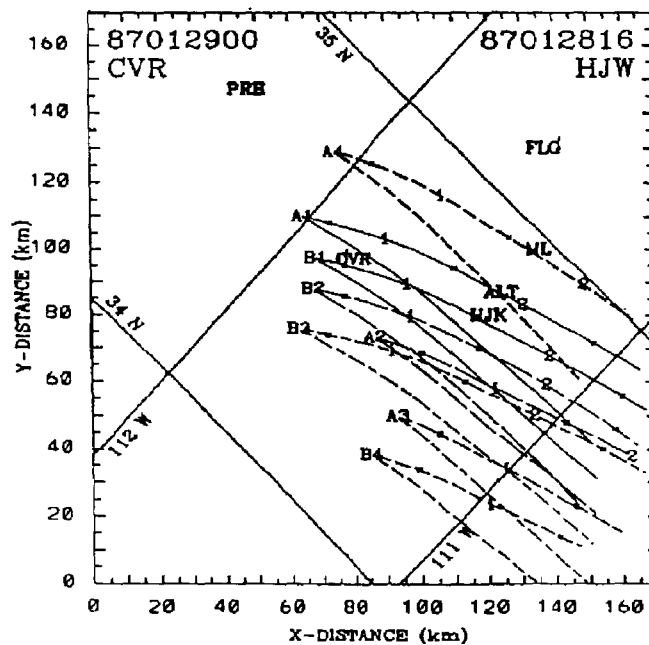
Figure 2.21. – Plume and crystal trajectory for the model simulation using the CVR 0000 UTC and the HJW 1600 UTC soundings, January 28-29, 1987.

from generators **A2** and **A4** are marked by numbers **2** and **4**, respectively. The nucleation temperature of -6 °C for the A4 plume was at 4.3 km m.s.l. Strong westerly winds of 15 to 20 m s$^{-1}$ at 3.5 to 4.2 km m.s.l. produced 0.3 to 0.6 m s$^{-1}$ lifting ahead of the crest. Lifting increased to 1.1 m s$^{-1}$ at 6.5 km m.s.l. above the crest at HJK, where the model $u$-component of the wind reached 29 m s$^{-1}$, which closely matched the aircraft wind observations of 27 m s$^{-1}$ at cloud top and vertical motion of 1 m s$^{-1}$. Plume positions every hour are shown by the numbers marked on the north edge of the plume (see fig. 2.21b).

Simulations of three-dimensional airflow and cloud development in the Clark model showed a distinct orographic wave with strong 3 m s$^{-1}$ lifting at the base of the ridge in the cloud ahead of the crest and sinking over the crest and lee side that reached 1.5 m s$^{-1}$ in contrast to 1 m s$^{-1}$ observed by aircraft and predicted by the AAIM model (see Hall et al., 1990, for details). Figure 2.22 shows the horizontal cloud distribution and cloud ice distribution in the airflow across the barrier along three north-south cross sections (lines AB, CD, and EF) at 80, 160, and 240 km east of the origin respectively. HJK is 150 km north and 150 km east of the origin (marked **x**). The Clark model results added credibility to the AAIM model's diagnosis of a seedline 80 km upwind of the target; however, the vertical motion field in the AAIM model was weaker than that in the Clark model simulations.

AAIM model simulations of aircraft seeding at the -14°C level using droppable flares from 5486 and 6096 m (18,000 and 20,000 ft) m.s.l. produced similar millimeter-size rimed plate crystals and fallout patterns. The strong winds required a seedline 80 km upwind of the target at a point 25 km northwest of Mingus Mountain (A4). Crystal growth and fallout for the aircraft seeding example required 75 min and occurred 80 km downwind of the **Q-point** shown by the stippled area on figure 2.23. Aircraft observations showed that the upwind edge of the cloud system matched the cloud outline in the Clark model simulation where a cloud extended 80 km northwest of HJK along the Rim (fig. 2.22a). This model's three-dimensional terrain retained the northwestward orientation of the Rim, the Verde River Valley, and the Mingus Mountain ridge west of the Rim, by realistically simulating lifting and resulting clouds. These model results suggest that aircraft seeding at the -14 °C level using droppable flares might have been a realistic seeding scenario for operations on this day. Further study of this scenario in the Clark model simulations is needed to evaluate this approach.

This aircraft simulation shows the type of information that the AAIM model provides operations directors and aircraft pilots regarding the positioning of seeding and cloud physics aircraft. The model showed a seeding line 20 n mi long located 80 km northwest of HJK with a right end 12.1 n mi from the Prescott VOR along a heading of 083°. The corresponding left end of the seeding line was located 21.7 n mi from the VOR on a heading of 017°. Figure 2.23 shows the seedline marked by the bold **Q** at its centerpoint. This seedline **Q-point** was on a 039° magnetic heading 14.4 n mi from the VOR. The initial cloud physics aircraft position was at 5796 m (19,000 ft) m.s.l. The model tabulation of this information is found in the "Airflout.dat" data file for the aircraft seeding simulation described in Appendix A1, section 3.2. This table transforms information from model coordinates to positions using terms that the pilot can readily interpret to navigate his aircraft to the appropriate location for efficient seeding or cloud physics data collection. The VOR is about 7 km northwest of the Prescott Airport. This VOR provides navigation information for the pilots flying over this portion of the Mogollon Rim. In this test the seeder aircraft height was selected at 6096 m (20,000 ft) m.s.l. and the resulting research aircraft altitude 300 m below at 5796 m m.s.l. The seeding line end points and the
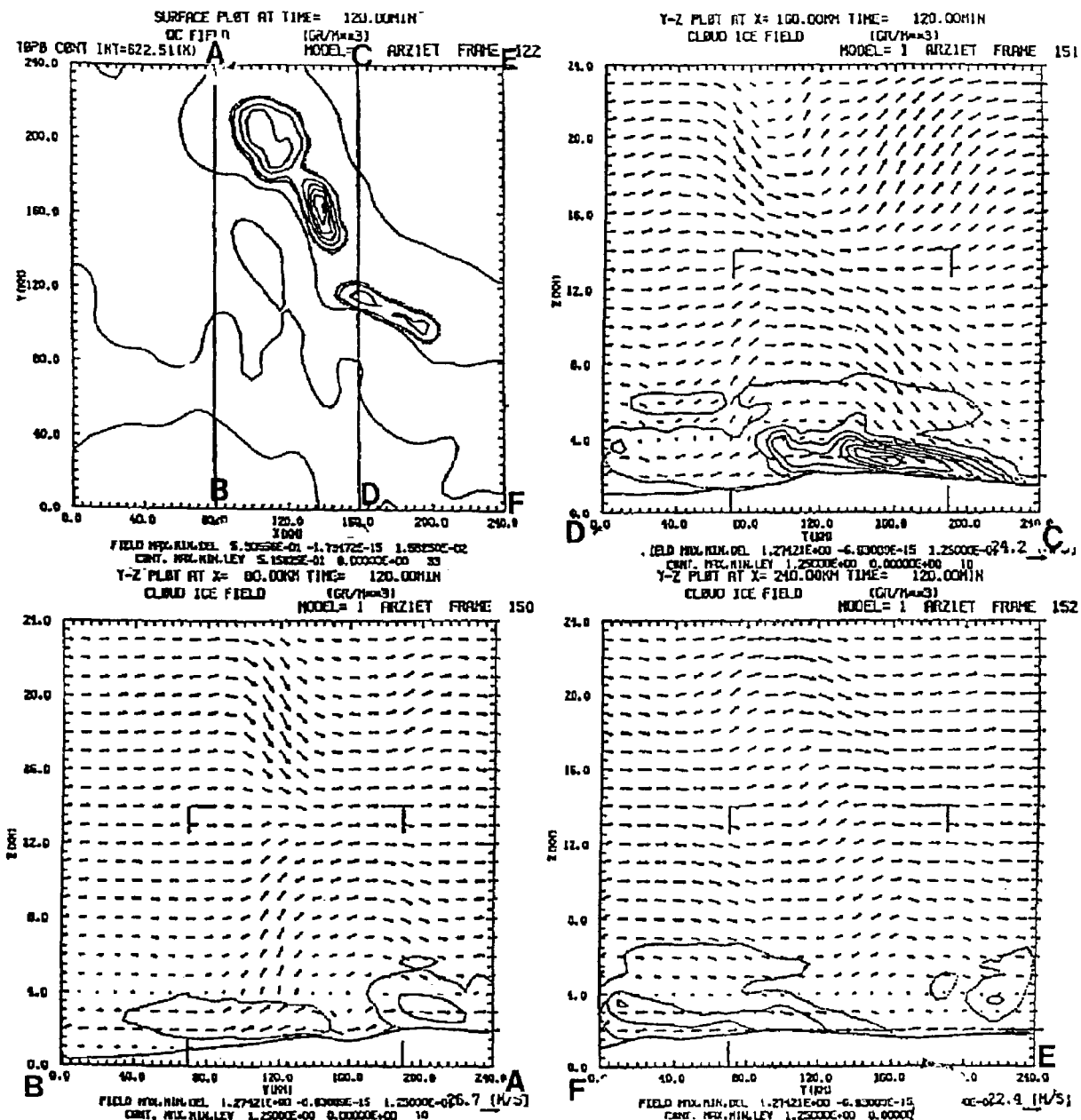
Figure 2.22. – Horizontal cloud distribution (a) and vertical cloud ice cross sections from Clark model simulations showing airflow across the barrier in different north-south cross sections along lines **AB**, **CD**, and **EF** at 80 (**b**), 160( **c**) and 240 (**d**) km east of the origin respectively. Happy Jack is 150 km north and 150 km east of the origin.

location of the aircraft Q-point were computed. Model tabulations also indicate the particle type, fall time and size of the a- and c-axes, and degree of riming and shear vector.

**2.2.3.2 January 30-31, 1987.** – This case provided a test of the model under changing storm conditions as a trough of low pressure moved from southern California through central Arizona, producing periods of heavy precipitation on the Mogollon Rim on January 30-31, 1987. This storm produced 24 h of nearly continuous SLW over HJK beginning at 2200 UTC January 30. The radiometer observed CLW that ranged from 0.2 to peak values of 0.7 mm of integrated

43
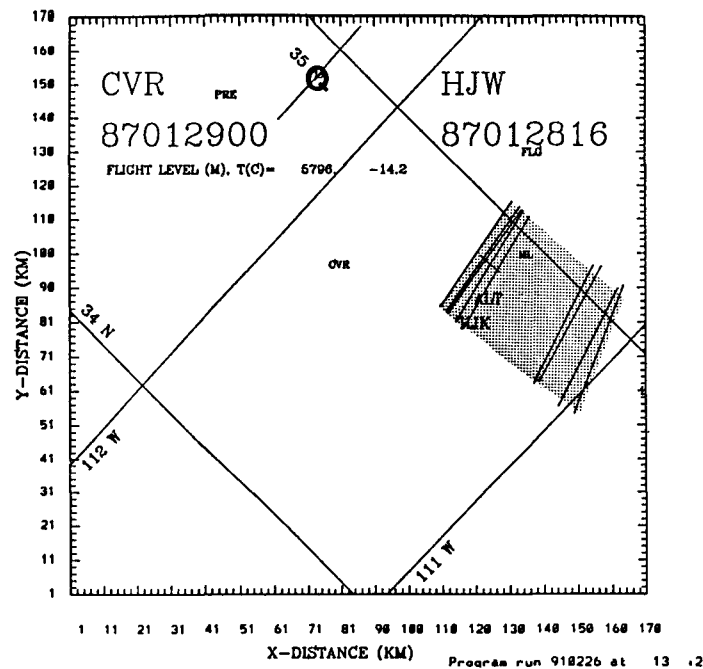
Figure 2.23. – Aircraft seeding seedline q-point (Q) and crystal fallout zone. Lines indicate the area of crystal fallout from five different release times.

water. Two aircraft flights observed convective clouds with mesoscale bands and thunderstorms during the flights. The first flight on January 31, from 0015 to 0330 UTC, observed rapidly changing conditions in the early part of the storm. SLW was spotty ranging from 0.05 to 0.15 g m$^{-3}$. Many ice crystals were encountered with dendritic forms common, and aggregates of dendrites often reached several millimeters in size. Graupel-like particles were predominant in the wetter portions of the cloud at 4.29 km m.s.l. to the north of HJK. Precipitation was light during the early part of the storm even though CLW was abundant during the frontal passage. This light precipitation suggested that the system was inefficient in converting liquid water to precipitation during this period.

Table 2.7. – Aircraft seeding sensitivity analysis on January 31, 1987.

| Experiment Fallout Identification (fig. 2.24) | Seeding Method | Stability | Flight level (ft m.s.l.) and Nucleation T (°C) | Crystal length (μm) | Type | Max $V_t$ (m s$^{-1}$) | Growth time (min) | Fallout point (km) |
|---|---|---|---|---|---|---|---|---|
| a | CO$_2$ curtain | U | 16000-9.4 | 1383 | rP | 1.3 | 57 | 65 |
| b | AgI flares | U | 20000-18.5 | 2887 | rD | 0.88 | 93 | 100 |
|   | AgI wingtip | U | 16000-12.5* | 614 | rC | 0.84 | 65 | 108 |
| c | CO$_2$ curtain | S | 16000-9.4 | 889 | rC | 1.03 | 44 | 85 |
| d | AgI flares | S | 20000-18.5 | 1807 | rD | 0.75 | 77 | 99 |

* The temperature at the nucleation level is at the flight level for wing tip flares, however, CO$_2$ and Pyrotechnic flare nucleation temperatures are reported for a level 300 m below the aircraft flight level.

Heavy snowfall of 3 to 5 mm h$^{-1}$ occurred from 1000 to 1300 UTC January 31. The second flight found heavy icing over HJK in regions of SLW that averaged 0.5 g m$^{-3}$ and peaked at 0.7 g m$^{-3}$.

44

Most ice crystals were needles and columns with occasional graupel-like particles with ~0.5-mm diameters at the lowest permissible flight level, ~3.0 km m.s.l. Cloud top height dropped to 3.85 km at 1655 UTC over HJK. Three decent/ascent passes over HJK from 1718-1757 UTC detected a region of column and needle growth, possibly by the Hallett-Mossop mechanism in the -5 °C temperature levels near 3 km m.s.l. Markedly higher IPC was encountered below 3.0 km over HJK with SLW values ranging from 0.08 to 0.13 g m$^{-3}$. But 20 to 26 km north of HJK, the highest values of SLW (0.6 to 0.7 g m$^{-3}$) were observed at 2.97 km indicating large spatial variations and suggesting a local low-level orographically induced SLW production zone. This case will be interesting for three-dimensional Clark model simulations by Bruintjes et al. (1993) who have generally found a SLW maximum to the north of HJK.

Soundings from CVR at 1200 UTC January 30 and 0000 UTC January 31 did not produce ice crystals from ground-based generators in the AAIM model simulations because of warm temperatures (10 to 17 °C) at the surface ahead of the front. Yet the AAIM model predicted a large 1-km increase in plume depth between 1200 and 0000 UTC soundings that showed the importance of the well mixed afternoon sounding and the effect of stronger flow at ridgetop. The modeled deep plumes passed to the west and north of HJK in the weak south-southeasterly flow to 3.6 km; however, above this level the wind increased to 20 to 30 m s$^{-1}$ from the south-southwest.

Aircraft seeding simulations using the 1200 UTC January 30, 1987, CVR sounding in this stronger flow showed that seeding with $CO_2$ and droppable AgI flare curtains from 4.877 km (16,000 ft at -12.5 °C) m.s.l. would produce rimed needles that grew to 1 mm and fell into the target after 81 min. Wingtip AgI-acetone seeding at the same altitude produced unrimed columns with 0.9-mm axis lengths that fell out after 62 min. These crystal types were the same as those observed by aircraft at 3.2-3.0 km m.s.l. (-7 °C), but the observed crystals were much smaller.

A sensitivity analysis of seeding techniques here clearly showed the importance of selecting the appropriate flight level and seeding technique to target crystal fallout along the Rim in measurement or watershed areas of interest. The 0000 UTC sounding from CVR on January 31, 1987, provided initial conditions for five simulations of seeding at temperature levels of -9, -12, and -18 °C. Here the distance from the seedline to the target ranged from 65 to 108 km depending on the type of crystals produced and the seeding altitude. Table 2.7 shows the results of this experiment.

Three types of seeding simulated in the model produced significantly different ice crystals and growth characteristics. Fallout points ranged from exactly on target for the unstable $CO_2$ curtain shown on figure 2.24a, to a complete overshoot of the target in the stable $CO_2$ seeding example (see fig. 2.24c). Targeting was set for the ALT-ML sites in these simulations. Note the significant differences in the maximum crystal terminal velocities that ranged from 0.75 m s$^{-1}$ for rD (rimed dendrites) to 1.3 m s$^{-1}$ for large rP (rimed plates) listed in table 2.7. Here the combination of different temperatures and winds at the effective seeding altitudes produced different crystal growth rates and resulting fall velocities, which determined the trajectory experienced by the particles. The heaviest, largest crystals with small cross sectional area, rimed plates, fell the fastest and were more precisely targeted on ML as shown on figure 2.24a. Large rD (rimed dendrites) grew to 2.9 mm, but their large cross-sectional area produced a smaller terminal velocity that spread the fallout footprint farther downwind, yet still permitted accurate targeting (fig. 2.24b). In contrast, the smaller lighter rC (rimed columns) fell
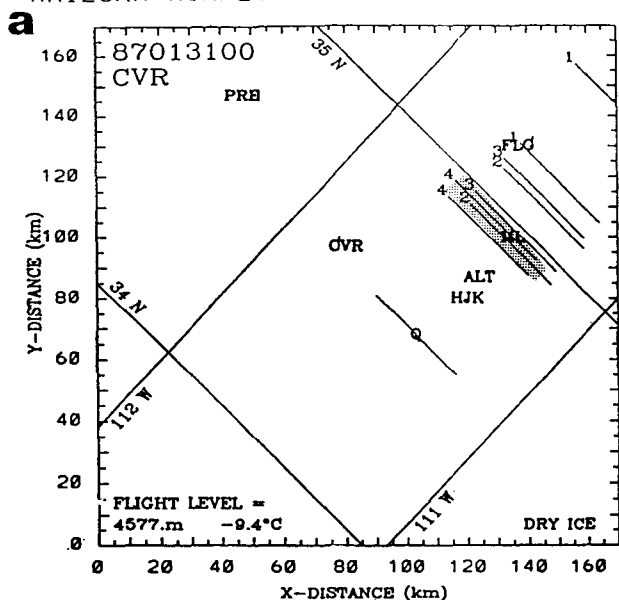
45
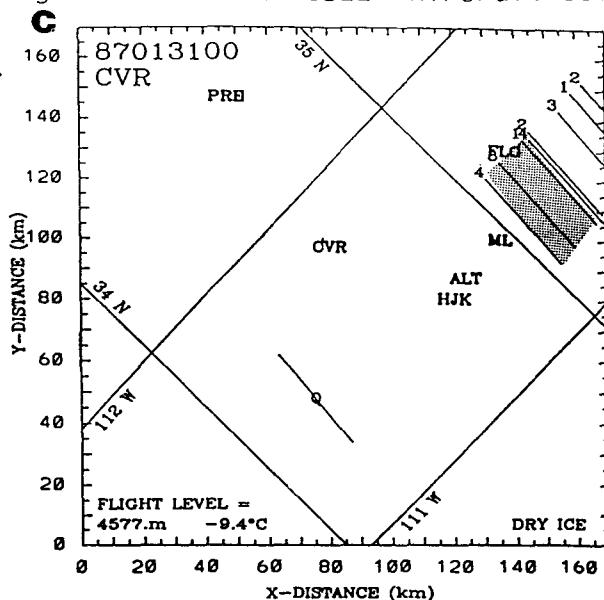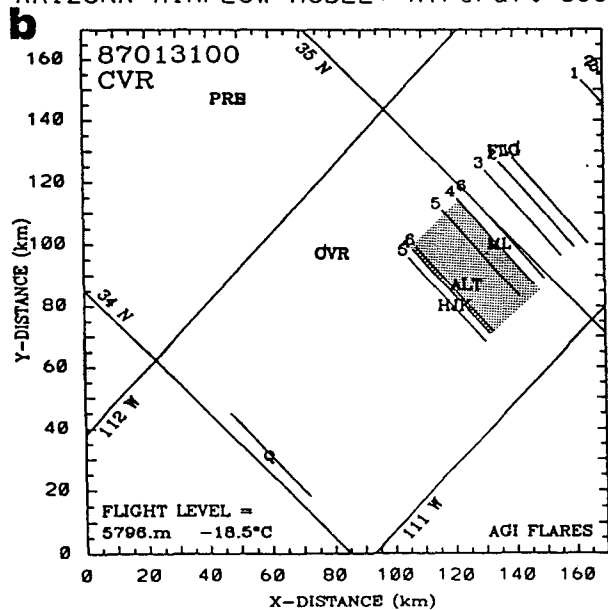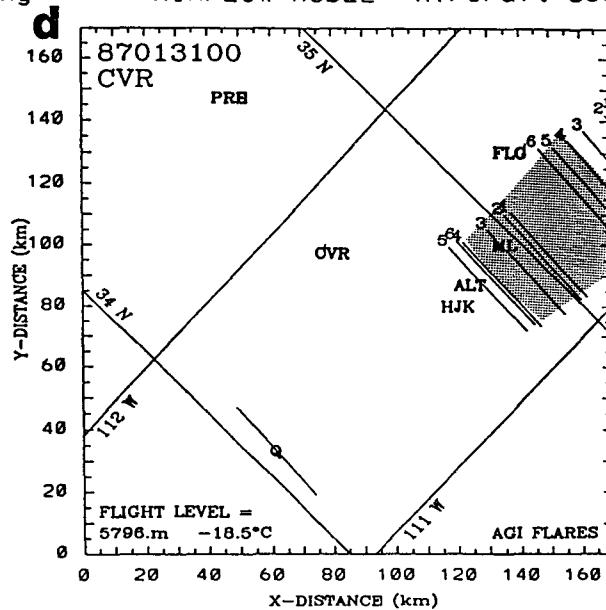
Figure 2.24. – Aircraft seedline and crystal fallout lines diagnosed by the AAIM model for the CVR 0000 UTC sounding, January 31, 1987. Four different seeding methods are tested for $CO_2$ curtain (a), AgI flares (b), for unstable conditions and $CO_2$ and AgI for stable conditions (c,d). Note the sensitivity of modeled fallout lines to seeding methods and stability criteria.

46

downwind of the target (fig. 2.24c). The model was unable to accurately target these crystals. Targeting of crystals was sensitive to the stability criteria, which is clearly shown by the comparisons of figures 2.24a and c, and figures 2.24b and d. The stable flow channels accelerated the crystals past the target, resulting in an increased overshooting of the target.

The sensitivity analysis for this case shows how the model may be used to determine the best seeding procedures on a particular day and illustrates the importance of selecting the most effective seeding altitude and method. In this case the user would select a lower seeding altitude to improve the targeting by wing tip acetone seeding generators, if dry ice or droppable AgI flares were not options. The specific strategy for seeding depends on local conditions such as cloud location, its depth and liquid water content, temperature at flight levels, wind component normal to the target, stability, and air traffic control restrictions. Therefore, the field scientist and project director must make the appropriate decisions for actual aircraft operations, the model simply serves as an objective tool for his decisionmaking process. All numerical models are subject to the limitations of their physical and numerical design and initial conditions. Each model provides an objective framework to evaluate the existing conditions and help the flight scientist and operations director in their decisionmaking process. However, to the extent that the model's results are consistent with observations and the scientist's sense of conditions at a given time, the model will provide useful information. A model cannot be used as a final definitive decision maker given today's technology; yet, it may provide valuable assistance.

**2.2.3.3. February 24-26, 1987.** – This case illustrates model performance in a well-documented, complex snowstorm. During this period, heavy snowfall grounded aircraft operations and limited data collection to automated surface observations from radar, radiometer and weather stations. This storm had well defined mesoscale convective bands, strong orographic lifting, and periods of efficient natural precipitation between inefficient periods of high SLW production. The storm had the highest CLW production of $41.9 \times 10^7$ g/m of crosswind distance, lasting 80 h with precipitation during 69 percent of this period. This case produced the equivalent of 35 percent of the 1987 field season's total water flux. It is interesting because it shows the evolution of airflow during an intense precipitation event and shows the model sensitivity to mesoscale changes observed by soundings made at 6-h intervals during this storm. Nearly saturated conditions prevailed from the surface to 500 mb (18,000 ft m.s.l.) throughout this storm. A series of nine soundings from CVR provided excellent information on the temporal evolution of the storm. Surface temperatures at CVR were near 0 °C throughout the storm with -6 °C nucleation levels for all generators between 1803- to 2343-m (5900- to 7700-ft) m.s.l. altitudes. Only 6 of the 80 plumes simulated remained too warm for nucleation; 3 of these occurred in the warmer daytime periods after the storm.

All eight seeding generators simulated in this storm produced plumes that reached the nucleation temperatures (-6 °C) and resulted in needles or columns. Figure 2.25 shows plumes and ice crystal trajectories for two soundings that characterize this storm. Rapid nucleation occurred early in the plume rise producing crystals that grew and always fell out before reaching the crest. The interaction between orographically-induced sinking motion over the Verde Valley to the lee of the Mingus Mountain ridge, weak, low-level flow, and the evolution of different crystal growth rates led to the variety of crystal trajectories.

The first period of the storm, from 1530 to 0030 UTC on February 23, was convective with strong southwesterly winds above 700 mb ahead of the storm. This period was characterized by

Plume and Crystal Trajectory   Plume and Crystal Trajectory
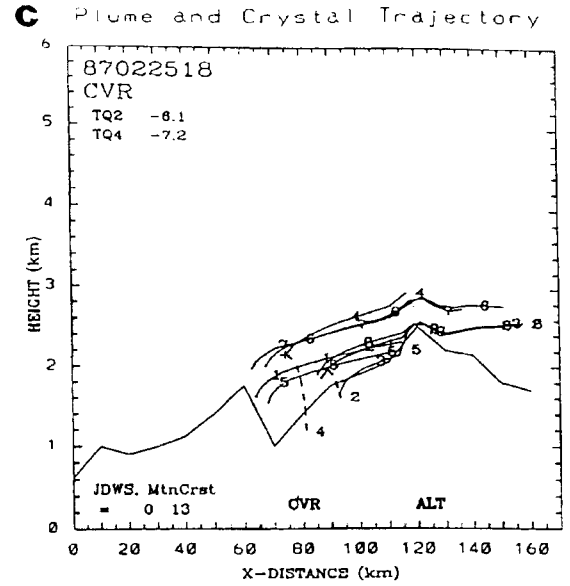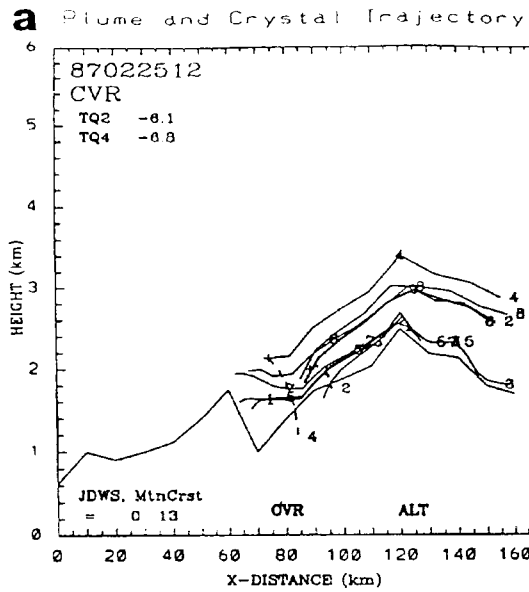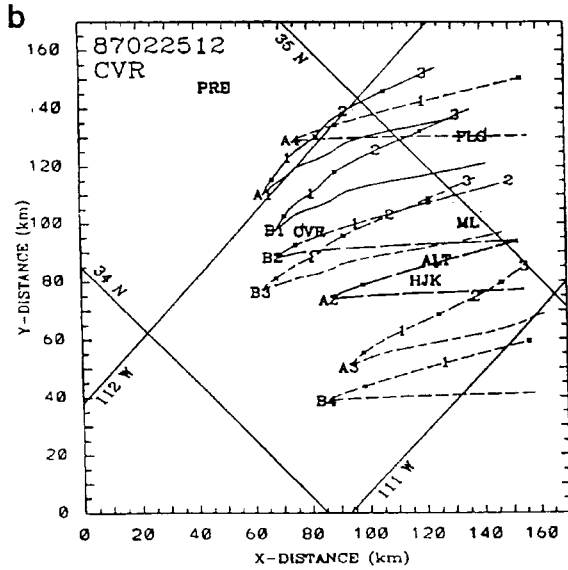
ARIZONA AIRFLOW MODEL. PLUME TRAJECTORY   ARIZONA AIRFLOW MODEL. PLUME TRAJECT
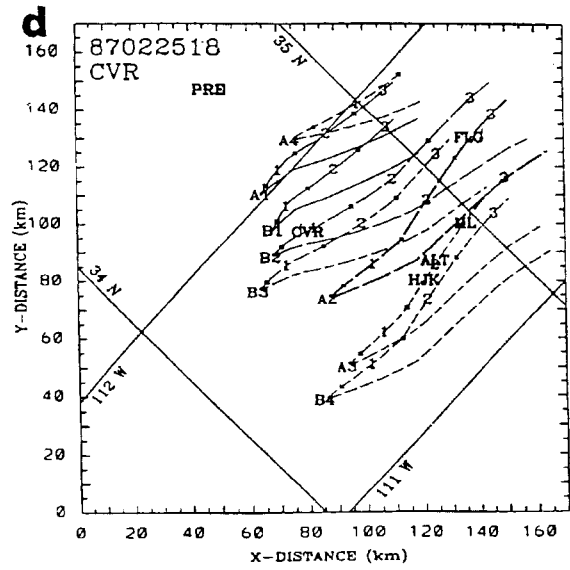
Figure 2.25. – Plume and ice crystal trajectories for the two CVR soundings observed on February 25, 1987, at 1200 (a,b) and 1800 UTC (c,d). Note the temporal variations in plume coverage and fallout points of ice crystals.

48

stratocumulus clouds with no snow and only moderate CLW observed by the radiometer. As convection increased from 0030 to 1200 UTC on February 24, 1987, precipitation became moderate to heavy, yet radiometer measurements of CLW still indicated moderate to large amounts of CLW. Super et al. (1987) suggested that this period could have been a good candidate for seeding. Then from 1200 to 0000 UTC February 24, heavy snowfall occurred, removing most but not all of the CLW. But radiometer observations suggest that the production of CLW was so large that the natural processes could not efficiently consume all of it. Therefore, potential may have existed for ground-based seeding. In the simulation using the February 24, 1987, 1900 UTC sounding, rapid growth of the crystals initiated by the A4 plume resulted in fall velocities of 1.3 m s$^{-1}$. These crystals fell on the upper slopes of the Verde Valley. They were carried farther up the barrier toward the crest than later in the storm. Here the crystals initiated from A2 and A4 fell to the ground at nearly the same point. Both crystals were millimeter size columns with terminal velocities of 1.2 and 1.3 m s$^{-1}$ respectively. Different $u$-components and vertical motions along each trajectory resulted in the same fallout point relative to the crest. The A4 fallout point was about 60 km north of that for A2. This case shows the complex nature of winter storms and suggests the need for three-dimensional analyses of the airflow and precipitation development. It would be an interesting case for further analysis by the Clark model using a four-dimensional data assimilation initialization to capture the storm's mesoscale structure.

Strong gravity-wave motion produced sinking of 3 m s$^{-1}$ over the Verde Valley in the AAIM model simulations using the 1200 and 1800 UTC CVR soundings on February 25. This sinking, combined with a crystal fall velocity of 0.4 m s$^{-1}$ in southwesterly winds of 5-7 m s$^{-1}$, produced a very short downward trajectory for A4 shown on figures 2.25a-c. In contrast the crystal from A2 had more time to grow, reaching a millimeter-size column with a fall velocity of 1.1 m s$^{-1}$. From 0720 UTC on February 25, to 1530, the largest amounts of CLW developed during the period of the highest winds as flow backed from southwest to south as shown on figures 2.25b,d. This flow was related to synoptic subsidence and clearing aloft that removed the upper-level clouds and allowed for more efficient CLW production. The model predicted significant seeded crystal growth and fallout on the lower elevations of the Rim during this period.

The selected generator sites appeared to provide coverage of the Rim throughout this storm until the cold frontal passage and return to westerly flow at 2300 UTC on February 26. These results support the concept of ground seeding of cold storms to increase precipitation in the Verde watershed. They show that at least 6-h interval soundings are often required to adequately describe mesosynoptic changes.

**2.2.3.4** *March 7, 1987.* – Convective conditions prevailed in a southerly flow as a moist pulse of unstable air passed over the region producing thunderstorms and graupel at HJK. Moderate amounts of CLW were observed by the radiometer during periods of graupel, wet snow and some rain. A tall cumulonimbus system moved over HJK from 1600 to 1800 UTC. Model simulations of this case did not produce ice crystals from ground seeding because the ground seeding plume minimum temperatures remained above -2 °C. Simulation of aircraft seeding at 4.267 km (14,000 ft) m.s.l. (-9.2 °C) using AgI flares produced a millimeter-sized unrimed column that grew for 46 min and fell out 24 km downwind of the seedline. This case shows the limitations of the model under conditions of deep convective activity. The model is not designed to simulate convective conditions and fails to develop deep convective plumes from the surface.

**2.2.4 Verification Summary.** – The previous two sections focused on specific case studies of model performance examining airflow and microphysical structure. This section provides a general overview of the model performance comparing 43 simulations of plumes predicted for 8 ground-based seeding generator sites. These simulations used sounding data from 6 days when $SF_6$ was tracked by aircraft. In addition, a series of 20 simulations was examined to verify modeled ice crystal development. In these simulations model plumes reached -6 °C temperature levels and produced ice crystals. Comparisons between modeled and aircraft observed winds and plume properties show the ability of the model to perform well under a variety of conditions without adjusting the observed soundings used to initialize the model. Model simulations were based on soundings observed generally within 6 h of the aircraft flights; however, several soundings were observed as much as 12 h before the flights.

**2.2.4.1 Modeled Wind Speed and Direction.** – Airflow is the most important variable in model simulations because it determines the trajectory of the seeding plume, crystal nucleation, and fallout locations. Two-dimensional models are limited in their ability to represent three-dimensional airflow over complex terrain. Therefore, it is gratifying that the results from the AAIM model have a remarkable resemblance to reality. Figure 2.26 shows comparisons of modeled airflow over the upwind area above the Verde Valley and the crest of the Mogollon Rim. Data from the model at grid points were compared with aircraft observations at three corresponding altitudes: 2.4, 3.0, and 4.2 km m.s.l. These altitudes represent the low-level flow across the barrier within flow channels affecting plume transport (2.4 and 3.0 km), and the mid-channel flow (4.2 km m.s.l.).

Modeled wind directions were generally within 30° of that observed both upwind and downwind of the crest shown by **bold lines** on figure 2.26a-b. Modeled wind speed upwind of the crest was generally within 3 m s^{-1} of that observed with a nearly uniform distribution above and below the observed speeds (fig. 2.26c-d). Over the crest, modeled winds increased because of the mass continuity requirements that were more restrictive in this two-dimensional model than in true three-dimensional flow. Observations also showed an increase in speed over the crest, but it was not as large as that modeled.

**2.2.4.2 Plume Trajectory and Depth.** – Comparisons between the analyses by Super et al. (1989) and model predictions of plume structure were encouraging. Five different $SF_6$ tracer release points were examined as discussed in section 2.2.2. Model predicted plume depth and width as defined at the 2-sigma level concentration line was compared with the observed plume's $SF_6$ concentration pattern as defined by the 3-p/t (parts per trillion) isoline at HJK. The modeled maximum plume top height was generally within 0.5 km of that observed and the plume width was within 3 km of the mean 7.6-km observed width as shown on figure 2.27. Table 2.6 compares the observed values with modeled estimates. The modeled plume width was within 1 km of the observed width at HJK in 15 of 24 simulations that used soundings observed during the six $SF_6$ tracer experiments. In the model simulation test, the mean observed plume width was 7.1 km in contrast to 7.8 km predicted by the model at HJK. In six simulations, the modeled plume top was within 200 m of that reported by the aircraft. This height was within the error of aircraft measurements. Only six cases were examined in the field study and those occurred on generally clear stable days that did not represent most storm conditions; therefore, it is difficult to generalize these results to actual storms. Analysis of the maximum plume depth correlated well with the observed depth when unrepresentative points were excluded. The distribution of dead layer top heights and temperatures shows that most stable layers were below 2 km m.s.l. and were relatively warm from 5 to 15 °C in this sample (see fig. 2.27).

**a** UPWIND: WIND DIRECTION
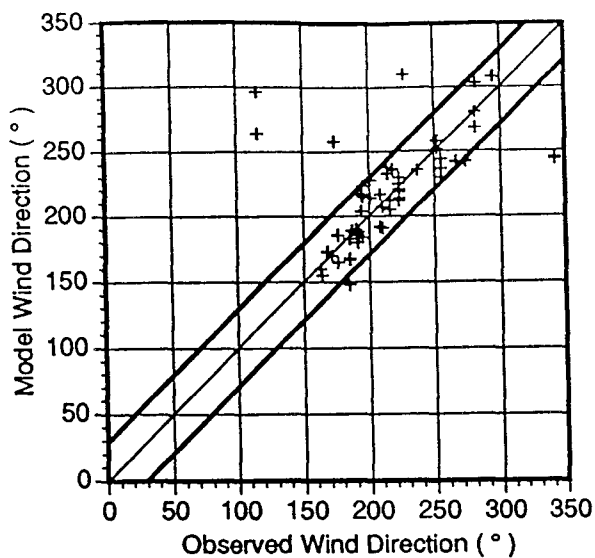
**b** CREST: WIND DIRECTION
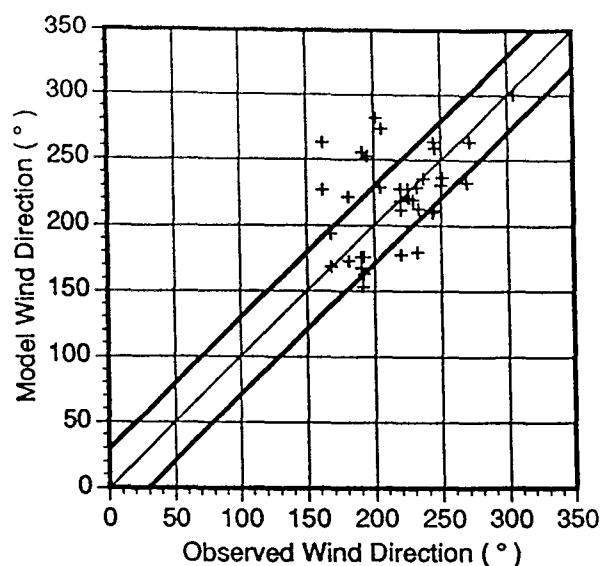
**c** UPWIND: WIND SPEED
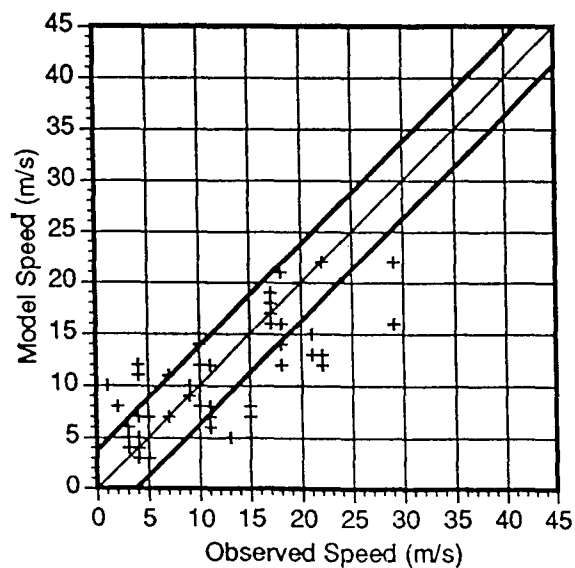
**d** CREST: WIND SPEED
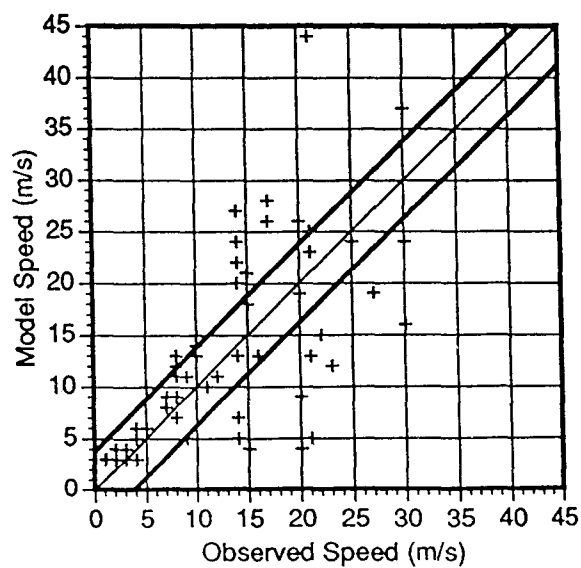
Figure 2.26. – Scatter plots of observed vs modeled wind direction (a,b) and wind speed (c,d) in the upwind area above the Verde Valley and above the crest of the Mogollon Rim. The **bold** lines indicate 30° direction differences and 3 m s^{-1} speed differences between the observed values and model estimates.

51

a  PLUME TOP HEIGHT

b  PLUME WIDTH



c  DEAD LAYER TOP HEIGHT

d  Temperature at Top of the Dead Layer
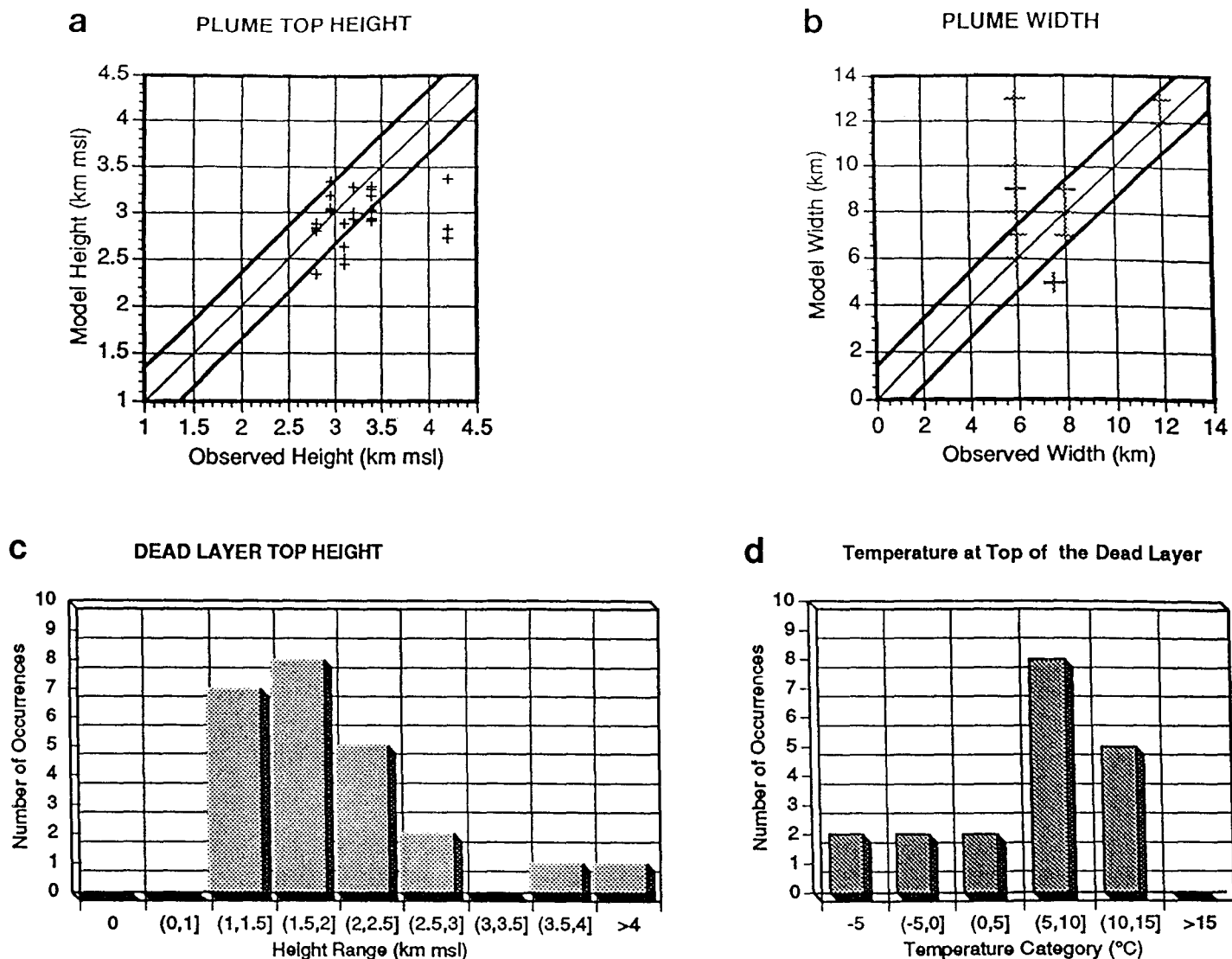
Figure 2.27. – Scatter plots of observed vs AAIM modeled plume top height (a) and width (b). The **bold** lines indicate ±300-m differences between observed and modeled top heights and ±3-km differences in plume width. Frequency distributions of the dead layer top height (c) and temperature (d) show the large number of low-level, warm inversions in this 1987 data set.

The model predicted a range of maximum seeding plume top heights for eight generator sites in each simulation. Figure 2.28 shows results from 35 simulations that used soundings observed on 17 days from January 28 to March 16, 1987. The range of plume top heights represented effects of different elevations and locations of the test generator sites and the $SF_6$ release points. This envelope showed the potential for successful seeding by selected generators whose plumes reached nucleation temperature levels. Deeper plume penetration to colder temperature levels generally suggests better potential for seeding more storms than the shallow plumes. Sites with consistently shallow plumes were less likely to be useful generator sites. Figure 2.28a shows the maximum plume top heights for each generator in a time series plotted by JD (Julian Day). This sample represents 10 separate events, 5 of which had precipitation. The plots by JD have over plots of results from several soundings on the same day. Thus, these plots indicate the daily range of results. This time series shows the temporal distribution and duration of each storm event examined from January through March.

**a**

MAXIMUM PLUME TOP HEIGHT

Generator Sites

| 1 | A1 |
| 2 | A2 |
| 3 | A3 |
| 4 | A4 |
| 5 | B1 |
| 6 | B2 |
| 7 | B3 |
| 8 | B4 |

Maximum Plume Height (km msl)

Jan.  February  March

Julian Day 1987

**b**

MINIMUM PLUME TEMPERATURE

Temperature (°C)

Jan.  February  March
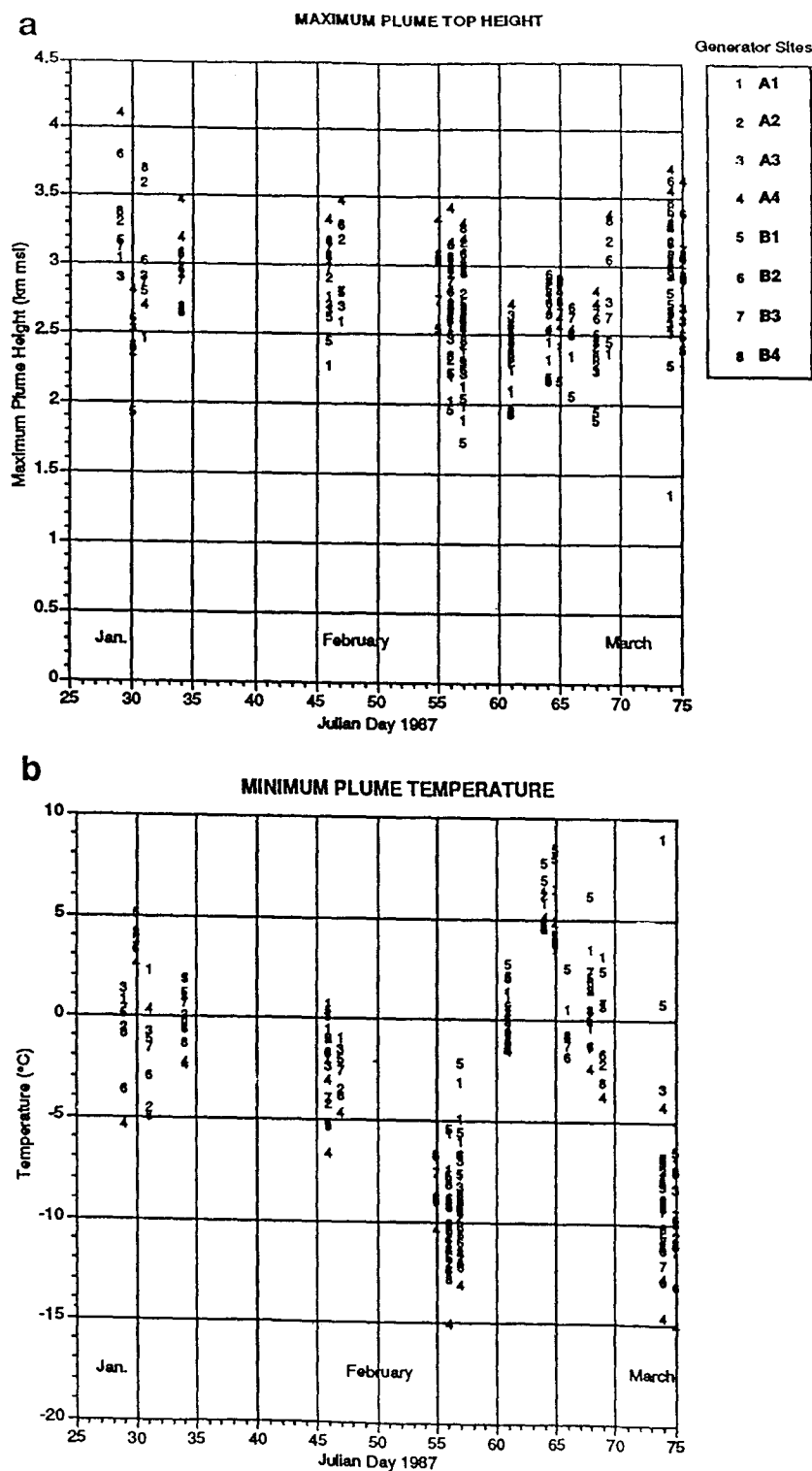
Julian Day 1987

Figure 2.28. — Time series distributions of maximum plume top height(a) and minimum plume temperature (b). Distributions by Julian Day show that nuclei from eight generators often reach heights separated by 0.5 to 1.0 km in a given case; however, all plume-top heights remained within 2 km of the ridge crest elevation. The coldest plume temperatures for all generator sites tested were often too warm to activate seeding nuclei.

53

Sites 1 and 5 (generators A1 and B1) consistently had the lowest plume top height, whereas 2, 4, 6, and 8 were consistently the highest. These patterns were reflected in the plume temperature analysis that clearly showed the limitations of ground-based seeding in Arizona. The limited sample of 17 JDs included only 5 precipitation events. Only one storm had an initial plume temperature of -6 °C on JD 55-57 (February 24-26, 1987). Only three other storms were cold enough for the minimum plume temperatures to reach -6 °C, as seen on figure 2.28b. On 11 of the 17 days studied all of the generators were too warm, while all the generators were effective on 5 days (JD 55,56,57,74,75). Thus, the model indicated that only about 30 percent of the days studied had potential for ground-based seeding. This limited sample of cases precludes generalizations for all Arizona storms; furthermore, the model's limited ability to simulate convective transport excludes evaluation of these cases, which are likely to be important precipitation systems in Arizona.

Model predictions of ice crystal characteristics were consistent with the indications from plumes examined in case studies. Seventeen model analyses of different soundings on 5 days when clouds and precipitation occurred showed that generators at A2, A4, B2, B3, and B4 developed the deepest plumes and produced the largest ice crystals. Generator sites A3 and B1 produced the crystals that fell along the Mogollon Rim most often. These crystals rose to higher maximum plume heights and were colder than those from other sites. These crystals also remained below freezing at their fallout point indicating somewhat colder conditions than the warmer transport and diffusion study cases.

Generators A2, A4, B2, and B4 produced the largest and most efficient precipitators, i.e. crystals with the highest terminal velocities. Nucleation started when the plume temperature reached -6 to -7 °C. This nucleation produced either needle or column crystal types whose terminal velocities ranged from 0.3 to 1.1 and 0.7 to 1.3 m s$^{-1}$ respectively over the range of sizes predicted in these cases. Sites A2, B2, and B4 produced the most large crystals in the 1000- to 1200-μm size range. Generator A3 produced the highest number of small crystals that were less than 500 μm. Interestingly, these smaller crystals overshot the crest most often; however, most generators produced crystals that fell out upwind and along the barrier crest.

**2.2.5 Model Capabilities and Limitations.** – The AAIM model produces plume trajectories and ice crystal fallout patterns that resemble observed conditions. The model simulates well the general properties of plume position and height downwind of tracer release points. It executes using operational sounding data with no modifications or adjustments to smooth observed initial conditions. The model assumes steady-state, non-transient atmospheric conditions and a simple uniform barrier in the y-direction normal to the 225° airflow. It is adapted to the Mogollon Rim of Arizona so that it may be used to position seeding aircraft and cloud physics aircraft flight tracks with respect to the Prescott VOR. These flight tracks and Q-points provide objective information that the operations director and pilots may use to guide experiments. The primary advantage of this model is its simplicity and robust character. It operates in real time on a microcomputer with limited requirements for resources. Model output is designed to provide information to solve practical operational questions under field conditions.

The AAIM model is limited by its assumptions of steady-state, two-dimensional, empirical solutions for atmospheric transport and simple ice crystal growth and fallout processes that often change rapidly in time and space. These processes are inherently three-dimensional, and often require complex non-linear numerical solutions to obtain detailed information. The greatest limitations are imposed by simplifying the complex three-dimensional terrain into an

$x$-$z$ plane and assuming a simple uniform ridge throughout the $y$-domain. This simplification limits the model's ability to simulate divergence and eddy motion induced by three-dimensional variations in the terrain that are important to the dynamic evolution of flow as demonstrated by the Clark model analyses described in sections 2.2.2 and 2.2.3. The three-dimensional, non-hydrostatic flow simulations clearly show horizontal and vertical variations in the wind fields that produce changes in the temperature and moisture fields, which evolve with time. The three-dimensional model also predicts the mesoscale structure of clouds and precipitation that varies in time and space, depending upon the airflow and thermodynamic conditions and topography.

The simple flow channel structure that was empirically derived from literature and field experiments produces a steady-state flow over the terrain that does not change from case to case. In reality, the structure of the flow channels changes with time and varies with the dynamic and thermodynamic conditions. Clark model simulations explicitly solve the primitive equations in terrain following sigma-coordinates. These solutions show spatial variations in the wave-like structure of the potential temperature fields within a simulation and between different cases. These variations produce different vertical motion fields resulting in significant changes in cloud and precipitation patterns over the Rim. Although these fields are tied to the terrain, their temporal and spatial patterns differ under various initial conditions. These flow fields also respond directly to buoyant forces that are not explicitly computed in the AAIM model.

The microphysical parameterizations in the AAIM model are limited to simple growth equations assuming saturated conditions throughout the crystal trajectory with no interaction with other particles or parcels of air in the crystal's environment. The model does not explicitly compute saturation at each point in the trajectory. This limitation may be a major constraint when nonhomogeneous conditions exist within a cloud or between cloud layers, which are often observed. Also, this simple approach neglects the effects of competition between particles for available water; therefore, it may overestimate the growth rates. However, a compensating error caused by lack of a pressure correction for the diffusivity of water vapor produces an underestimate of particle growth rate. Other limitations of the simple approach include dependence of fall velocity on density and Reynolds number, and the exclusion of aggregation and ice multiplication processes. Although aggregation may not be a problem in the Sierra Nevada (Martner 1986; Deshler and Reynolds 1987), Super et al. (1989) found indications that aggregation may be important in the more convective precipitation of Arizona.

The AAIM model was designed for somewhat stable orographic storms that may have neutral to slightly unstable conditions. The model does not explicitly simulate convective processes. Buoyant effects are not simulated; therefore, the model does not compute convective dynamics that may transport seeding nuclei into clouds and carry them within clouds to effective nucleation temperature levels. The empirically derived flow channels are fixed to the terrain and do not explicitly vary with different amounts of buoyancy. More explicit calculations are needed to improve this important aspect of the modeled airflow.

One limiting factor of complex three-dimensional, time-dependent models that solve the equations of motion and include time-dependent microphysics is their inherently high sensitivity to numerical instabilities. These instabilities are often introduced by mesoscale eddies and real phenomena observed in the unfiltered data. It may be difficult to alter such data in real time to produce stable numerical solutions of value to the operational decision

makers who need model results within minutes of sounding observations. To the extent that numerical instabilities do not affect the operation of the Clark model, it may become a much more powerful replacement for the AAIM model. Current research by Gall and Bruintjes and Clark and Hall will demonstrate the feasibility of the Clark model for operational simulations. Still, the simple, robust AAIM model will likely play a role in operations as a backup model and for onboard aircraft decision making. As more sophisticated models are developed and proven in the 1990s, this role may diminish.

## 2.3  Summary and Recommendations

The AAIM model has been adapted to the Mogollon Rim and performs well for operational applications. The model is a fast, objective, diagnostic tool that is useful for field program analyses during the daily decision making process. Model diagnoses of airflow and ice crystal trajectories appear to match observed airflow patterns and range of likely crystal trajectories. Modeled plume top height was generally within 200-500 m of that observed and plume width was within 3 km of the observed width. Plume positions downwind of $SF_6$ tracer release points generally matched the aircraft observed plume patterns and were within 2-5 km of the observed position at Happy Jack. But, results indicate that the model is sensitive to sounding variations that often occur within 3- to 6-h periods and within distances of 100 to 200 km. These variations produced significant changes in model predictions of plume and ice crystal trajectories, which suggest that rawinsondes are needed at 3- to 6-h intervals during field operations and should be taken at a site upwind of the barrier and along the Rim.

Case study results suggest that ground-based seeding may be effective in about 25 percent of the precipitation events. Two types of storms appear to have potential for ground seeding: cold mid-winter storms with surface freezing temperatures over the Mogollon Rim, and late winter, unstable convective systems with deeper vertical transport of seeding nuclei. Temperatures over the Rim are often too warm for ground-based seeding; therefore, airborne seeding will likely be required for most conditions. Model tests of airborne seeding suggest that the AAIM model will be a useful tool for positioning the seeding and cloud physics aircraft. The limited sample of cases studied in 1987 precluded broad generalizations regarding suitable seeding generator sites and aircraft flight tracks; still, they provided a useful model adaptation test.

Comparisons with coarse resolution simulations from the three-dimensional Clark model indicated that the AAIM model did not capture three-dimensional, time-dependent features of flow over the Mogollon Rim. More accurate and detailed results from the Clark model provide better theoretical information and guidance, but this model has not been proven as an economical operational real-time tool. Current studies by Gall and Bruintjes will evaluate the operational application of the Clark model. Results from their studies will determine the role of the AAIM model in future field projects. At this time the AAIM model is recommended as an operational tool for real-time decisionmaking.

Additional studies and field tests of the model are suggested to improve the model. These projects should involve comparisons with the high resolution Clark model research simulations and its coarse resolution operational version. During the initial field tests of the operational version of the Clark model, parallel runs with the AAIM model are recommended as a backup to provide timely information. A simple method to select the most appropriate flow channel structure for specific stability and wind conditions is needed to define more accurately the flow over barriers. A series of typical flow channels that are defined by the Clark model should be

developed to initialize the AAIM model under different conditions of stability and flow. These conditions should then be evaluated under a variety of conditions to verify model predictions.

Analyses of 5 days where precipitation occurred suggest that precipitation events are colder than the tracer study cases and that ground-based seeding may be suitable. More cases from different seasons must be examined to develop a climatology of seeding opportunities from which we may generalize frequency of ground-based seeding potential. In this limited 1987 sample, it appears that the storm structure evolves toward colder temperatures as cold advection behind cold fronts and within storms cools the atmosphere. These cold, unstable conditions favor ground-based seeding techniques. Super (1991) has found that unstable conditions in Utah permit transport of AgI from the valley floor into clouds along the Wasatch Plateau. Further study of this type of evolution is needed in Arizona. Further study of a larger sample of soundings such as those examined by Medina in section 3 of this report is needed to evaluate ground-based seeding feasibility.

The model should be tested onboard aircraft using a laptop computer to assist the flight scientist in real-time decisions during seeding experiments. Future field programs may use the simple model as an objective tool for quick assessments of conditions in flight, which may later be updated with more complete information from the three-dimensional models on the ground.

## 3. OROGRAPHIC PRECIPITATION MODEL

### 3.1 Introduction

The orographic precipitation process (fig. 1.2) has been observed in most mountainous areas of the world. Societal water needs and recognition of the simplicity of the most important aspects of this precipitation process have led scientists to develop mathematical models that simulate its occurrence over mountain barriers.

Some highly complex models are currently available that attempt to simulate intricate cloud processes in orographic clouds. These models generally require considerable computer resources and thus are used primarily for research purposes. Less complex models, known as orographic precipitation models, are also available. These models attempt to simulate only the most important physical processes that account for most of mountain winter precipitation. These simpler models generally require only routinely collected upper air sounding data as input. The simpler model, which is more amenable for production runs and application in the field, is the focus of this study.

An orographic precipitation model (hereafter denoted as a "precipitation model" or simply, "the model") employed with good success in Colorado (Rhea, 1978; Armstrong and Williams, 1981; Medina, 1981) is that developed by Rhea (1978) during the late 1970s. The model showed promise as a tool for daily operational use in the development of quantitative precipitation forecasts and in the development of a fully objective statistical covariate useful in the evaluation of cloud seeding effects on precipitation.

Arizona's future water resource needs suggested that a precipitation model adapted to the Mogollon Rim could add a useful tool for water resource studies. Rhea's model seemed well

suited for adaptation and application to the Mogollon Rim. Work on adaptation was initiated in 1990 and completed during early 1991.

Rhea's model, like other simple precipitation models, attempts to simulate only the most important physical processes that determine most mountain winter precipitation. Advantages of a simple model include ease of performing many iterative runs on relatively inexpensive microcomputers or work stations, and operational applicability of the model for hydrometeorological purposes. Additionally, the requirement of only routinely collected upper air sounding data as the primary input means that for many mountainous areas, availability of historical data enables the study of many winter storms.

Section 3.2 provides a brief description of the model and some of its important features, including inputs and outputs. Section 3.3 discusses adaptation of the model to the Mogollon Rim. Section 3.4 covers application of the model with historical soundings as input. The latter section includes the results of model runs for the study of winter storm climatology and comparisons with streamflow measurements. Section 3.5 provides a brief summary of the model adaptation and application results. Some figures and results are given in English units compatible with model requirements, operation, and output.

## 3.2 Model Description

Rhea describes his model in detail in his Ph.D. dissertation (1978). Interested parties should consult his publication for intricate technical details of the model. An abbreviated description of the most important features of the model is given here.

The two-dimensional, steady-state, and multilayer model accounts for moisture flow from any direction and terrain effects such as rate-of-rise and "shadowing" by upstream barriers. The model requires a topographic grid unique to each wind direction. Thus, 36 separate grid arrays of topography are employed, one for each 10° interval of the compass, at a selected grid spacing that for Arizona was set at 10 km. For each routine sounding period of the national sounding network, 0000 and 1200 UTC, the wind direction over a particular ground location and a selected pressure level is employed to determine the elevation grid array to be used for a model run.

An accounting of condensate formation or evaporation is maintained by the model as air layers experience vertical displacements in interaction with the underlying topography. Because the model is multilayer, condensate falling into a subsaturated layer will partially or totally evaporate. Eventually, condensate developed at higher layers reaches the ground as precipitation.

Simple formulations are included in the model to account for blocking at low layers. Under weak wind conditions and/or stable air near the upwind mountain surface, a blocked layer frequently develops over which the ambient flow must rise to move downstream. The model also estimates streamline vertical displacement as the air layers rise and fall over the undulating terrain. Enhanced streamline displacement over the highest terrain is used to simulate effects of convection, which is the only attempt in the model to simulate such effects.

The precipitation model can be configured to use inputs of vertical motion estimates that may lead to improved forecasts for some locations. When atmospheric sounding data are available

for three or more locations, the model can be configured to estimate divergence and thus compensate to some degree for the large-scale vertical motion. Forcing from this motion can lead to additional precipitation. The effect is to enhance the lifting of the moist layers and, consequently, the production of additional condensate. For some locations, estimates of the large-scale vertical motion may be obtained from sources such as the NGM (nested grid model) numerical model employed by the National Weather Service (and thus are not computed by the precipitation model).

The model employs a spatially constant precipitation efficiency. The particular relationship employed is given by,

$$E = -kT_c \, ,$$

where:

$E$ = efficiency
$k$ = a positive constant
$T_c$ = temperature in degrees Celsius of the highest layer with relative humidity equal to or greater than 65 percent (60% in Arizona) which is also not underlain by any lower layer with mean relative humidity less than 50 percent (45% in Arizona)

This formulation was found to give satisfactory results in simulations of Colorado storms provided $E$ was not allowed to exceed 25 percent or, of course, become negative when $T_c > 0$ °C.

Inputs to the model are given on figure 3.1. Soundings are required that contain estimates of the vertical profiles of wind, temperature, and humidity at the upwind edges of the geographical area of interest. The soundings are interpolated to 50-mb points up to 300 mb. The model also requires the coordinates of gauges or other point locations of interest, in the model
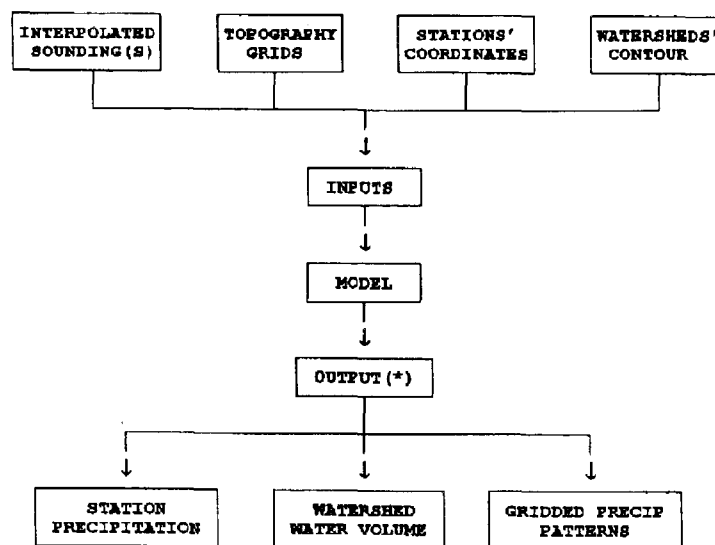


(*)The user specifies the time interval for outputs.

Figure 3.1. – Precipitation model inputs and outputs.

59

coordinate system, for estimation of precipitation at those sites. An interpolation scheme using surrounding grid point values is employed to produce desired point estimates.

An additional input to the model is the descriptions of watersheds of interest, coded according to the model coordinate system. Each watershed description consists of grid point coordinates for each point involved and respective point weights that represent the fractional area surrounding each grid point that is contained within the watershed. The model employs the watershed descriptions for integration of estimated precipitation over a selected time period. The resulting volume precipitation estimates can then be employed with streamflow measurements, in regression analysis, to objectively forecast monthly or seasonal streamflow (e.g., Medina, 1981).

Volume precipitation is an output of the model. Others, listed on figure 3.1, include estimates of precipitation for gauge and other specified locations usually not grid points (but could be), and estimates for each grid point of the model domain.

The model attacks the estimation of precipitation from a water budget point of view. Given in the following is the basic precipitation formula for the model (Rhea, 1978):

$$R = \frac{E}{\rho_w g} \int_o^t \int_{P_1}^{P_2} \frac{dq_s}{dz} \, w \, dp \, dt \tag{1}$$

where:

$R$ = Precipitation amount (cm)
$E$ = Precipitation efficiency (dimensionless)
$w$ = Vertical motion (cm s$^{-1}$)
$\rho_w$ = Density of water (1 g cm$^{-3}$)
$g$ = Gravitational acceleration (cm s$^{-2}$)

$\dfrac{dq_s}{dz}$ = Specific humidity chang with height (cm$^{-1}$)

$\displaystyle\int_{P_2}^{P_2}$ = Pressure depth of saturated air column (g cm$^{-1}$ s$^{-2}$)

$\displaystyle\int_t^o$ = Duration of the process(es)

Figure 3.2 shows a representation of the two-dimensional flow across a barrier as given by Rhea (1978). The schematic contains two streamlines, $N_1$ and $N_2$, many of which usually exist
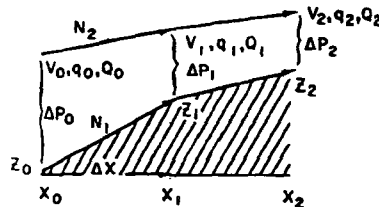


Figure 3.2. – Symbolic two-dimensional flow across a barrier (from Rhea, 1978).

60

in each model run. Definition of the variables on figure 3.2 are given below, following equation (2). These variables are employed in the computation of the precipitation rate.

The equation (Rhea, 1978) employed by the model for computation of a mean precipitation rate:

$$\bar{r}_{I,I+1}$$

between grid points $I$ and $I + 1$ that are separated by distance, $\Delta x$, is

$$(\bar{r}_{I,I+1})_l = \frac{EV_l\Delta P}{\rho_w g \Delta x}(Q_I + \Delta C_{I,I+1})_l \tag{2}$$

where:

| | |
|---|---|
| $l$ | = Computational layer in question |
| $V$ | = Horizontal wind speed in $x$ direction at grid upwind edge |
| $\Delta P$ | = Pressure thickness of the inflowing layer at upwind edge |
| $Q_I$ | = Cloud water mixing ratio of liquid or solid at point $I$ |
| $\Delta C_{I,I+1}$ | = Additional condensation (or evaporation) caused by vertical displacement between points $I$ and $I + 1$. |
| $E$ | = Precipitation efficiency |
| $\rho_w$ | = Density of water |
| $g$ | = Acceleration due to gravity |

The equation for precipitation rate is applied in a coordinate framework that follows the air parcels. The precipitation efficiency, $E$, is spatially constant and a linear function of the temperature of the highest cloudy layer expected to produce precipitation. Wind speeds are determined, level by level, as components in the direction determined for selection of the elevation grid applicable to the model run.

## 3.3 Model Adaptation to the Mogollon Rim

A previously indicated, the model requires access to 36 topographic grids. The grid spacing for Arizona was set at 10 km. Figure 3.3 shows a contoured presentation of the 10-km model topography that corresponds to a map orientation view of the terrain. This presentation illustrates the model domain and is frequently denoted as the "270° grid." Individual elevation values of the 270° grid were obtained by averaging archived 30-arc-second point values (elevations about every 0.8 km). Elevation values for each rotated profile, for example, the 300° profile, were obtained by overlaying the 270° profile with an appropriately oriented (grid lines oriented parallel to the 300° radial) 10-km grid and interpolating with inverse distance-squared weighing.

The model domain shown on figure 3.3 extends eastward into New Mexico and southward to, approximately, the Arizona/Mexico border. The northern border is located about 80 km north of Winslow and the western border is nearly 90 km west of Phoenix. The model domain extends 500 km in the north/south direction and 470 km in the east/west direction. Consequently, the 270° grid contains 51 rows and 48 columns.
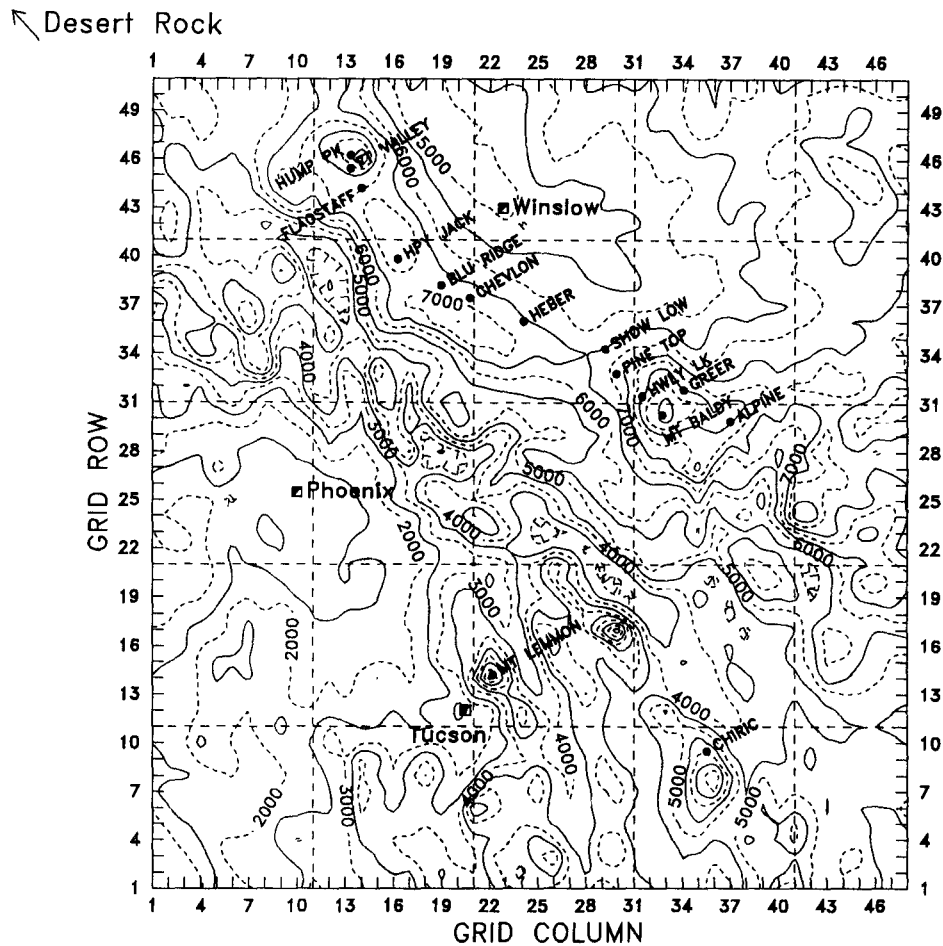
Figure 3.3. — Model topography for the Mogollon Rim area of Arizona using 10-km grid spacing (contours in ft because the model is mixed mode).

From an orographic precipitation production point of view, prominent protruding terrain substantially impacts the precipitation amount and deposition location. The Arizona study area is most distinguished by the Mogollon Rim, which is relatively flat compared to the Rocky Mountains, with the exception of two prominent peaks that extend above 3050 m (~ 10,000 ft). Slender peaks may be noticeably underemphasized in gridded terrain at a 10-km resolution. Study of figures 1.1 and 3.3 indicates that the model terrain erroneously has the elevation of the Humphreys Peak (San Francisco Mountain) vicinity less than that of Mount Baldy (White Mountains).

Figure 3.3 shows that several other prominent peaks are evident to the south of the Mogollon Rim including the Santa Catalina Mountains northeast of Tucson and farther southeast, the Chiricahua Mountains. The terrain in the southwestern part of the model domain is generally flatter and lower in elevation at 400 to 800 m (~ 1300 to 2600 ft) than terrain in the northeast. This elevation difference means that air layers moving from the southwest would be rising as they approach the Mogollon Rim. This lifting is responsible for condensation of air layer moisture and the formation of clouds and, eventually, precipitation.

The use of 5-km terrain resolution versus that at 10 km will improve simulation of precipitation in deep valleys surrounded by much higher terrain, but will likely overstate precipitation over the highest peaks (Rhea, 1978). Additionally, computer run time is approximately quadrupled

with the 5-km terrain. The questionable gain in precipitation accuracy for the Mogollon Rim, with 5-km terrain resolution, led to the selection of the 10-km resolution.

The model input requirement of sounding data was satisfied from the archives for the national network. Regularly scheduled daily 0000 and 1200 UTC soundings were obtained and interpolated for use by the model. The available sounding stations considered most applicable to the Mogollon Rim and possessing good quality data for a number of winters were DRA (Desert Rock), INW (Winslow), and TUS (Tucson). Soundings of each station were obtained for 10 winters of 1978-88. The winter term was selected as November through April.

For best results, the model should have representative sounding information at the upwind border of the model domain. Consequently, interpolation in space of the sounding data can noticeably affect the performance of the model. Rhea (1978) interpolated from available national network sounding data to 10 border positions, distributed around the perimeter of the model domain, plus the center of the domain. He selected border points such that they represented important moisture sources. Each grid line was then assigned to a particular border-point sounding. For the Arizona modeling, a similar procedure was applied, including the determination of 10 border soundings from the DRA, INW, and TUS data. A series of weights, based on inverse distance squared to real sounding locations, and assignments based on considerations of typical winter storm conditions, were employed to determine the border soundings. Assignment of each grid line to a border sounding was based on distance to border points and typical winter weather conditions.

For each model run, the selection of one of the 36 terrain grids is required. The average of Tucson and Winslow 700-mb wind directions was chosen to represent the flow over the Mogollon Rim during winter storms. This criterion was applied in all model runs.

The vertical displacement of the air layers as they cross the underlying terrain is estimated by the model according to airmass stability and terrain rise or fall. Model runs were made to study the sensitivity of, and determine appropriate values for, parameters affecting air-layer displacements. Model estimates of precipitation for selected sites on the Mogollon Rim were observed over a range of parameter values inserted into the model. The final parameter values selected were those that provided the better estimates of precipitation.

The large-scale vertical motion provides lift to air layers in addition to lift resulting from crossing over higher terrain. The model can estimate (a divergence computation) the large-scale vertical motion provided that at least three soundings are available for each observational time. Estimates were developed using the DRA, INW, and TUS soundings. However, estimation of precipitation deteriorated by inclusion of this feature. Consequently, it was eliminated in all production runs made with the model.

Model efficiency ($E$) was determined according to Rhea's procedure (1978). Attempts to improve model performance by altering his formulation were not productive.

The model uses thresholds for a number of other parameters such as the average relative humidity for key layers that indicate whether a sounding is "dry" or "wet" and, consequently, whether a complete model run should be performed. Analysis on the sensitivity of these parameters was performed to improve model performance.

For model fitting and verification studies, 13 gauges from the study area were selected that routinely report daily precipitation. Table 3.1 and figure 3.3 identify the gauges, their elevations, and locations (in the model coordinate system). The first 11 gauges listed in the table are positioned along the Mogollon Rim from north of Flagstaff to the White Mountains. The remaining gauges are located at Mt. Lemmon in the Catalina Mountains northeast of Tucson and the Chiricahua National Monument (hereafter Chiricahua NM) in the Chiricahua Mountains southeast of Tucson. Gauges preferred were those located at higher elevations and having historical records of adequate length and quality for comparison with model estimates.

Table 3.1. – Precipitation gauges employed in model adaptation and verification.

| Gauge name | Elevation (ft) | Location coordinates $(x, y)$ |
|---|---|---|
| 001 Fort Valley | 7347 | 13.30, 45.40 |
| 002 Flagstaff | 7006 | 14.00, 44.20 |
| 003 Happy Jack RS | 7480 | 16.25, 39.80 |
| 004 Blue Ridge RS | 6810 | 18.95, 38.20 |
| 005 Chevelon RS | 7006 | 20.75, 37.40 |
| 006 Heber RS | 6590 | 24.10, 36.00 |
| 007 Show Low City | 6400 | 29.20, 34.30 |
| 008 Pine Top Fish Hat | 8180 | 29.90, 32.80 |
| 009 Hawley Lake | 8180 | 31.50, 31.40 |
| 010 Greer | 8490 | 34.10, 31.80 |
| 011 Alpine | 8050 | 37.00, 29.90 |
| 012 Mt. Lemmon | 7794 | 22.20, 14.20 |
| 013 Chiricahua NM | 5300 | 35.55, 9.50 |

The model is generally unable to estimate point precipitation with high accuracy for a number of reasons that lead to highly variable precipitation records, and because of model shortcomings that include using a relatively coarse resolution such as 5- or 10-km grid spacing (Rhea, 1978). Modeling difficulties may include noticeable amounts of convective precipitation and the frequent occurrence of minor precipitation events, both of which the model is unable to properly simulate. The steady-state feature of the model also leads to errors, as most precipitation occurs in highly variable patterns in time and space. As a consequence of these various problems, model performance for point estimates varies substantially. However, should a special requirement arise for estimates at some particular point of the model domain, the model can sometimes be configured for better results at that point, but often at the expense of estimates at other locations.

As a consequence of difficulties in accurately estimating point precipitation, it was believed that model adaptation and application could be better accomplished by modeling to estimate the mean of Mogollon Rim gauge measurements, in particular, the mean of point estimates for the first 11 gauge locations given in table 3.1. Consequently, the mean of the nonmissing 11-gauge values was determined for each day. The model was configured to develop daily means from the 11-point model estimates for each day. (Actually, the model computes the precipitation for a 12-h period, from each input sounding. A separate computer code must be usd to add the 12-h totals for the daily amount.) Because the primary interest was modeling for a watershed, the

mean values provided a less noisy data set with which to adapt and calibrate the model for better simulation on the watershed scale.

## 3.4 Model Application to the Mogollon Rim

### 3.4.1 *Model Performance.*

**3.4.1.1 *Input Data.*** – The principal focus of the modeling was the Mogollon Rim and more specifically, the Salt River and Verde River watersheds. These watersheds drain southwestward into the Gila River. Both benefit from moisture flow with a westerly or southerly wind component and to a lesser extent with northwesterly flow. The Little Colorado River watershed is located immediately east of the rim summit, adjacent to the Salt-Verde watersheds (figs. 1.1 and 3.3). From winter storms with southwesterly winds, the western portion of the Little Colorado is subject to shadowing and, thus, receives less precipitation than windward exposed areas of the rim. The eastern region of the Little Colorado gradually increases in elevation and experiences significant orographic precipitation with moist northwesterly flow, whereas much of the Mogollon Rim parallels such flow and, consequently, is not favored for notable amounts except for higher areas of the San Francisco and White Mountains. No modeling was performed explicitly for the Little Colorado watershed.

Inputs required by the model included a computer file containing a description of the Salt and Verde watersheds. Likewise, a separate computer file was developed containing location information for each of the selected 13 precipitation gauges (table 3.1).

The principal inputs to the model are the soundings that specify the temperature, moisture, and wind profiles for each model run. Each sounding must be preprocessed for preparation for the model. The model requires estimates, at 50-mb increments, of the pressure, pressure height, temperature, relative humidity, and wind direction and speed. Specialized computer software not included in the model computer code was employed for developing the 50-mb interpolated estimates. Given in table 3.2 is a sample of a model-ready sounding from DRA. Because information above the 300-mb level is of no consequence to modeling results, that level was selected as the cutoff in each sounding. The highest pressure cutoff selected for DRA and TUS was 900 mb (or the surface pressure if lower) and for INW the cutoff was 850 mb (or the surface pressure if lower).

Table 3.2. – Sample sounding in model ready status.

841212 0 DRA72387 33

| 895.0 | 1007.0 | 10.6  | 0.619 | 240.0 | 5.0  |
| 850.0 | 1433.0 | 6.3   | .718  | 231.0 | 6.0  |
| 800.0 | 1926.0 | 1.8   | .937  | 221.0 | 6.0  |
| 750.0 | 2443.0 | -2.7  | .940  | 236.0 | 7.0  |
| 700.0 | 2988.0 | -4.1  | .449  | 262.0 | 8.0  |
| 650.0 | 3570.7 | -6.3  | .325  | 272.0 | 8.0  |
| 600.0 | 4192.8 | -9.7  | .272  | 273.0 | 11.0 |
| 550.0 | 4860.5 | -12.1 | .559  | 320.0 | 13.0 |
| 500.0 | 5583.0 | -15.2 | .399  | 343.0 | 24.0 |
| 450.0 | 6371.3 | -20.6 | .340  | 350.0 | 23.0 |
| 400.0 | 7232.0 | -27.3 | .499  | 1.0   | 32.0 |
| 350.0 | 8182.9 | -33.0 | .748  | 2.0   | 42.0 |
| 300.0 | 9253.0 | -40.4 | .120  | 4.0   | 54.0 |

A model run for each sounding time was performed only if all three soundings were available. Additionally, if a model run failed for one sounding period, then that day (two sounding periods) was assigned a missing designator. Because the historical data set consisted of nearly 1800 days, it was felt that an occasional missing day would not noticeably impact precipitation comparisons. However, missing wet days may contribute to streamflows and, therefore, model comparisons with those values could be affected.

**3.4.1.2 Model Estimates of Daily and Monthly Precipitation.** – Comparisons of modeled versus gauge precipitation were made with the daily 11-gauge means. Potentially, 1812 data pairs could have been used for comparisons. Without stratification of the data as to, for example, wind direction, 1683 nonmissing pairs existed, as indicated in table 3.3. Thus, 129 days, or 7.1 percent, were determined as missing because of soundings problems. With 0-0 cases (model estimate and the respective gauge mean both zero) eliminated, the sample size was reduced to 840 pairs. This figure suggests that, on the average, some 84 precipitation days (days with non-zero precipitation in at least one of the 11 gauges) occurred per winter of the 10-winter data set. Gauge data indicated the number was 86 precipitation days per winter. Model runs indicated that the model generally underestimated the frequency of precipitation days. This discrepancy is believed to be caused primarily by model inability to correctly estimate precipitation from weak weather systems that produce little precipitation.

Table 3.3. – Comparison of model estimates of daily and monthly precipitation with respective Mogollon Rim 11-gauge means over 10 winters.

| Gauge precipitation sum (mm) | Model precipitation sum (mm) | Cases | Correlation with 0-0 pairs | Cases | Correlation without 0-0 pairs |
|---|---|---|---|---|---|
| 3326.2 | 3369.3 | 1,683 (days) | 0.75 | 840 | 0.72 |
|  |  | 60 (months) | 0.92 | 60 | 0.92 |

A simple basis of comparison of the model estimates versus corresponding gauge values was required. Based on previous experiences with applications of the model to other mountainous areas, the Pearson correlation was determined adequate for this purpose.

As indicated in table 3.3, the model estimated 3369.3 mm of precipitation during 1683 nonmissing days. Gauge precipitation for those days was 3326.2 mm, indicating the model overestimated the measured 10-winter total by 1.3 percent. The correlation of measured versus modeled precipitation was 0.75. With 0-0 cases eliminated, the correlation was 0.72. These values are considered respectable, given that daily precipitation measurements were employed over the full 6-month period of November through April. When the winter period was reduced to 5 months by excluding April, the correlation increased slightly to 0.77 with 0-0 cases included. As will be shown later, the model performance on April soundings is poor in comparison to the other winter months. Precipitation during April is generally more convective in nature, thus negatively affecting the performance of the precipitation model.

Of interest also was whether integration in time that yielded monthly sums for gauge and model values would lead to higher correlations. With monthly totals, the sample size decreased to 60 months (table 3.3). The correlation increased to 0.92 (the same with 0-0 cases included and excluded) from 0.75 obtained with daily values. Clearly, the explained variance ($r^2$) was noticeably improved by the integration over time (0.85 vs. 0.56).

The correlation values given in table 3.3 consider all nonmissing precipitation over the entire 10-winter period. Also of interest is the model's performance in each of the 10 winters and in each month of winter. Noticeably lower or higher performance for some year or, for example, all Januarys of the data, may be associated with certain weather regimes.

Table 3.4 and figure 3.4 give the results of comparison of model estimates with 11-gauge means for each of the 10 winters. The number of days modeled per winter varied from a low of 145 days for 1987-88 to 181 days for each of 1981-82 and 1983-84. Measured precipitation for days modeled of each winter ranged from a low of 174.2 mm during 1983-84 to a high of 535 mm in 1978-79, an amount more than 3 times the low value. With 0-0 cases included, correlation values of modeled versus gauge precipitation ranged from 0.43 to a high of 0.91, with a mean value of 0.70 and a median value of 0.765. Figure 3.4 indicates that lower correlation values were generally associated with lower precipitation values.

Figure 3.4. – Model precipitation estimates versus 11-gauge
means for each of 10 winters.

Table 3.4. – Comparison of model estimates with Mogollon Rim
11-gauge mean precipitation for each of 10 winters.

| Winter | Gauge precipitation sum (mm) | Model precipitation sum (mm) | Cases | Correlation with 0-0 pairs | Cases | Correlation without 0-0 pairs |
|--------|------|------|-----|------|-----|------|
| 1978-79 | 535.0 | 634.2 | 173 | 0.91 | 98 | 0.90 |
| 1979-80 | 455.1 | 425.2 | 174 | 0.68 | 80 | 0.61 |
| 1980-81 | 195.8 | 194.1 | 180 | 0.76 | 71 | 0.69 |
| 1981-82 | 331.3 | 285.0 | 181 | 0.69 | 81 | 0.63 |
| 1982-83 | 457.4 | 497.1 | 180 | 0.71 | 109 | 0.67 |
| 1983-84 | 174.2 | 187.4 | 181 | 0.50 | 81 | 0.43 |
| 1984-85 | 367.5 | 379.2 | 157 | 0.77 | 95 | 0.74 |
| 1985-86 | 236.5 | 232.9 | 152 | 0.43 | 77 | 0.34 |
| 1986-87 | 292.0 | 240.0 | 160 | 0.77 | 81 | 0.75 |
| 1987-88 | 281.5 | 294.1 | 145 | 0.82 | 67 | 0.82 |

Study of the model performance for individual days of the seasons (indicated in table 3.4) with lower correlations, suggested difficulties in modeling low precipitation events. This difficulty is not surprising considering that the model is initialized only once per 12 h and that initial conditions are taken to apply for 12 h because the model is steady state. In many storms the horizontal moisture profile is quite inhomogeneous. The moisture may flow across the Mogollon Rim in bands spaced at unequal distances. Sounding measurements can easily misrepresent the mean moisture profile that is desired for the steady state model.

Because the model was developed to estimate orographic precipitation, performance was expected to deteriorate somewhat with storms generating noticeable convection. The latter

would lead to more highly variable precipitation in space and, consequently, lower correlations in comparison studies. On the Mogollon Rim, convective storms generally become much more evident in April and so the model performance was anticipated to drop for April days.

Performance by the model for each of the 6 months of the winter is indicated in table 3.5 and figure 3.5. Like months were analyzed together (e.g., all Januarys) and the time unit for each sample pair of the data set was a day. Gauge and model values were developed for each day in the usual manner.

Table 3.5 shows that, generally, the measured monthly precipitation varied about 100 mm during the winter with the exception of April when it dropped by nearly one-half, indicative of a significantly dryer period. With 0-0 cases included, comparisons indicated the highest correlation, 0.85, was obtained for December and the lowest value, 0.37, occurred with April data. Examination of the gauge daily data for April indicated a substantial increase over other winter months of the number of light precipitation events.
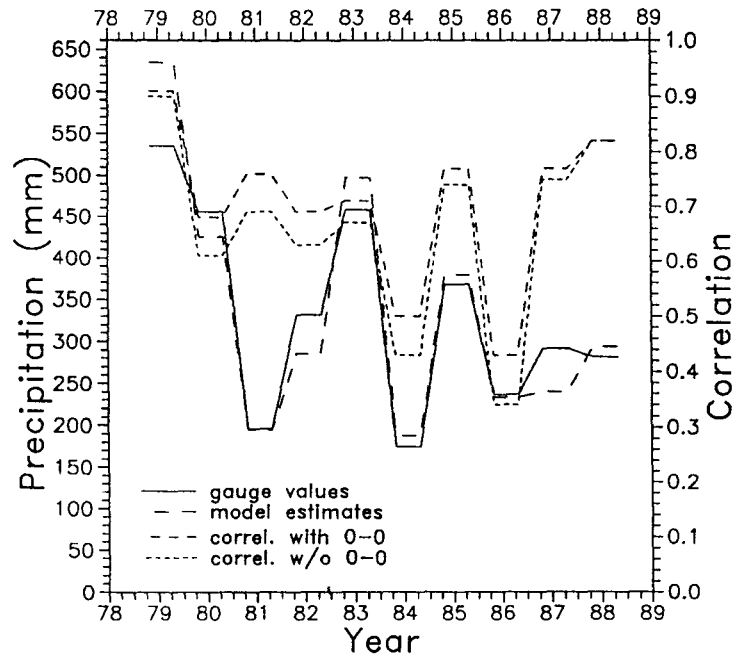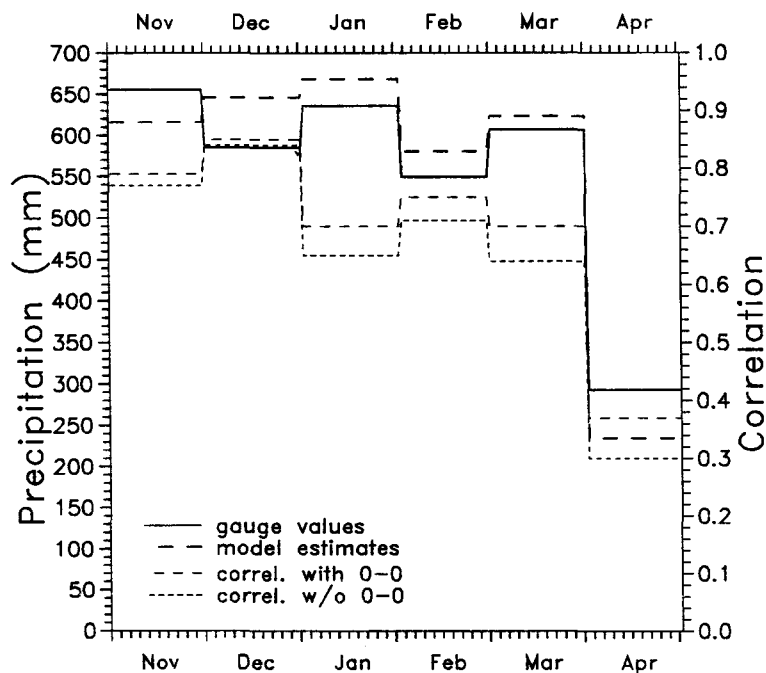


Figure 3.5. – Model precipitation estimates versus 11-gauge means for each winter month.

69

Table 3.5. – Comparison of model results with Mogollon Rim 11-gauge mean precipitation
for each month of November through April.

| Month | Gauge precipitation sum (mm) | Model precipitation (mm) | Cases | Correlation with 0-0 pairs | Cases | Correlation without 0-0 pairs |
|---|---|---|---|---|---|---|
| November | 655.6 | 616.0 | 282 | 0.79 | 126 | 0.77 |
| December | 585.0 | 646.2 | 289 | 0.85 | 135 | 0.84 |
| January | 635.9 | 668.8 | 294 | 0.70 | 157 | 0.65 |
| February | 549.6 | 580.6 | 257 | 0.75 | 134 | 0.71 |
| March | 607.3 | 623.3 | 276 | 0.70 | 153 | 0.64 |
| April | 292.8 | 234.4 | 285 | 0.37 | 135 | 0.30 |

**3.4.1.3 *Point Precipitation Estimation*.** – Precipitation estimates were developed by the model for each of the 13 gauge locations listed in table 3.1. Of these, nine gauges were selected for comparison studies to examine how well the model estimated point precipitation at locations of relatively higher terrain over different areas of the model domain. The nine gauges employed are listed below and their locations are shown on figure 3.3. The seven gauges, (a) through (g), were distributed along the Mogollon Rim and believed to produce the better data for that area. Gauges (h) and (i) were positioned just northeast of Tucson and well southeast of Tucson, respectively.

  a. Flagstaff
  b. Happy Jack Ranger Station
  c. Blue Ridge Ranger Station
  d. Heber Ranger Station
  e. Pine Top Fish Hatchery
  f. Hawley Lake
  g. Greer
  h. Mt. Lemmon
  i. Chiricahua National Monument.

Correlations were developed of gauge measurements versus model estimates, with daily and, separately, with monthly sums. Given in table 3.6 are comparison results for the nine gauges. Study of the precipitation totals reveals the model performance extremes of an underestimate of 47 percent and an overestimate of 54 percent. Individual underestimated or overestimated percentage values for the nine gauges (a) through (i) were -33, -17, -39, -47, 3, 19, 54, -25, and -20, respectively. Generally, the model underestimated precipitation at northern gauges of the Mogollon Rim and overestimated it in the White Mountains located in the southeastern part of the rim. The model also underestimated precipitation at the two southern located gauges.

Table 3.6. – Comparison of model estimates with individual gauge precipitation with daily sums and monthly sums of the 10-winter data set.

| Gauge | Gauge precipitation sum (mm) | Model precipitation sum (mm) | Cases | Correlation with 0-0 pairs | Cases | Correlation without 0-0 pairs |
|---|---|---|---|---|---|---|
| Flagstaff | | | | | | |
| (daily sums) | 3722.6 | 2503.2 | 1812 | 0.59 | 604 | 0.52 |
| (monthly) | 3722.6 | 2503.2 | 60 | 0.81 | 59 | 0.81 |
| Happy Jack RS | | | | | | |
| (daily sums) | 4462.8 | 3701.5 | 1683 | 0.49 | 840 | 0.37 |
| (monthly) | 4462.8 | 3701.5 | 60 | 0.80 | 59 | 0.80 |
| Blue Ridge RS | | | | | | |
| (daily sums) | 3053.6 | 1848.1 | 1726 | 0.53 | 432 | 0.40 |
| (monthly) | 3053.6 | 1848.1 | 60 | 0.75 | 58 | 0.74 |
| Heber RS | | | | | | |
| (daily sums) | 2264.7 | 1208.3 | 1672 | 0.63 | 404 | 0.52 |
| (monthly) | 2264.7 | 1208.3 | 60 | 0.81 | 59 | 0.81 |
| Pine Top FH | | | | | | |
| (daily sums) | 3382.8 | 3492.8 | 1610 | 0.60 | 461 | 0.50 |
| (monthly) | 3382.8 | 3492.8 | 59 | 0.89 | 58 | 0.89 |
| Hawley Lake | | | | | | |
| (daily sums) | 5573.0 | 6658.4 | 1735 | 0.54 | 609 | 0.43 |
| (monthly) | 5573.0 | 6658.4 | 58 | 0.85 | 58 | 0.85 |
| Greer | | | | | | |
| (daily sums) | 2565.6 | 3961.6 | 1668 | 0.66 | 569 | 0.55 |
| (monthly) | 2565.6 | 3961.6 | 57 | 0.80 | 57 | 0.80 |
| Mt. Lemmon | | | | | | |
| (daily sums) | 958.3 | 715.8 | 543 | 0.32 | 92 | 0.13 |
| (monthly) | 958.3 | 715.8 | 20 | 0.39 | 20 | 0.39 |
| Chiricahua NM | | | | | | |
| (daily sums) | 2256.3 | 1800.6 | 1613 | 0.45 | 385 | 0.28 |
| (monthly) | 2256.3 | 1800.6 | 58 | 0.63 | 57 | 0.62 |

Study of gauge locations (fig. 3.3) and modeling results in table 3.6 suggested that comparison results depended noticeably on gauge position with respect to mountain crests. Under northwesterly flow the moist air is forced, by the two-dimensional feature of the model, to nearly parallel the Mogollon Rim. This flow may lead to a weak cross-barrier component and, consequently, little precipitation developed by the model. In reality, the three-dimensional flow often tends to turn somewhat perpendicular to the barrier and thus becomes more favorable to orographic precipitation. Additionally, the gauges Blue Ridge RS and Heber RS, are located downwind of the rim crest under winds with westerly components, thus leading to greater

variability in model estimates as a result of shadow effects. The gauges Hawley Lake and Greer are favorably located for orographic precipitation under northwesterly winds.

Figure 3.6 shows a sample of model precipitation for January 1979, with only northwesterly flow cases modeled. The precipitation over the White Mountains and vicinity is overestimated; over the central and northwestern part of the Mogollon Rim, precipitation is underestimated.
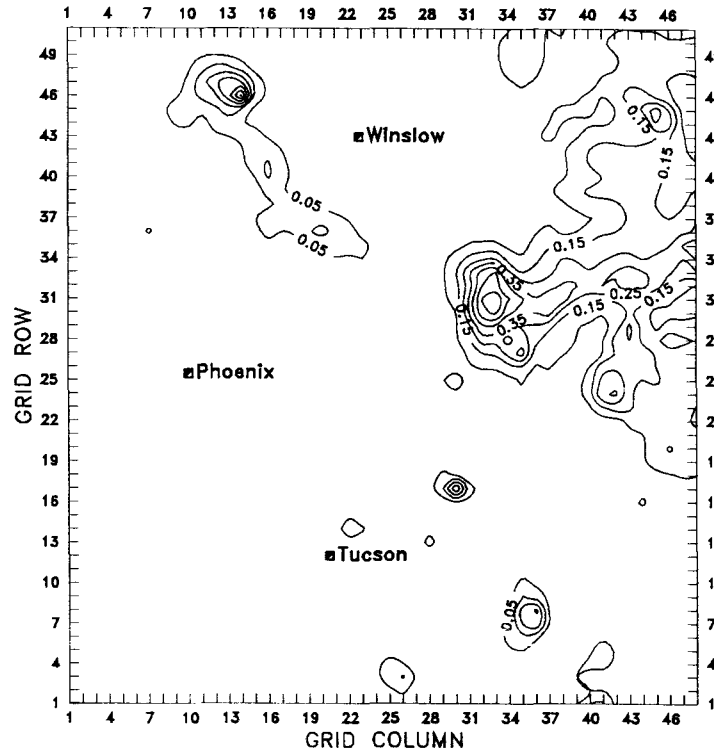


Figure 3.6. – Model precipitation for January 1979 produced
with northwesterly winds. The grid spacing is 10 km.

Correlation values of gauge versus modeled precipitation, for each of the nine gauges, are given in table 3.6. With 0-0 cases included, correlations for daily amounts range from 0.32 for Mt. Lemmon to a high of 0.66 at Greer. The average correlation for the nine gauges was 0.53. For the seven gauges located on the Mogollon Rim, the average correlation was 0.58. Values were a bit lower for the northern three gauges of the rim with a mean correlation value of 0.54 versus 0.60 for the three gauges in the White Mountains.

The precipitation record for Mt. Lemmon contained considerable missing information to the extent that data for only 20 of 60 months were analyzed. Correlations of gauge versus modeled daily precipitation were 0.32 and 0.13 with and without 0-0 cases, respectively. For the Chiricahua NM gauge, the data set consisted of precipitation for 58 of 60 months. Correlation values with and without the 0-0 cases were 0.45 and 0.28, respectively.

When monthly precipitation sums were employed rather than daily totals, table 3.6 shows that correlation values improved noticeably, indicating that integration over time reduced data noise substantially. The overall range of correlation values was 0.39 to 0.89. The average correlation for the nine gauges was 0.75. Elimination of the two southern gauges improved the

72

average correlation to 0.82. Least improvement in the correlation from daily to monthly totals occurred in data for the two southern gauges.

Model performance for the two southern locations was expected to be inferior to performance for gauges on the Mogollon Rim. This inferior performance was caused primarily by model tuning for the Mogollon Rim, a gradual progression with decreasing latitude of conditions unfavorable to orographic precipitation, and a less favorable orography at southern gauge locations.

In general, correlation values determined in this study with daily precipitation for individual gauges were somewhat lower than those obtained in other geographical areas (El Majdoub, 1989; Rhea, personal communication), although those studies employed shorter data sets. Correlations of about 0.75 were obtained for two gauges by El Majdoub in modeling 40 days for the Atlas Mountains of Morocco. The availability of favorably located local soundings likely enhanced results in Morocco. Similar values were obtained by Rhea with small data sets from the American-Feather watersheds in California.

In summary, integration in time improved correlation values noticeably, particularly for the seven gauges analyzed individually from the Mogollon Rim. Integration over space obtained through computation of the 11-gauge means also improved results. When both integration over time and space were applied to data for the Mogollon Rim gauges, a correlation of 0.92 was obtained, employing 11-gauge daily means summed monthly versus like model estimates. The 0.92 correlation is noticeably higher than the 0.75 obtained with daily data. Unfortunately, results are not currently available of application of the model on a daily basis in other geographical areas over a comparable length period of at least 10 winters. Applications of the model in other watersheds of the western U. S. are now commencing and should furnish new results for comparisons.

### 3.4.2 *Model Runs for Winter Storm Climatology Study.* –

**3.4.2.1 *Temperature Character at 750-mb and 500-mb Levels.*** – Temperatures in the cloud layer from the height of the barrier crest [typically near 2.25 km m.s.l. (mean sea level) on the Mogollon Rim] to about 700 m a.g.l. (above ground level) are important to the efficacy of cloud treatment by ground-based seeding applications of a glaciogenic agent such as silver iodide (e.g., Super et al., 1989) . Super et al. (1989) found that this layer contained the highest concentrations of cloud liquid water, which is essential to successful cloud seeding. Tracer plumes released from the ground often reached 700 m a.g.l. before passing the barrier crest. An important precondition for proper application of the treatment agent is sufficiently cold temperatures, at least -6 °C, in the desired cloud zone where the supercooled liquid water is located and the treatment agent is able to reach and disperse. Temperatures as low as -6 °C or lower are required for silver iodide nuclei to initiate ice crystals in desired numbers. In Arizona winter storms, the desired moist level is often near 750 mb. Because cloud seeding experiments are being contemplated in Arizona, a study was performed with the model of 750-mb temperatures that accompany winter storms. The results, which may be useful to determining the feasibility of ground seeding applications for the Mogollon Rim, are given in table 3.7.

Table 3.7. – Model estimates with corresponding Mogollon Rim 11-gauge mean precipitation for 750-mb and 500-mb temperature stratifications, using the mean of DRA and TUS temperatures.

| Temperature interval (°C) | Gauge precipitation sum (mm) | Model precipitation sum (mm) | Cases | Correlation with 0-0 pairs | Cases | Correlation without 0-0 pairs |
|---|---|---|---|---|---|---|
| $T_{750} > 0$ | 3030.7 | 3152.4 | 1622 | 0.75 | 784 | 0.72 |
| $T_{750} > -6$ | 3319.7 | 3363.7 | 1679 | 0.75 | 836 | 0.72 |
| $-10 \geq T_{500} \geq -27$ | 3057.0 | 2893.6 | 1596 | 0.74 | 787 | 0.71 |
| $T_{500} < -27$ | 107.5 | 73.9 | 14 | 0.93 | 14 | 0.93 |
| All cases | 3326.2 | 3369.3 | 1683 | 0.75 | 840 | 0.72 |

Additional results of temperature studies are given in table 3.7. Some cloud seeding studies (e.g., Mielke, et al., 1971; Grant and Elliott, 1974) have suggested that certain temperatures at the 500-mb level (about 5600 to 5700 m during Arizona storms) favor positive results from seeding winter clouds with those temperatures. Those studies also suggested that if 500-mb temperatures are lower than about -27 °C, positive seeding results are much less likely. Consequently, the model was also applied to examine 500-mb temperatures during winter storms that produced precipitation on the Mogollon Rim.

Table 3.7 gives comparison results of model runs for several upper air temperature stratifications. Because each sounding of the full 10-winter data set was interpolated to 50-mb increments, necessary temperatures were readily available. Stratification was performed according to the mean of DRA and TUS temperatures at the 750-mb level and, separately, at the 500-mb level (temperatures at the 750-mb level at INW are likely to be noticeably distorted because of the effects of flow over the Mogollon Rim).

In particular, results are included in table 3.7 for days when the 750-mb temperature exceeded 0 °C and when it exceeded -6 °C. Other stratifications included are 500-mb temperatures ( -27 °C and -10 °C), and 500-mb temperatures less than -27 °C. Results are also given, for comparison purposes, for the pooled data set consisting of all cases, regardless of temperature.

In 1683 modeled days, 1679 cases had 750-mb temperatures exceeding -6 °C, and so virtually all gauge precipitation occurred with temperatures warmer than desirable at this level for ground-based seeding applications. However, of 3326.2 mm total precipitation, only 107.5 mm (in 14 days) occurred with 500-mb temperatures less than -27 °C. When 500-mb temperatures exceeded -10 °C, 161.7 mm (4.9 percent of the total measured on modeled days) of precipitation occurred. These warm cases likely involved some convective clouds. In summary, neither 500-mb temperature extremes appear to often accompany winter storms. However, warm temperatures at 750 mb were common and will likely influence future cloud treatment methodology.

Though the results in table 3.7 indicate frequent warm temperatures at 750 mb, thus negatively affecting ground-based seeding with silver iodide, the actual temperatures in the vicinity of the Mogollon Rim are probably one or 2° colder than the results obtained in this study. These differences were observed in comparisons of temperatures from soundings taken

at Camp Verde with those from TUS, INW, and DRA soundings. Consequently, temperature limitations on ground-based seeding are not quite as bleak as the results in table 3.7 suggest.

Table 3.7 shows that correlation values for modeled versus measured precipitation differed little with different temperature stratifications. The high correlation of 0.93 for 14 cases with 500-mb temperatures less than -27 °C is likely an aberration (rather high correlation) caused by the small sample size. However, it would not be surprising that the model would perform well in cold cases because clouds on such days may be largely orographic in character.

**3.4.2.2** *Wind Direction Studies.* – Super et al. (1989) found that during January through March of 1987 and 1988, southwesterly moist flow contributed most precipitation that occurred on the Mogollon Rim. It was determined to run the model with soundings for 10 winters to study this phenomenon on a much larger data set. Model runs were made for daily cases stratified according to four 700-mb wind direction classes corresponding to the four quadrants of the compass. The model determined the key wind direction, for each sounding period, by taking the mean of the 700-mb values at INW and TUS. The 700-mb winds were selected because they frequently indicate cloud movement.

Table 3.8 contains the results of model runs with stratification by wind direction. These results indicate that 88 percent of the Mogollon Rim gauge precipitation (of days accepted for model runs) occurred with a 700-mb wind direction from the southwest quadrant, that is, winds of 190 to 270°, inclusive. Storms with winds from the northwest quadrant contributed 8 percent of the precipitation. The southeast and northeast quadrants contributed 3.5 and 0.3 percent, respectively. Northeast quadrant storms contributed essentially no precipitation. Precipitation given in the table for the four quadrants does not total to the amount measured for all cases because of the rejection of cases (594 days designed as missing, during which about 22 percent of the precipitation occurred) when the two soundings for a day had 700-mb wind directions from different quadrants.

Table 3.8. – Model estimates with corresponding Mogollon Rim 11-gauge mean precipitation stratified according to the mean of 700-mb winds for INW and TUS.

| Wind direction interval (°) | Gauge precipitation sum (mm) | Model precipitation (mm) | Cases | Correlation with 0-0 pairs | Cases | Correlation without 0-0 pairs |
|---|---|---|---|---|---|---|
| [10,90] | 7.8 | 6.1 | 91 | 0.34 | 8 | 0.06 |
| [100,180] | 91.1 | 107.4 | 49 | 0.40 | 31 | 0.31 |
| [190,270] | 2299.2 | 2428.0 | 627 | 0.77 | 399 | 0.74 |
| [280,360] | 207.5 | 121.2 | 322 | 0.44 | 125 | 0.29 |
| [10,360] | 3326.2 | 3369.3 | 1683 | 0.75 | 840 | 0.72 |

Sample sizes given in table 3.8 with 0-0 cases eliminated indicate that relatively few precipitation events occur with 700-mb winds with an easterly component. The total precipitation from easterly cases was about one-half the amount for northwesterly flow cases. These results suggest that moist southwest flow leads to most winter precipitation on the Mogollon Rim.

Division of the gauge precipitation given in table 3.8, in each category, by the number of cases remaining after 0-0 cases are eliminated, produces an estimate of the mean precipitation per day. For southwest flow cases, this quantity was 5.8 mm/day; for northwest flow cases, 1.7 mm/day; for northeast flow cases, 1.0 mm/day; and for southeast flow cases, 2.9 mm/day. Clearly, the southwest flow cases are far more productive in producing precipitation than flow cases from the other quadrants.

**3.4.2.3 *Wind Speed Studies.*** – The model was employed to study steering level wind speeds that accompany storm days on the Mogollon Rim. Wind speeds affect where precipitation is deposited. High wind speeds potentially can transport some cloud particles (both water and ice) over the barrier summit where they may fall as precipitation or evaporate. The fallout of additional ice crystals by seeding in clouds with strong winds may not occur at desired locations unless winds have been factored into the treatment process. On the other hand, weak winds may lead to minor amounts of cloud liquid water flux, generally an undesirable cloud seeding condition. More information is required on the distribution of cloud liquid water and winds, in space and time, in the vicinity of the Mogollon Rim, to better determine favorable and unfavorable wind speed conditions to precipitation and cloud seeding feasibility.

The key winds selected were the 700-mb level winds. Model runs were stratified according to the mean, designated as $U_{700}$, of INW and TUS 700-mb wind speed components in the direction selected as representative of the 700-mb flow direction. Three stratums of the 700-mb wind speed were selected for analysis: (a) $U_{700}$ <5 m/s, (b) $U_{700}$ >15 m/s, and (c) 15 $\geq U_{700}$ $\geq$5 m/s. The selection of these intervals for Arizona was aimed at studying what are generally considered weak, strong, and moderate winds, respectively, for winter storms on the Mogollon Rim.

In the wind speed analysis, the goal was to study the relationship of wind speeds to precipitation amounts and occurrences. Given in table 3.9 are the results of model runs stratified by the three selected wind speed intervals. Study of the sum of daily 11-gauge mean precipitation over the three speed categories indicates that 59 percent of the precipitation included in the three intervals occurred at speeds of 5 to 15 m/s, inclusive. Thirty-six percent of the precipitation occurred with the highest wind speeds, and only four percent occurred with the lowest wind speeds. The mean precipitation amount was 12.8 mm/day for the higher speed stratification, 3.0 mm/day for the intermediate speed interval, and 1.1 mm/day for the lowest speed stratification. These results indicate that the more productive precipitation episodes occured with higher 700-mb wind speeds, suggesting that those storms are efficient producers of precipitation and that blow-over (over the crest) of the precipitation does not substantially decrease amounts near the crest. However, there were relatively few days with precipitation (denoted by the model or gauges with 0-0 cases eliminated) under high wind speed conditions. For the 254 cases with the weakest winds, the correlation of model estimates versus gauge values was 0.39, which is a relatively poor value.

Table 3.9. – Model estimates with corresponding Mogollon Rim 11-gauge mean precipitation for some 700-mb wind speed stratifications, using the mean wind for INW and TUS.

| Wind interval (m/s) | Gauge precipitation sum (mm) | Model precipitation sum (mm) | Cases | Correlation with 0-0 pairs | Cases | Correlation without 0-0 pairs |
|---|---|---|---|---|---|---|
| $U_{700}<5$ | 82.2 (4%) | 50.3 | 254 | 0.39 | 73 | 0.21 |
| $U_{700}>15$ | 706.0 (36%) | 683.8 | 68 | 0.75 | 55 | 0.73 |
| $15 \geq U_{700} \geq 5$ | 1151.1 (59%) | 992.6 | 746 | 0.62 | 384 | 0.57 |

Gauge precipitation in table 3.9 does not total to 3326.2 mm, which was obtained for all days of the 10 winters for which 3 soundings were available. The discrepancy was caused by sounding periods applying to different stratifications.

A problem worthy of further study is the determination of cloud seeding feasibility of cases with ample moisture but weak winds. This study suggests that about as many wet cases (days with measurable precipitation at Mogollon Rim gauges) occur with weak winds as with strong winds, but little natural precipitation occurs on weak wind days. The weak winds lead to relatively low moisture flux over the barrier and, therefore, less fuel for precipitation. However, perhaps early seeding or some other seeding strategy of weak wind cases could increase their precipitation efficiency.

**3.4.3 Precipitation Volume Comparisons With Streamflow.** – The model integrates precipitation for specified watersheds and over desired time periods, such as monthly. Estimates of volume precipitation can then be employed as an independent variable in regression analysis, with selected streamflow measurements as the dependent variable. Regression equations may be useful in obtaining early estimates of seasonal runoff. Other independent variables can be included in multiple regression analysis to, perhaps, further improve runoff forecasting capability.

In this application, streamflow data were obtained from the three stream gauges listed below:

| Gauge | Record |
|---|---|
| Salt R. near Roosevelt (Station 09498500) | November through June of water years, 1979-88, inclusive |
| Tonto Cr. above Gun Cr. (Station 09499000) | As above |
| Verde R. below Tangle Cr., above Horseshoe Dam (Station 09508500) | As above |

Gauges were selected such that the high elevation areas of the Salt-Verde watersheds were covered, yet confounding by upstream diversions, reservoirs, and return flows did not

appreciably influence results. Salt River and Tonto Creek flows measured at the gauging stations indicated above were combined to represent more encompassing Salt River flows.

Separate monthly and seasonal analyses were performed. Gauge seasonal sums consisted of November through June flows. Because river hydrographs indicated that spring runoff persists into June. Model seasonal volume precipitation was generated by integration over the period November through April.

Linear regression analysis was performed on monthly data and, separately, on seasonal data. Sample sizes were 60 cases (months) in the monthly analysis and 10 cases (winters) in the seasonal analysis. Given in table 3.10 are correlation values resulting in each analysis. Scatterplots with regression lines are given on figures 3.7 and 3.8. The regression equations developed are defined in table 3.11.

Table 3.10. – Comparison of Salt River and Verde River flows with model volume precipitation estimates.

| Watershed (time unit) | Cases | Correlation |
|---|---|---|
| Verde R. (monthly) | 60 | 0.66 |
| Salt R. (monthly) | 60 | 0.56 |
| Verde R. (seasonal) | 10 | 0.84 |
| Salt R. (seasonal) | 10 | 0.97 |

Table 3.11. – Regression equations for seasonal streamflow in the Salt and Verde watersheds.

Verde River watershed regression:

$\hat{y} = 0.397x - 21.051$,     $\hat{y}$ = Gauge streamflow summed November through June
                          $x$ = Model volume precipitation summed for November through April

Salt River watershed regression:

$\hat{y} = 0.480x - 354.008$     $\hat{y}$ and $x$  defined as above.

## Verde River Watershed



$$y = 0.397x - 21.0$$
$$r = 0.84$$
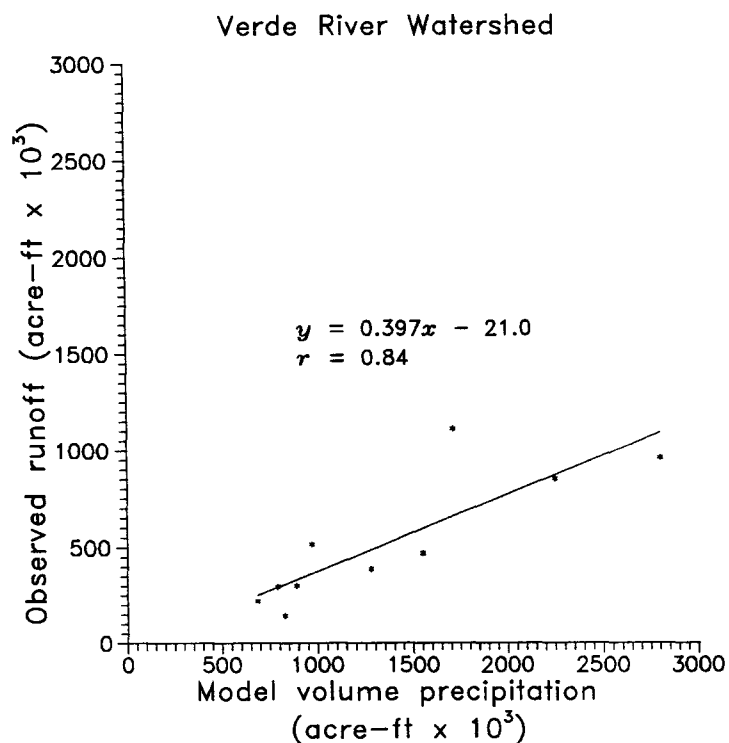
Figure 3.7. – Scatterplot of observed seasonal streamflow vs. model volume precipitation for the Verde River watershed.

## Salt River Watershed
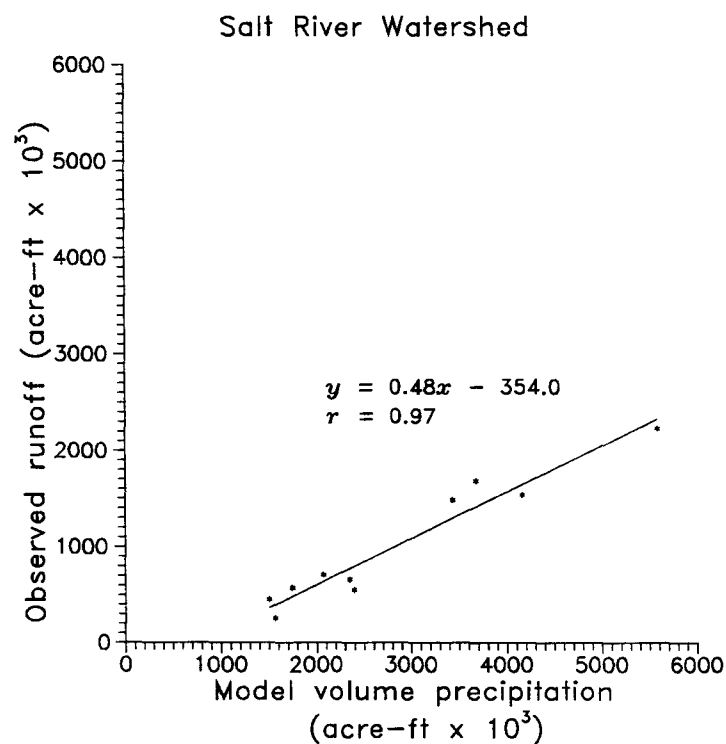


$$y = 0.48x - 354.0$$
$$r = 0.97$$

Figure 3.8. – Scatterplot of observed seasonal streamflow vs. model volume precipitation for the Salt River watershed.

For Verde River data, the correlation was 0.66 with monthly flows and 0.84 with seasonal flows. For Salt River data the respective correlation values were 0.56 (monthly) and 0.97 (seasonal). The correlations with monthly flows were noticeably higher than the 0.4 correlation obtained with flows into Bin El Ouidane Reservoir in the Atlas Mountains of Morocco (Matthews et al., 1989). The higher values for Arizona suggest that a noticeable amount of the winter precipitation that occurs on the Salt-Verde watersheds runs off within a few days to a couple of weeks rather than remains in snowpack storage for extended periods.

The difference in correlation between the Verde River and Salt River watersheds in the seasonal analysis is largely caused by the presence of one outlier in the Verde River data (fig. 3.7). A correlation value as large as 0.97 for the Salt River seasonal flows would not likely be obtained from a larger sample. These results suggest that a larger data set would lead to correlations near 0.85. No noticeable skill difference is apparent in the model performance over the two watersheds. Employing a sample size of 13 seasons, Rhea (1978) obtained correlations from 0.62 to 0.91 in 20 Colorado mountain watersheds.

The variance explained ($r^2$) in the monthly analysis (monthly time units) was 31 percent and 44 percent for the Salt and Verde watersheds, respectively. These values reflect a regression model that is not adequate to forecast monthly streamflows. Other more capable models exist for this purpose. A better approach would be to employ the daily grids of precipitation produced by the precipitation model as input to a physical hydrologic model which produces daily streamflow estimates through the use of more sophisticated and encompassing physics.

The seasonal analysis (seasonal time units) produced explained variances of 71 percent and 94 percent for the Salt and Verde watersheds, respectively. These results suggest useful capability in forecasting seasonal flows by this type of a regression model. However, the precipitation model requires November through April soundings to develop the seasonal volume precipitation. To employ this type of regression for seasonal forecasting, say in early February or March, one would need to assume some range of values for the volume precipitation not yet experienced. By assuming selected percentages of the long-term mean volume precipitation for the period of missing data, this forecasting system could supplement other forecasting procedures now in use for the Salt and Verde watersheds.

## 3.5 Summary and Recommendations

An existing grid-point orographic precipitation model was adapted for application to the Mogollon Rim of Arizona. The model is two-dimensional, steady-state, multilayer, and fast-running on recent microcomputers or workstations. In the current configuration, the model only requires interpolated soundings from DRA, INW, and TUS as input. The model produces estimates of precipitation at each grid point of the 10-km model domain and other selected locations that currently are specified as the sites of 13 gauges, 11 of which are distributed along higher areas of the Mogollon Rim. The model also integrates precipitation over defined watersheds and time periods.

The adapted model was applied to the Mogollon Rim with input consisting of twice-per-day interpolated soundings for the 10 winters of 1978-88. A correlation of 0.75 was obtained for model estimates of daily precipitation, defined as the mean of 11-point values that corresponded to the 11 Mogollon Rim gauges, versus the corresponding gauge mean values, each developed by taking the mean of the non-missing gauge values (up to 11 each day) each

day. When monthly totals were employed the correlation increased to 0.92. Values for point locations were lower, near 0.6, indicating that averaging model estimates over a watershed improves results. Correlation of seasonal streamflow, obtained by summing gauge monthly flows over November through June, with November through April model volume precipitation, yielded 0.97 for the Salt River watershed and 0.84 for the Verde River watershed.

Correlation values obtained indicate the model has useful predictive capability for the Salt-Verde watersheds. This capability exists for daily precipitation areal averages and, particularly, for monthly totals for which the model seems capable of explaining nearly 85 percent of the variance. These results suggest that model daily grid-point estimates of precipitation may be sufficiently accurate to be employed as input to physical hydrologic models, providing them vital improved resolution of the precipitation in space. Although use of the model in an areal sense over the two watersheds appears feasible, single point estimates were noticeably less accurate and should be used with caution.

The model may be of use in forecasting seasonal streamflow. For example, probable seasonal runoffs can be developed using model generated monthly volume precipitation for months with soundings plus adjusted mean flows for the remaining months of a season. Model forecasts of seasonal streamflow can also be employed in the evaluation of cloud seeding programs to increase watershed streamflow.

The model can be useful in the study of winter storm climatology. Application of the model to the Mogollon Rim confirmed that most precipitation, about 88 percent of the total, occurs from storms bearing southwesterly steering winds. Though nearly one-third as many precipitation days occur with northwesterly winds as with southwesterly winds, they produce only about 8 percent of the precipitation on the rim, perhaps indicative of inefficient cloud precipitation processes (could also be caused by low CLW from inefficient lift of air layers because the flow is somewhat parallel to the Mogollon Rim).

Moist layer temperatures play a vital role in the formation and growth of cloud ice particles and in cloud precipitation efficiency. Consequently, the model was employed to examine the temperatures at levels important to cloud seeding by ground-based application, and the 500-mb level temperatures that have been of interest to some seeding programs. Model runs indicated that precipitation events on the Mogollon Rim frequently occur with 750-mb (about 2.5 km m.s.l.) temperatures exceeding -6 °C, which may present special problems to ground-based seeding applications. On the other hand, about 92 percent of the precipitation occurred at 500-mb temperatures estimated at -27 °C to -10 °C, an interval considered by some scientists to be favorable to cloud seeding.

Wind speed can also play an important role in precipitation production. As in the case of temperatures, the model was employed to investigate wind speeds that accompanied precipitation days on the Mogollon Rim. Model runs indicated that about 36 percent of rim precipitation occurred with 700-mb winds exceeding 15 m/s and less than 5 percent occurred with winds less than 5 m/s. Cloud treatment when winds exceed 15 m/s may sometimes present formidable targeting problems. That little precipitation occurred with weak winds may mean that, in some cases, clouds were relatively stable and producing precipitation with low efficiency. Whether cloud seeding can be productive in such cases requires more field studies and experimentation.

Application of the model to the Mogollon Rim indicated useful skill in the estimation of daily mean precipitation for 11 gauges located in higher elevations of the rim. With relatively minor changes, the model can be configured to use a single sounding as input. In future cloud seeding experiments that collect local sounding data, the model should be used to estimate precipitation for the rim and results compared with gauge data. The model can be configured to develop estimates for periods with less than 24 h and this feature may be useful in the development of weather forecasts in the conduct of experiments. Additionally, it is recommended that any evaluation plan for future cloud seeding experiments on the rim, consider the use of model precipitation estimates as a fully objective covariate. Because the model seems capable of routinely producing useful precipitation estimates for the rim, a future cloud seeding experiment may benefit through a shorter experimental period, as a result of using the model to lessen the precipitation variability and thus the number of cases necessary to detect an anticipated change at a prescribed significance level.

## 4. REFERENCES

Armstrong, R. L., and K. Williams, 1981: Snowfall forecasting in the Colorado mountains. Preprints from Second Conference on Mountain Meteorology, American Meteorological Society, Boston MA, 386-390.

Brown, S. R., 1970: Terminal Velocities of Ice Crystals. Atmos. Sci. Paper 170, Colorado State University, Ft. Collins CO 80523.

Bruintjes, R. T., R. Gall, T. L. Clark, and W. D. Hall, 1991: Comparisons Between Modelling and Observations of Precipitation Over Mountainous Terrain in Arizona. Abstracts, IUGG, General Assembly Symposium Mesoscale Meteorology: Observational Systems, Analysis and Forecasting, Vienna 11-24 August 1991.

Bureau of Reclamation, 1987: Feasibility study on wintertime cloud seeding to augment Arizona water supplies. Final Report to Arizona Department of Water Resources, Intergov. Agr. No. IGA85/86-4500-008, U.S. Bureau of Reclamation, Code D-3720, Denver CO, 133 pp.

Clark, T. L., 1977: A small scale dynamic model using a terrain following coordinate transformation. *J. Comput. Phys.*, 24, 186-215.

Clark, T. L., and R. D. Farley, 1984: Severe downslope windstorm calculations in two and three dimensions using an elastic interactive grid nesting: A possible mechanism for gustiness. *J. Atmos. Sci.*, **41**,329-350.

Clark, T. L., and W. D. Hall, 1990: Multidomain simulations of the time-dependent Navier-Stokes equations: Benchmark error analysis of nesting procedures. *J. Comput. Phys.*, xxx

Cotton, W. R., M. A. Stephens, T. Nehrkorn, and G. J. Tripoli, 1982: The Colorado State University three-dimensional cloud/mesoscale model-1982. Part II: An ice phase parameterization. *J. Rech. Atmos.*, 16, 295-320.

Davis, C. I., 1974: Ice Nucleating Characteristics of Various AgI Aersols. Ph.D. dissertation, University of Wyoming, 259 pp.

DeMott, P. J., W. G. Finnegan, and L. O. Grant, 1983: An application of chemical kinetic theory and methodology to characterize the ice nucleating properties of aerosols used in weather modification. *J. Climate Appl. Meteor.*, 22, 1190-1203.

Dennis, A. S., 1980: *Weather Modification by Cloud Seeding*. Academia Press, Inc. New York, NY. 120-133.

Deshler, T., and D. W. Reynolds, 1987: The evolution of artificially nucleated ice crystals in shallow orographic winter clouds: Two case studies. *11th Conf. on Weather Modification*, Edmonton, Amer. Meteor. Soc., 28-29.

Elliott, R. D., R. W. Shaffer, A. Court, and J. F. Hannaford, 1978: Randomized Cloud Seeding in the San Juan Mountains, Colorado. *J. Appl. Meteor.*, *17*, 1298-1318.

El Majdoub, Ali, 1989: Adaptation of the Rhea winter orographic precipitation model to Morocco. M.S. thesis, South Dakota School of Mines and Technology, PASA IMA-0190-P-IW-4093-00, Rapid City SD, 57pp.

Elliot, Robert. D., 1971: Santa Barbara Pyrotechnic cloud seeding test results 1967-70. *J. Appl. Meteor.*, **10**, 785-795.

_____, D. A. Griffith, J. F. Hannaford, and J. A. Fleuck, 1978: Special Rep. on Background and Supporting Material for the Sierra Cooperative Pilot Project Design, Rep. 78-22, North American Weather Consultants, Goleta CA, 240 pp.

_____, 1981: A seeding effects targeting model. *Preprints of Eighth Conf. on Inadvertent and Planned Weather Modification*, Reno, Amer. Meteor. Soc., 34-39.

Grant, L. O., and R. E. Elliott, 1974: The cloud seeding temperature window. *J. Appl. Meteor.*, **13**, 355-363.

Grant, L. O., and P. W. Mielke, Jr., 1967: A randomized cloud seeding experiment at Climax, Colorado, 1960-65. Proc. Fifth Berkeley Symposium on Mathematical Statistics and Probability, 5, University of California Press, 115-132.

Hall, W. D., D. A. Matthews, and A. B. Super, 1990: Orographic production of supercooled liquid water and precipitation over the Mogollon Rim of Arizona. Conf. on Cloud physics, San Francisco, Amer. Meteor. Soc., **xxx-757**.

Hallett, J., and B. J. Mason, 1958: The influence of temperature and supersaturation on the habit of ice crystals grown from the vapor. *Proc. Roy. Soc. London*, A247, 440-453.

Heymsfield, A., 1982: A comparative study of the rates of development of potential hail embryos in the High Plains storms. *J. Atmos. Sci.*, **39**, 2867-2897.

## Mission

The mission of the Bureau of Reclamation is to manage, develop, and protect water and related resources in an environmentally and economically sound manner in the interest of the American Public.